Fixed Membrane Wings for Micro Air Vehicles: Experimental Characterization, Numerical Modeling, and Tailoring

Bret Stanford, Peter Ifju
Department of Mechanical and Aerospace Engineering, University of Florida, Gainesville, FL, 32611

Roberto Albertani
Research and Education Engineering Facility, University of Florida, Shalimar, FL, 32579

Wei Shyy
Department of Aerospace Engineering, University of Michigan, Ann Arbor, MI, 48109

Abstract

Fixed wing micro air vehicles (wingspan between 10 and 15 cm) are aerodynamically challenging due to the low Reynolds number regime (10^4-10^5) they operate in. The low aspect ratio wings (typically used to maximize area under a size constraint) promote strong tip vortices, and are susceptible to rolling instabilities. Wind gusts can be of the same order of magnitude as the flight speed (10-15 m/s). Standard control surfaces on an empennage must be eliminated for size considerations and drag reduction, and the range of stable center of gravity locations is only a few millimeters long. Membrane aeroelasticity has been identified has a tenable method to alleviate these issues: flexible wing structures with geometric twist (adaptive washout for gust rejection, delayed stall) and aerodynamic twist (adaptive inflation for high lift, larger stability margins) are both considered here. Recent investigations in static aeroelastic characterization, including flight loads, wing deformation, flow structures, aeroelastic tailoring studies through laminate orientation, as well as unconventional techniques based on membrane pre-tension, are reviewed. Multi-objective optimization aimed at improving lift, drag, and pitching moment considerations is also discussed.

Nomenclature

α	angle of attack
A, A_o	deformed and un-deformed areas
$\mathbf{A}_m$	elastic membrane constitutive matrix
β	master/slave stiffness coefficient
$\mathbf{B}$	strain-displacement matrix
c, b	wing root chord, span
C_L, C_D, C_m	lift, drag, and pitching moment coefficients
$C_{L\alpha}$, $C_{m\alpha}$	lift and pitching moment slopes
$\mathbf{D}_p$, $\mathbf{A}_p$	orthotropic laminate bending and stretching stiffness matrices
$\boldsymbol{\varepsilon}_o$, $\boldsymbol{\varepsilon}_L$	linear and nonlinear Green-Lagrange strain pseudo-vectors
ε_{xx}, ε_{yy}, ε_{xy}	chordwise, spanwise, and shear strain
ξ, η, ζ	curvilinear coordinates
E_1, E_2	elastic moduli
f_{ij}	metric terms
$\mathbf{G}$	displacement gradient matrix
G_{12}	shear modulus
h_k, z_k	thickness and position of the k^{th} ply
J	Jacobian
$\mathbf{K}_\sigma$, $\mathbf{K}_c$, $\mathbf{K}_{ext}$, $\mathbf{K}_w$	geometric, constituitive, external, and pre-stress finite element stiffness matrices
$\mathbf{K}_e$, $\mathbf{P}_e$, $\mathbf{F}_e$, $\mathbf{X}_e$	finite element stiffness matrix, and internal force, external force, and solution vector
$\mathbf{K}_p$, $\mathbf{K}_m$	laminate bending and stretching finite element stiffness matrices
L, D	lift and drag forces
$\mathbf{M}$	stress matrix
N_x, N_y, N_{xy}	chordwise, spanwise, and shear stress resultants
ρ	density
p	pressure
q_{ij}	transformation parameters

$\mathbf{Q}_k$	reduced laminate constitutive matrix of the k^{th} ply
Re	Reynolds number
St	Strouhal number
θ	laminate fiber orientation
T	transformation matrix
μ	viscosity
u, v, w	chordwise, spanwise, and vertical displacements
U, V, W	contravariant velocities
U_∞	free-stream velocity
ν_{12}	Poisson's ratio
ω	Gaussian distribution decay function
x, y, z	chordwise, spanwise, and vertical coordinates
x_s, x_m	slave and master node locations

1. Introduction

The rapid convergence of unmanned aerial vehicles to continually smaller sizes and greater agility represents successful efforts along a multidisciplinary front. Technological advances in materials, fabrication, electronics, propulsion, actuators, sensors, modeling, and control have all contributed towards the viable candidacy of micro air vehicles (MAVs) for a plethora of tasks. MAVs are, by definition, a class of unmanned aircraft with a maximum size limited to 15 cm, capable of operating speeds of 15 m/s or less. Examples of successfully designed, built, and flight tested MAV platforms can be seen in the work of Ailinger [1], Torres and Mueller [2], Grasmeyer and Keenon [3], Ifju et al. [4], Shkarayev et al. [5], and Sun et al. [6], among many others.

Ideally, a MAV should be both inexpensive and expendable, used in situations where a larger vehicle would be impractical or impossible, to be flown either autonomously or by a remote pilot. Military and defense opportunities [7] are perhaps easiest to envision (in the form of over-the-hill battlefield surveillance [8], bomb damage assessment [9], chemical weapon detection [10], etc.), though MAVs could also play a significant role in environmental [11], agriculture, wildlife, and traffic monitoring applications. Fixed, flapping, and rotary wing micro air vehicles are all viable candidates for these missions; fixed wings are the focus of this review.

A recent monograph by Shyy et al. [12] provides a review of the aerodynamics of biological flyers, with a chapter devoted to flexible fixed wings. It is the goal of this work to build upon this chapter through a greater amount of detail on recent progress made in the study of low Reynolds number flows about low aspect ratio fixed elastic membrane wings. Particular attention is paid to methods for tailoring the wing structure in order to alleviate the unfavorable aerodynamics found with micro air vehicles: relatively strong wind gusts, flow separation, rolling instabilities, etc. A detailed review of the relevant literature is provided for both experimental and numerical characterization of these wings, followed by development of the specific techniques used in this work. Flow structures, aerodynamic loads/derivatives, and wing deformations are discussed for disparate MAV wing structures, clarifying the relationship between stiffness distribution and flight performance, as well as the potential benefits for aeroelastic optimization via tailoring.

The aeroelastic design of a micro air vehicle differs in many respects from that of conventional, larger aircraft, with less of an emphasis placed on the fundamental trade-off between flexibility and weight. The literature is filled with many successful examples of nominally rigid MAV wings [1], [2], [3], [13], where the larger weight is not seen to be generally prohibitive toward fulfillment of typical mission requirements. Nonetheless, micro air vehicles are notoriously difficult to fly; an expected consequence of a highly maneuverable and agile vehicle that must be flown either remotely or by autopilot [14]. Flexibility is purposefully added to the wing structures with the hope that the pressure load re-distribution can have significant performance benefits. The potentially benevolent aerodynamics provided by aeroelastic structures can help offset the following issues:

1. The operational Reynolds number for MAVs is typically between 10^4 and 10^5. Flow over the upper wing surface can be characterized by massive flow separation, a possible turbulent transition in the free shear layer, and then reattachment to the surface, leaving behind a separation bubble [15]. Such flow structures typically result in a loss of lift, and an increase in drag [16].
2. The low aspect ratio wing (on the order of unity) promotes a large wing tip vortex swirling system [17], which interferes with the longitudinal circulation of the wing [18]. Entrainment of the aforementioned separated flow can lead to tip vortex destabilization [19]; the resulting bilateral asymmetry may be the cause of the rolling instabilities known to plague MAV flight.
3. Sudden wind gusts may be of the same order of magnitude as the vehicle flight speed (10-15 m/s). Maintaining smooth controllable flight can be difficult [13], [20].

4. The range of flyable (statically stable) CG locations is generally only a few millimeters long, which represents a strenuous weight management challenge [21].

Passive shape adaptation can be successfully built into a MAV wing through the use of a flexible membrane skin [4]. The basic structure of these vehicles is built around a composite laminate skeleton. Bi-directional graphite/epoxy plain weave or uni-directional plies are usually the materials of choice, due to durability, low weight, high strength, and ease of fabrication: all qualities well-exploited in the aviation industry [22]. The carbon fiber skeleton is affixed to an extensible membrane skin, of which several choices are available: latex, silicone, plastic sheets, polyester, or cloth [23]. Smart materials for MAV wing skins have attracted interest as well: Pawlowski et al. discuss the use of electrically responsive wing skins [24], and Xu et al. develop flexible shear stress sensing skin to monitor flow separation [25].

The distribution of carbon fiber and membrane skin within the wing determines the aeroelastic response, and two distinct designs are considered in this work. The first can be termed a load-alleviating design, where the wing attempts to streamline itself with the flow. A MAV wing utilizing this concept is given in Figure 1, with thin strips of uni-directional carbon fiber imbedded within the membrane skin, oriented in the chordwise direction. The trailing edge of this batten-reinforced (BR) design is left unconstrained, and the resulting nose-down geometric twist of each flexible wing section should alleviate the flight loads: decrease in C_D, decrease in $C_{L\alpha}$, delayed stall (as compared to a rigid wing) [26]. A certain measure of gust rejection may also be obtained, though this would certainly depend upon the comparison of the relevant time scales between the unsteady flow and the flexible wing. The membrane material in Figure 1 is a latex rubber, which will be the considered for the majority of the results presented in this work.

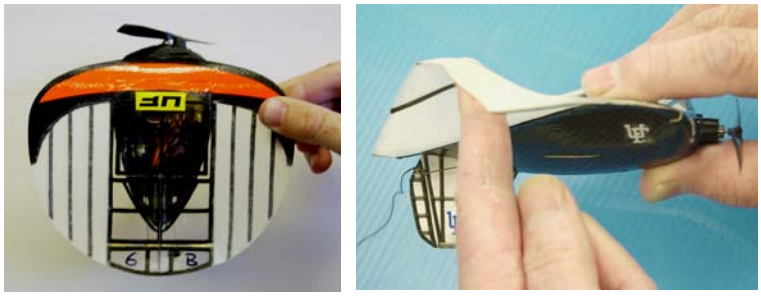

Figure 1. Batten-reinforced membrane wing design.

A second design methodology would seek to further exacerbate the wing's disturbance within the flow: load augmentation. This strategy is demonstrated in Figure 2, where the interior of the MAV wing's membrane skin is unconstrained, while the perimeter of the skin is sealed to a thin curved strip of carbon fiber. The perimeter-reinforced (PR) wing deformation is closer in nature to an aerodynamic twist. Both the leading and the trailing edges of each membrane section are constrained by the relatively-stiff carbon fiber. The positive cambering (inflation) of the wing should lead to an increase in C_L and a decrease (more negative) $C_{m\alpha}$ [27]. It should be noted that these changes in aerodynamic loads and derivatives of both BR and PR wings can only be expected in a time-averaged or steady (if possible) sense. Under strong pressure gradients (typically at larger angles of attack), periodic vortex shedding [28] may lead to membrane vibration [20], with seemingly random variations in time-dependent lift and drag computations in an otherwise steady oncoming flow, as clearly seen in the work of Persson et al. [29] and Lian et al. [30].

A membrane skin lends itself well to micro air vehicle construction [4]. It's typically strong enough to sustain the relatively low flight loads, and presents obvious weight savings (compared to a homogenous carbon fiber wing, for example). Furthermore, its compliant nature is conducive to active wing morphing; substantial shape changes can be inflicted through the use of torque rods or warping cables without an overwhelming amount of required power [14]. Such a design methodology will not be pursued in this work however, which is singularly concerned with passive shape adaptations. As expected, the highly-flexible wing surface may be prone to instabilities, but here again MAV aeroelastic design sees a significant deviation from that of larger vehicles. Classical problems like torsional divergence and panel flutter have little bearing on MAV design, due to the low aspect ratio nature of the wings and the small operating dynamic pressures [31]. Certain instabilities do exist, but can rarely be expected to damage wings constructed from the aforementioned resilient latex and carbon fiber materials. This may not be true for comparatively fragile Mylar skins, which are a popular choice for the construction of flapping wings [32].

Potential problems for fixed membrane wings include the lift slope of a highly flexible wing approaching infinity [33], large-amplitude flapping of a poorly constrained trailing edge [34] (which can provoke excessive drag penalties [35]), or luffing [36]. This latter term describes the large vibration of a membrane stuck within a hysteresis loop: negative camber at a positive angle of attack [37].

Figure 2. Perimeter-reinforced membrane wing design.

In this paper, we review both experimental and numerical analysis of low aspect ratio, low Reynolds number fixed membrane wings. Experimentally, the small dynamic pressures encountered by MAVs will test the force/moment resolution capabilities of most load sensors and sting balances [38]. The lightweight, flexible nature of the membrane skin requires non-contact optical methods for deformation measurements, which can also suffer from resolution and accuracy problems [39]. Though not explicitly discussed here, the highly three-dimensional nature of the flow about a MAV wing [40] makes accurate flow quantification via laser-based flow visualization and PIV [41] difficult, as does the reflective nature of the membrane skin [42].

Computationally, the aeroelastic system is defined by a number of nonlinearities. Multiple levels of fidelity can be reasonably considered for the structural model, the fluids model, and the interfacing technique. Insightful knowledge of the aeroelastic system (perhaps through experimental testing) must guide the numerical model to the correct level of fidelity, but an overarching need for efficient exploration through the design space should also limit this level. Both geometrical and material nonlinearities can be prevalent in membrane skins [43], though a significant pre-tension in the skin is known to provide a linearizing effect [44]; the opposite is true for an initially wrinkled surface [45]. Generally, the flow over a MAV wing will be unsteady and transitional, but various combinations of steady, unsteady, laminar, or turbulent modules can provide satisfactory results [12], depending on Reynolds number, angle of attack, airfoil geometry, freestream turbulence intensity, etc. [15].

The proper correlation between flow structures, wing deformation, and flight loads demonstrated below can uncover the working mechanisms behind various forms of passive shape adaptation, their associated aerodynamic advantages, and the feasibility of exploiting these advantages through tailoring and optimization. These techniques will assist in, and perhaps enable the development of mission-capable fixed wing micro air vehicles, well-suited for the wide-ranging tasks described above.

The remainder of this work is organized as follows. Section 2 outlines the apparatus and procedures used for adequate experimental characterization of the micro air vehicle wings. This includes a low-speed closed loop wind tunnel, a high sensitivity sting balance, and a visual image correlation system. Information is also given detailing wing fabrication and preparation. The computational framework is summarized in Section 3, including nonlinear structural and flow models, aeroelastic coupling, and ad hoc techniques devised to handle the membrane skin pre-tension. Section 4 details the deformation patterns, flow structures, and aerodynamic characterization of a series of baseline flexible and rigid MAV wings, obtained both numerically and experimentally for comparison purposes. Section 5 presents a non-standard aeroelastic tailoring study to identify the optimal wing type and structural composition for a given objective function, as well as various combinations thereof. The work concludes with experimental validation of the performance of selected optimal designs.

2. Experimental Characterization

As will be extensively discussed below, numerical modeling of flexible MAV wings, while conducive to design and optimization studies, is very challenging: at the present time, no practical model exists which can accurately predict all of the unsteady flow phenomenon known to occur over a micro air vehicle. As such, experimental model validation is required to instill confidence in the employed models, highlight numerical shortcomings, and provide additional aeroelastic wing characterization.

All of the aerodynamic characterization experiments discussed in this work are run in a closed-loop wind tunnel, a diagram of which can be seen in Figure 3. Only longitudinal aerodynamics are of interest, and as such only α-sweep capability is built into the test setup. While there exists much successful precedent in such a setup for testing MAV wings [6], [21], [46], whirling arm apparatus have shown some promise for micro air vehicle experiments as well. Advantages to such a system include the possibility of tethered flight without crash risks [47], as well as easier determination of all of the main aerodynamic derivatives and coefficients, along with special maneuver derivatives [48]. The logistics concerning size and weight of such a system limit the maximum testing Reynolds numbers, which is obviously less of a concern for MAVs.

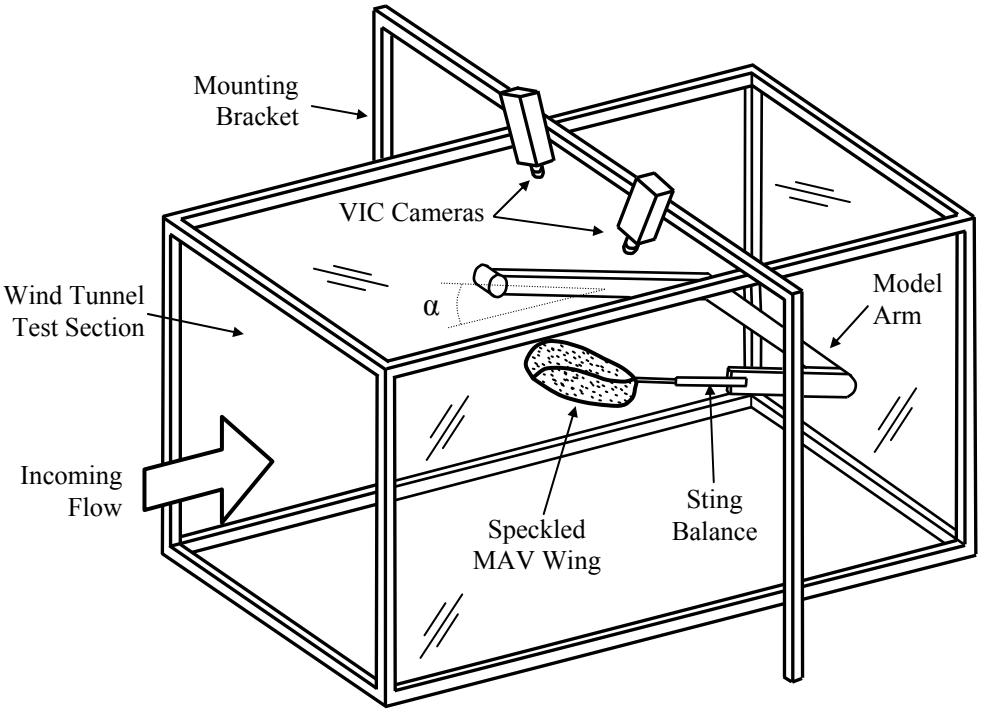

Figure 3. Schematic of the wind tunnel setup.

2.1. Closed Loop Wind Tunnel

General design guidelines for wind tunnel facilities specifically suitable for micro air vehicle aerodynamic characterization are discussed by Babinsky et al. [49] and Mueller [38]. The former emphasizes a series of state-of-the-art requirements for control stratagems, aeroelasticity, thrust integration, and sensor integration of MAV wind tunnel testing. The test facility used for this work is an Engineering Laboratory Design, Inc. (ELD) 407B closed-loop wind tunnel, with the flow loop arranged in a horizontal configuration. The test section has an inner dimension of 0.84 m on each side and is 2.44 m deep. The velocity range is between 2 and 45 m/s, and the maximum Reynolds number is 2.7 million.

Suitable flow conditions are achieved through hexagonal aluminum honeycomb cell, high-porosity stainless steel screens, and turning vane cascades within the elbows of the closed loop. Centerline turbulence levels are measured on the order of 0.2%. Optical glass window access is available on the sidewalls and the ceiling. A Heise model PM differential pressure transducer is used to measure the pressure difference from a pitot-static tube mounted within the test section. A four-wire resistance temperature detector is mounted to the wall of the test section for airflow temperature measurements. Further details of the operational specifications of this particular system are given by Sytsma [42].

2.2. Strain Gage Sting Balance

Several outstanding issues exist with measuring the aerodynamic loads from low Reynolds number flyers. Several such airfoils are known to exhibit hysteresis loops at high angles of attack. If the flow does not reattach to the wing surface (typically for lower Reynolds numbers below $5 \cdot 10^4$ [50]) counterclockwise hysteresis loops in the lift data may be evident; the opposite is true if a separation bubble exists via reattachment [51]. Adequate

knowledge of such a loop is obviously important as it effects vehicle control problems via stall and spin recovery. As described by Marchman [52], the size of the hysteresis loop measured in a wind tunnel can be incorrectly decreased by poor flow quality: large freestream turbulence intensity levels or acoustic disturbances (noise emitted from the turbulent boundary layer along the tunnel walls, the wind tunnel fan, etc. [51]). Mounting techniques are also presumed to cause an incorrect relationship between Reynolds number and the zero-lift angle of attack among several sets of published data [52].

Sensitivity is another concern, particularly in drag force measurements which may be as low as 0.025 N (computed for a wing with a chord of 100 mm and a Reynolds number of $5 \cdot 10^4$). An electrical resistance strain gage sting balance is typically used for force and moment measurements, though many other methods are reported in the literature for MAV testing. While strain gages typically provide the greatest sensitivity and simplicity, they are also prone to temperature drift, electromagnetic interference, creep, and hysteresis. Pressure measurements over the airfoil and wake surveys can be used (Kaplan [40], for example, uses particle image velocimetry data to calculate lift via circulation and effective span at low Reynolds numbers), but may not always have the required sensitivity [51]. Successful attempts to avoid strain gages for MAV load measurements are also given by Kochersberger and Abe, who describe an external mechanism to measure force by achieving zero net moment amount the pivot axis of a beam balance [53].

Design and implementation of strain gage based-sensors for MAV applications can be found in the work of Mueller [38] (external platform sting balance) and Suhariyono et al. [54] (finite element-based design and analysis of an internal balance). Typical setups involve the use of six channels in a full Wheatstone-bridge configuration, whose signals can be converted into three forces and three moments depending upon the rotational orientation of the MAV. An internal Aerolab 01-15 6-component strain gage sting balance is used for force/moment measurements in the current work. Wind tunnel models are mounted to the sting balance by a simple jaw mechanism. Details concerning data acquisition and signal processing for this particular system are given by Ifju et al. [55].

Standard procedures [56] are used to calibrate the sting balance down to an adequate sensitivity: 0.01 N in drag (though still just 40% of the minimum given above). Such a resolution is comparable to that found in the work of Pelletier and Mueller [46], but superior precision is used by Kochersberger and Abe [53] and Moschetta and Thipyopas [57]. The calibration matrix is determined through the use of known weights applied at control points in specified directions. This calibration is able to predict the relationship between load and signal for a given channel, as well as potential interactions (second-order interactions are not included) in both single and multiple load configurations. Further information on the calibration of strain gage sting balances for micro air vehicle measurements is given by Mueller [38] and Albertani [58].

Numerous examples of experimentally measured loads (lift and drag, typically) from membrane wings can be found in the literature. Early work by Newman and Low [59] and Greenhalgh et al. [37] consider the two-dimensional sail: a large aspect ratio elastic sheet stretched (or possibly slack) between a rigid leading and trailing edge supports. More recently, Galvao et al. [60] conduct similar tests, but with smaller aspect ratios and Reynolds numbers (between $3 \cdot 10^4$ and 10^5), in order to emulate MAV flight. The results show a consistent pre-stall increase in lift, lift slope, drag, and power efficiency of the membrane wing over its rigid counterpart, though not efficiency. De-cambering of the wing as the pressure on the upper surface increases due to imminent flow separation is seen to ameliorate the stall behavior, as compared to a rigid plate.

Waszak et al. [26] report load measurements from batten-reinforced membrane MAV wings (Figure 1). Proper tailoring of the number of battens, as well as the membrane material (latex or monofilm) leads to a measured stalling angle delayed 10° past that for the rigid wing. Similar balance data is given by Tamai et al. [41] for two-dimensional generalizations of BR wings. Albertani et al. [21] detail loads measurements of both BR and PR wings, with dramatic improvements in longitudinal static stability of both membrane wings over their rigid counterpart. The BR wing has a noticeably smoother lift behavior in the stalled region, though neither deforms into a particularly optimal aerodynamic shape: both incur a drag penalty. A comparison of aerodynamic measurements between MAV wings and vehicles finds a decrease in lift of the entire vehicle, but less of a penalty when load-alleviation is built into the membrane wing [58].

All of the work cited in this section provides time averaged aerodynamic loads; experimental unsteady force/moment data of fixed membrane wings is very rare. Shyy et al. [61] are able to study the effects of oscillatory low Reynolds number flow with a flow-restricting device in the exhaust of an open-loop wind tunnel. Data is recorded at 2 kHz. A two-dimensional membrane sailwing is measured with larger lift-to-drag ratios (compared to a rigid model) for the high-velocity portion of the flow cycle, but substantially lower during the low-velocity: membrane collapse leads to massive flow separation. This problem is remedied with the use of a hybrid airfoil, where a wire mesh prevents negative-cambering of the wing.

2.2.1. Uncertainty Quantification

Two types of uncertainty are thought to contribute to the eventual error bounds of sting balance data. The resolution error is indicative of a measurement device's resolution limit: for example, the inclinometer used to measure the pitch of a model can measure angles no finer than 0.1°, an uncertainty that can be propagated through the equations to find its theoretical effect on the aerodynamic coefficients using the Kline-McClintock technique [62]. Typical resolution errors are: 3 Pa of dynamic pressure from the Heise, $1.2 \cdot 10^{-7}$ V from the output voltage of the strain gages (estimated from the quantization error of the 16-bit DAQ cards), 0.001 m^2 from wing area measurements, and 0.002 m from chord length measurements.

The second source is the precision error, a measure of the repeatability of a measurement. This is well quantified by the standard deviation of the voltage signals. Uncertainty bounds can be computed with a squared sum of the resolution and precision errors (where the latter is magnified by Student's t at 95% confidence and infinite degrees of freedom). The precision of the strain gage signals is found to contribute the most error to the aerodynamic coefficients, particularly in the stalled regions. Typical uncertainty percentages are 5% for C_L, 7% for C_D, 9% for L/D, and 20% for C_m. Theses values can be expected to double during stall. Error bars measured for MAV wings through an α-sweep can be seen in the work of Waszak et al. [26] and Stanford et al. [63].

2.2.2. Wind Tunnel Corrections

Corrections can be applied to the coefficients of lift, drag, and pitching moment based upon wind tunnel blockage, and model flexibility effects. The solid blockage effect is due to the presence of the model within the wind tunnel, thus decreasing the effective area of the test section and increasing the flow velocity (and the coefficients) in the vicinity of the model [64]. Wake blockage occurs when the flow outside of the model's wake must increase, in order to satisfy the flow continuity in a closed tunnel. In an open freestream, the velocity outside of the wake would be equal to the freestream velocity. The effect of wake blockage is proportional to the wake size, and therefore proportional to drag [16]. Streamline curvature blockages are the effect of the tunnel walls on the streamlines around the model. The streamlines are compressed, increasing the effective camber and lift [65]. Such corrections generally decrease both lift and drag, while the pitching moment is made less negative, with percentage changes on the order of 2-3%.

Finally, flexibility effects within the wind tunnel setup must be accounted for. These effects are primarily caused by the elasticity of the internal strain gage sting balance; under load the wind tunnel model will pitch up via a rigid body rotation. Visual image correlation (described below) is used to measure the displacement at points along the wing known to be nominally rigid (specifically, the sting balance attachment points along the wing root). This data then facilitates the necessary transformations and translations of the wing surface, and is used to correct for the angle of attack. $\Delta\alpha$ is a positive monotonically increasing function of both lift and dynamic pressure, and can be as large as 0.7º at high angles of attack [58].

2.3. Visual Image Correlation

Wind tunnel model deformation measurements are a crucial experimental tool towards understanding the role of structural composition upon aerodynamic performance of a MAV wing. The flexible membrane skin generally limits applications to non-contacting optical methods, several of which have been reported in the literature. Galvao et al. [60] use stereo photogrammetry for displacement measurements of a membrane wing, with a reported resolution between 35 and 40 μm. Data is available at discrete markers placed along the wing. Projection moiré interferometry requires no such marker placement (a fringe pattern is projected onto the wing surface), and the resulting data set is full-field. However, displacement resolutions reported by Fleming et al. [66] are relatively poor (250 μm), the dual-camera system must be rotated during the α-sweep, and only out-of-plane data is available, making strain calculations (if needed) impossible. Burner et al. [39] discuss the use of photogrammetry, projection moiré interferometry, and the commercially available Optotrak™ system. The authors find no single technique suitable for all situations, and that a cost-benefit tradeoff study may be required. Furthermore, the methods need not be mutually exclusive, as situations may arise wherein they can be used in combination. For the current work, a visual image correlation system (VIC), originally developed by researchers at the University of South Carolina [67], is used to measure wing geometry, displacements, and plane strains. This technique is widely-regarded as state-of-the-art in terms of experimental mechanics in general [68], and for wind tunnel model deformation in particular [21].

The underlying principle of VIC is to calculate the displacement field by tracking the deformation of a subset of a random speckle pattern applied to the specimen surface. The random pattern is digitally acquired by two cameras before and after loading. The acquisition of images is based on a stereo-triangulation technique, as well as the computing of the intersection of two optical rays: the stereo-correlation matches the two 2-D frames taken simultaneously by the two cameras to reconstruct the 3-D geometry. The calibration of the two cameras (to account

for lenses distortion and determine pixel spacing in the model coordinates) is the initial fundamental step, which permits the determination of the corresponding image locations from views in the different cameras. Calibration is done by taking images (with both cameras) of a known fixed grid of black and white dots.

Temporal matching is then used: the VIC system tries to find the region (in the image of the deformed specimen) that maximizes a normalized cross-correlation function corresponding to a small subset of the reference image (taken when no load is applied to the structure) [67]. The image space is iteratively swept by the parameters of the cross-correlation function, to transform the coordinates from the original reference frame to coordinates within the deformed image. An originally square subset in the un-deformed image can then be mapped to a subset in the deformed image. As it is unlikely that the deformed coordinates will directly fall onto the sampling grid of the image, accurate grey-value interpolation schemes [69] are implemented to achieve optimal sub-pixel accuracy without bias. This procedure is repeated for a large number of subsets to obtain full-field data.

In order to capture the three-dimensional features and deformation of a wind tunnel model, twin synchronized cameras, each looking from a different viewing angle, are installed above the wind tunnel ceiling, as can be seen in Figure 3. As the cameras must remain stationary through the experiment (to preserve the information garnered from the calibration procedure), a mounting bracket is constructed to straddle the tunnel, and prevent the transmission of vibration. Optical access into the test section is through an optical glass ceiling. The results of conducting visual image correlation tests with a glass interface between the cameras and the specimen have been studied, with little benign effects reported [70]. Further details of the VIC process in terms of calibration, illumination, and image synchronization/acquisition is given by Albertani [58].

Typical data results that can be obtained from the VIC system consist of the geometry of the surface in discrete x, y, and z coordinates, and the corresponding displacements along the wing (u, v, and w). The VIC system places a grid point every N pixels, where N is user defined. A final post-processing option involves calculating the in-plane strains (ε_{xx}, ε_{yy}, and ε_{xy}). This is done my mapping the displacement field onto an unstructured triangular mesh, and conducting the appropriate numerical differentiation (the complete definition of finite strains is used). Aeroelastic deformation measurements of membrane MAV wings are given by Albertani et al. [21], Ifju et al. [55], and Stanford et al. [63] for static measurements, and by Albertani et al. [71] for high speed measurements of unsteady wing vibration.

2.3.1. Data Processing

The objective of most of the wind tunnel tests given in the remainder of this work is to determine the deformation of the wings under steady aerodynamic loads, at different angles of attack and free stream velocities, while simultaneously acquiring aerodynamic force data. Each angle of attack requires a separate wind-off reference image: failure to do so will inject rigid body motions (as the body moves sequentially from one angle of attack to the next) into the displacement fields. If each reference image taken for VIC is of the fully assembled wing, the amount of pre-strain in the wing is not included in the measured strain field, but only those caused by the aerodynamic loads. This condition needs to be carefully considered in the evaluation of the results, since the areas of relaxation of the pre-existing tension will generate areas of "virtual" compression within the skin. The thin membrane cannot support a genuine compressive stress (it will wrinkle), but negative Poisson strains are possible.

An alternative procedure uses the un-stretched sheet of latex rubber (prior to adhesion on the wing) as a reference image. This provides the state of pre-strain in the membrane, as well as the absolute strain field during wind tunnel testing, but makes the displacement fields very difficult to interpret and is not used here. The pre-strain data is merely recorded (with a separate set of reference and deformed images), but not used as a reference for further aerodynamic testing. As mentioned above, the acquired displacement field will be composed of both elastic wing deformation and rigid body motion/translations originating from the sting balance, the latter of which must be filtered out. The computed strains are, theoretically, unaffected by these motions.

2.3.2. Uncertainty Quantification

In order to estimate the resolution error of the VIC system, a simple ad hoc experiment is conducted. A known displacement field is applied to a structure, and then compared with the field experimentally determined by way of image correlation. A thin latex membrane is stretched and fixed to a rigid aluminum ring with a diameter of 100 mm. The center of the membrane circle is then indented with a rigid steel bar with a spherical head of 8 mm diameter. The bar is moved against the membrane by a micrometer with minimum increments of 0.25 mm.

Results, in terms of the error between commanded displacement (via the micrometer) and the measured displacement at the apex of the membrane profile, directly beneath the axis of the indentation bar, are given in Figure 4. Three different VIC setups are shown: 0.5, 3, and 10 speckles per millimeter of membrane, the latter of which corresponds to 2 pixels per speckle (with half the membrane in view). As expected, the error is smallest for

the finest speckle pattern, whose readings randomly oscillate about zero, with a peak error of 0.018 mm (0.6%). The coarser speckling patterns randomly oscillate at an offset error of 0.04 mm, with a peak error of 0.077 mm (2.2%). This places the resolution error for the VIC system between 10 and 20 μm, about twice the resolution reported for the photogrammetry system [60]. Though not explicitly discussed here, the strain resolution is estimated to be between 500 and 1000 με (a non-dimensional parameter independent of speckle size), a high value (compared to strain gages, for example) owing to the differentiation methods used.

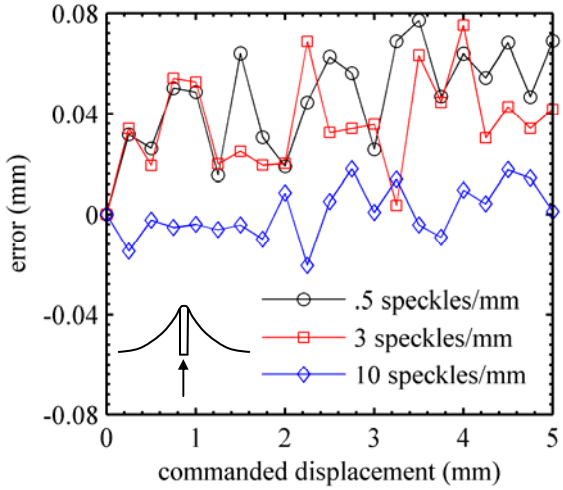

Figure 4. Quantification of the resolution error in the VIC system.

2.4. Flow Visualization

Though specific results are not explicitly discussed in this work, much progress has been made in both qualitative flow visualization and quantitative particle image velocimetry for membrane wings. Very recent PIV work has detailed the flow over two-dimensional generalizations of the membrane wings in Figure 1 and Figure 2: Tamai et al. [41] study batten-reinforced airfoils, while Rojratsirikul et al. [72] study perimeter-reinforced airfoils. The former is able to show that trailing edge washout can keep the flow attached to the flexible surface up to 14º angle of attack, while a rigid wing under similar conditions shows a very large separation bubble [41]. The latter use similar techniques for a membrane fixed at the trailing and leading edges: mean membrane shape is insensitive to angle of attack, though time-averaged flow is not, through the development of flow separation and vortex shedding. The authors are also able to show a strong time-dependent correlation between membrane vibration and the height of the shear layer [72]. Streamline data from a similar sailwing study is given by Lorillu et al. [73].

Results from more operational vehicles are given by Parks [74], who measures the vortex core of a 6.0 aspect ratio BR membrane wing to be 5% to 15% higher above the wing than for the rigid case, though the flexible wing is seen to have a denser core-distribution of velocity for moderate angles of attack. Gamble and Reeder [75] measure the flow structures resulting from interactions between propeller slipstream and the same BR wing. The rigid wing spreads the axial component of the propwash further along the wing (resulting in a higher measured drag), whereas the membrane wing can absorb the downwash and upwash. A region of flow separation is measured at the root of the rigid wing, significantly larger and stronger than that measured from the membrane wing; the superiority decreases with larger Reynolds numbers. Flow visualization of low aspect ratio membrane MAV wings can be found in the work of Waszak et al. [26] and Sytsma [42].

2.5. Model Fabrication and Preparation

Only the wing (152 mm wingspan, 124 mm root chord, 1.25 aspect ratio) of the MAVs seen in Figure 1 and Figure 2 is considered in this work. The maximum camber at the root is 6.8% (at x/c = 0.22), the maximum reflex at the root is -1.4% (at x/c = 0.86), and 7º of positive geometric twist (nose up) is built into the wingtip. The MAV wing has 7º of dihedral between 2y/b = 0.4 and the wingtip. The fuselage, stabilizers, and propeller are omitted from both computations and experiments. The leading edge, inboard portion of the wing, and perimeter (of the PR wings) are constructed from a bi-directional plain weave carbon fiber laminate with 3000 fibers/tow, pre-impregnated with thermoset epoxy. The battens (for the BR wings) are built from uni-directional strips of carbon

fiber. These materials are placed upon a tooling board (appropriately milled via CNC) and cured in a convection oven at 260º F for four hours. A wind tunnel attachment (to be fastened to the aforementioned jaw mechanism) is bonded along the root of the wing between x/c = 0.25 and 0.8.

The latex rubber skin adhered to this wing surface is 0.12 mm thick, and approximately isotropic. A random speckle pattern is applied to the latex sheet with flat black spray paint, and then coated with a layer of dulling spray. Each paint speckle, while relatively brittle, has a small average diameter (less than 0.5 mm) and is generally not connected to another speckle pattern; the pattern should not provide significant reinforcement to the latex. If information concerning the state of pre-strain in the skin is desired, a picture of the un-stretched latex sheet is taken for future use as a reference in the VIC system. The latex is then appropriately stretched about a frame (or not at all if a slack membrane is desired), and adhered to the upper carbon fiber wing surface (which must be painted white) with spray glue. After the glue has dried, the excess latex is trimmed away. A picture of the resultant wind tunnel model is given in Figure 5.

Figure 5. Speckled batten-reinforced membrane wing with wind tunnel attachment.

3. Computational Framework

Several difficulties are associated with modeling the passive shape adaptation of a flexible micro air vehicle wing. From a fluid dynamics standpoint, the low aspect ratio wing (1.25) forces a highly three-dimensional flow field, and the low Reynolds number (10^5) implies strong viscous effects such as flow separation, transition, and potential reattachment. Structurally, the mechanics of the rubber membrane inflation are inherently nonlinear, and the orthotropy of the thin laminated shells used for the wing skeleton is dependent on the plain weave fiber orientation. Further difficulties arise with the inclusion of a state of pre-tension within the membrane. This section, as above, will detail recent progress made in the computational modeling of membrane MAV wings, as well as provide a review or relevant literature.

The aeroelastic membrane structure is dominated by three-dimensional structural and aerodynamic effects, but much useful insight can be gained from two-dimensional simulations and experiments. Such endeavors are obviously easier to undertake for PR-type membrane wings, but three-dimensional reinforcement must be taken into account for a pure membrane (or string in two dimensions) with geometric twist, as the structure alone cannot sustain a flight load in a stable manner [35]. A second option involves considering an elastic sheet with some bending/flexural stiffness, which is essentially the design approach taken for the batten-reinforced wing, with the addition of carbon fiber battens.

A large variety of work can be found in the literature concerning two-dimensional flexible beams in flow. For problems on a MAV scale, work tends to focus on flags and organic structures such as leaves, seaweed, etc. Fitt and Pope [34] derive an integro-differential flag equation for the shape of a thin membrane with bending stiffness in unsteady inviscid flow, considering both a hinged and a clamped leading edge boundary condition. Argentina and Mahadevan [77] solve a similar problem, and are able to predict a critical speed that marks the onset of an unstable flapping vibration, noting that the complex instability is similar to the resonance between a pivoting airfoil in flow and a hinged-free beam vibration. Over-prediction of the unstable flapping speed (when compared to experimental data) leads to the possibility of a stability mechanism wherein skin friction induces tension in the membrane. Alben et al. [101] discuss the streamlining of a two-dimensional flexible filament for drag reduction. In particular, they are able to show that the drag on a filament at high angles of attack decreases from the rigid U_∞^2 scaling to $U_\infty^{4/3}$.

The list of publications pertaining to aeroelastic simulations of membrane wings (with no bending stiffness) is very large, as summarized in Table 1. The literature is sorted by the level of fidelity utilized for the structural and aerodynamics models, whether the test subject is load-alleviating (BR) or load-augmenting (PR) design, and

whether the simulation is in two or three dimensions. Entries that indicate a treatment of both BR and PR type designs utilize a hybrid wing: a membrane surface with a flexible trailing edge, for example.

Table 1. Literature review of aeroelastic membrane simulations, divided by structural model (columns) and aerodynamics model (rows).

	Inextensible/Slack	Linear Stress Stiffening	Geometrically Nonlinear	Hyperelastic
Linear/Analytical	[78][79][80] (○) [81] (○/Δ)		[82] (○) [33][83] (□/◊)	
Inviscid Panel Method	[84] (○)	[44][85][86] (□)	[87] (○) [88][89] (□/◊)	[90] (□)
Steady Laminar	[91][92][73] (○)	[27] (□)	[91] (○) [63] (□)	
Unsteady Laminar			[93][94][95] (○)	[29] (○) [30][96] (◊)
Steady Turbulent	[97] (○)		[97][61] (○)	
Unsteady Turbulent	[98] (○)		[99] (○)	[100] (◊)
Transitional				[20] (○)

○ - load augmenting airfoil, □ - load augmenting wing, Δ - load alleviating airfoil, ◊ - load alleviating wing

Early work in the study of membrane wings without bending stiffness is given by Voelz [78], who describes the classical two-dimensional sail equation (upper left of Table 1): a slack inextensible membrane, fixed at the leading and trailing edges, immersed in incompressible, irrotational, inviscid steady flow. Using thin airfoil theory, along with a small angle of attack assumption, Voelz is able to derive a linear integro-differential equation for the shape of the sail as a function of incidence, freestream velocity, and slack ratio. Various numerical solution methods are available, including those by Thwaites [79] (eigenfunction methods) and Nielsen [80] (Fourier series methods), to solve for lift, pitching moments, and membrane tension. Multiple solutions are found to exist at small angles of attack with a finite slack ratio: approaching 0° from negative angles provides a negatively-cambered sail, though the opposite is true if this mark is approached from a positive value. The sail is uncertain as to which side of the chord-line it should lie [79], a phenomenon which ultimately manifests itself in the form of a hysteresis loop [33]. Variations on this problem are considered by Haselgrove and Tuck [81], where the trailing edge of the membrane is attached to an inextensible rope, thereby introducing a combination of adaptive aerodynamic and geometric twist. Increasing the length of the rope is seen to improve static stability, but decrease lift.

Geometrically nonlinear membrane elasticity (third column of Table 1) is included in the work of Murai and Maruyama [87] and Jackson [82], indicating a nonlinear C_L-α relationship as strains develop within the membrane at high incidence. Viscous flow models are employed in the work of Cyr and Newman [92] and Smith and Shyy [91]. The latter cites viscous effects as having much more influence on the aerodynamics of a sail wing than the effects of the assumptions made with linear thin airfoil theory. Specifically, inviscid solutions tend to over-predict lift at higher angles of attack (or large slack ratios), due to a loss of circulation caused by viscous effects about the trailing edge. A comparison of lift and tension versus angle of attack with experimental data yields mixed results; surprisingly, the lift is over-predicted by the viscous flow model, yet the tension is under-predicted. Smith and Shyy also note a substantial discrepancy in the available experimental data in reported values of slack ratios, sail material properties, and Reynolds numbers, which may play a role in the mixed comparisons [97].

Unsteady flow simulations over a load-augmenting membrane airfoil are given in the recent work of Lian and Shyy [20], Persson et al. [29], and Gordnier [95]. Gordnier's technique couples a sixth-order Navier-Stokes solver to a geometrically nonlinear membrane model to study the vortex shedding and subsequent airfoil vibration in a two-dimensional configuration. For low angles of attack, the airfoil is largely steady, as the vortex rollup occurs predominately in the wake. At moderate incidence the membrane sees a third mode standing wave, while at high angles the second mode dominates, though the response is less regular. Membrane vibration is seen to excite the separated shear layer, prompting earlier roll up and a series of secondary vortices, as compared to a rigid wing of the same mean deflected membrane shape [95].

Three complicating factors can arise with the simulation of a three-dimensional membrane wing, rather than the planar airfoil case [88]. First, the tension is not constant (in space or direction), but is in a state of plane-stress. Secondly, the wing geometry can vary in the spanwise direction, and must be specified. Finally, the membrane may possess a certain degree of orthotropy [36]. Most importantly, analytical solutions cannot generally be found.

Simplifying assumptions to this problem are given by Sneyd et al. [83] (triangular planform) and Ormiston [33] (rectangular sailwing). Sneyd et al. reduce both the aerodynamics and the membrane deformation to two-dimensional phenomena, where the third dimension is felt through the presence of a trailing-edge cable. Ormiston assumes both spanwise and chordwise deformation (but not aerodynamics), and is able to effectively decouple the two modules by using only the first term of a Fourier series to describe the inflated wing shape. Boudreault uses a higher-fidelity vortex lattice solver, but also prescribes the wing shape, here using cubic polynomials [85]. Holla et al. [86] use an iterative procedure to couple a double lattice method to a structural model, but assume admissible mode shapes to describe the deformation of a rectangular membrane clamped along the perimeter. The stress in the membrane is assumed to be equal at all times to the applied pre-stress (initial tension overwhelms the nonlinearities in the membrane mechanics: second column of Table 1). A similar framework is used by Sugimoto in the study of circular membrane wings, where the wing shape is completely determined by a linear finite element solver [44].

Jackson and Christie couple a vortex lattice method to a nonlinear structural model for the simulation of a triangular membrane wing. Comparisons between a rigid wing, a membrane wing fixed at the trailing edge, and one with a free trailing edge elucidate the tradeoffs in lift between adaptive camber and adaptive washout [88]. Aeroelastic models directly pertaining to MAV wings are given by Lian et al. [30] (BR wings) and Stanford et al. [63] (PR wings). Lian et al. couple a hyperelastic solver (fourth column of Table 1) and an unsteady viscous flow solver. Battens are simulated with a dense membrane. The results indicate self-exciting membrane vibration on the order of 100 Hz, with a maximum wing speed about 2% of the freestream, though overall aerodynamics are similar to that of a rigid wing prior to stall [30]. Stanford and Ifju discuss the steady laminar aeroelasticity of a PR wing, and are able to show the expected increase in lift and stability. Significant drag penalties are seen to arise with increasing Reynolds numbers, though the opposite is true for the rigid wing [63].

For the results explicitly discussed in this work, only static aeroelasticity is considered. Past wind tunnel work has indicated that MAV membrane inflation may be modeled as qausi-static for a large range of angles of attack up to stall. For a slack membrane PR wing, experimental data of Albertani et al. [71] show dynamic deformations ~10% of the time-averaged value and a dominant St of 4.29 at 0º angle of attack. At 15º however, these numbers have reduced to ~1% dynamic deformations and a St of 0.98. Certainly, unsteady effects are present for all flight ranges, but may be ignored for a relevant portion without significant errors and at a reduced cost (an important consideration for thorough exploration of the design space). Stanford et al. indicate that the membrane MAV wing is nearly-stationary between 6º and 21º angles of attack, and that adequate predictive capability of a static aeroelastic model still exists for those flight conditions with obvious unsteady features [63]. Unsteady phenomena may be even less important for BR-type wings, as the amount of unconstrained membrane skin is less.

3.1. Structural Solver

The unstructured mesh used for finite element analysis can be seen in Figure 6. 2146 nodes are used to describe the surface of the semi-wing, connected by 4158 three-node triangle elements. The same mesh is used for both batten and perimeter-reinforced computations, by using different element-identification techniques, as seen in the figure. Greater local effects are expected in the membrane areas of the wing, and the mesh density is altered accordingly. Nodes that lie along the wing root between x/c = 0.25 and 0.8 are given zero displacement/rotation boundary conditions, to emulate the restrictive effect of the wind tunnel attachment (Figure 5). All nodes that lie on the wing root are constrained appropriately as necessitated by wing symmetry. Complexities involving membrane wing models with both membranes and elastic shells (such as batten reinforcement) can be found in the work of Stanford et al. [102] (linear mechanics) and Ferguson et al. [103] (nonlinear).

3.1.1. Composite Laminated Shells

Discrete Kirchhoff triangle plate elements [104] are use to model the bending/twisting behavior of the carbon fiber areas of the wings: leading edge, root, perimeter, and battens. Due to the comparative stiffness of these materials, linear behavior is assumed. The orthotropy of the plates is introduced by the flexural stiffness matrix of the laminates, $\mathbf{D}_p$, relating three moments (two bending, one twisting) to three curvatures:

$$\mathbf{D}_p = \sum_{k=1}^{NL} \mathbf{Q}_k \cdot \left(h_k^3 / 12 + h_k \cdot z_k^2 \right) \tag{1}$$

where NL is the number of layers in the laminate, h_k is the thickness of the k^{th} ply, z_k is the normal distance from the mid-surface of the laminate to the mid-surface of the k^{th} ply, and $\mathbf{Q}_k$ is the reduced constituitive matrix of each ply, expressed in global coordinates. $\mathbf{Q}_k$ depends upon the elastic moduli in the 1 and 2 directions (equal for the bi-

directional laminate, but not so for the uni-directional) E_1 and E_2, the Poisson's ratio ν_{12}, and the shear modulus G_{12}. The finite element stiffness matrix pertaining to bending/twisting is then found to be:

$$\mathbf{K}_p = \mathbf{T} \cdot \int_{A_o} \mathbf{B}_p^T \cdot \mathbf{D}_p \cdot \mathbf{B}_p \cdot dA \cdot \mathbf{T}^T \tag{2}$$

where **T** is a matrix which transforms each element from a local coordinate system to a global system, $\mathbf{B}_p$ is the appropriate strain-displacement matrix [105], and A_o is the un-deformed area of the triangular element. $\mathbf{K}_p$ is a 9x9 matrix whose components reflect the out-of-plane displacement w and two in-plane rotations at the three nodes.

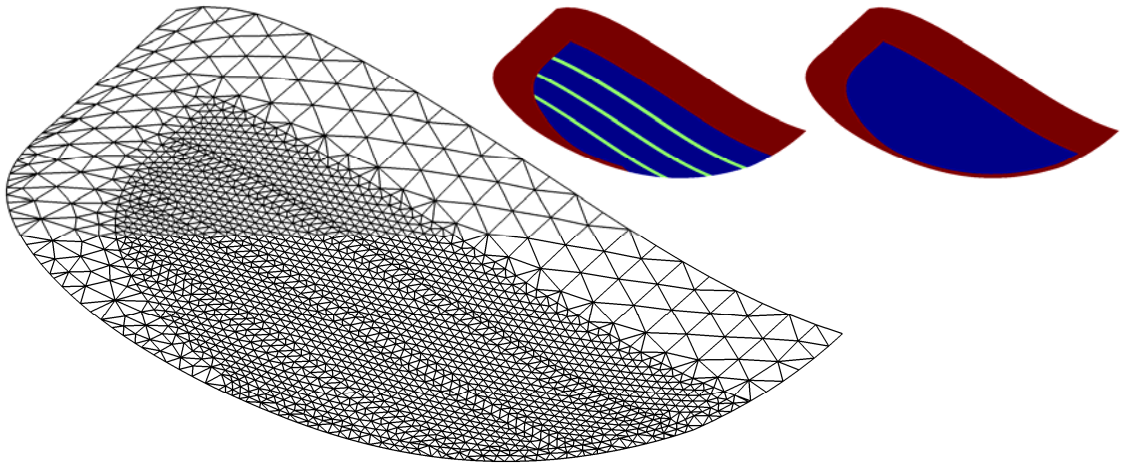

Figure 6. Unstructured triangular mesh used for finite element analysis, with different element types used for PR and BR wings.

Similarly, in-plane stretching of the laminates (a secondary concern, but necessarily included), is given by:

$$\mathbf{A}_p = \sum_{k=1}^{NL} \mathbf{Q}_k \cdot h_k \tag{3}$$

where $\mathbf{A}_p$ is a laminate matrix relating three in-plane stress resultants to three strains. Expressions similar to Eq. (2) are then formulated to compute $\mathbf{K}_m$, the 6x6 finite element stiffness matrix governing in-plane displacements u and v at the three nodes. $\mathbf{K}_m$ and $\mathbf{K}_p$ are then combined to form the complete 15x15 shell stiffness matrix of each element, $\mathbf{K}_e$. Drilling degrees of freedom are not included. Though some wing designs may use un-symmetric laminates, coupling between in-plane and out-of-plane motions is not included.

3.1.1.1. Loads Model Validation/Estimation

The following method is used to both validate the model presented above, and identify the relevant material properties of the laminates. A series of weights are hung from a batten-reinforced wing (with 2 layers of bi-directional carbon fiber oriented 45º to the chord line and 1 layer uni-directional battens, but no membrane skin) at nine locations: the two wing tips, the trailing edges of the six battens, and the leading edge, as shown in Figure 7. VIC is used to measure the resulting wing displacements. A linear curve is fit through the load-displacement data of all nine points due to all nine loadings. The slopes of these curves are used to populate the influence matrix in Table 2: the diagonal gives the motion of a wing location due to a force at that location; the off-diagonals represent indirect relationships.

A genetic algorithm is then used for system identification. The six variables are the material parameters: E_1, ν_{12}, and G_{12} of both the plain weave and the battens. E_2 is assumed to be equal to E_1 for the plain weave, and equal to 10 MPa for the uni-directional battens. This latter value has little bearing on the results, as the 1 direction corresponds with the axis of the batten. The objective function is the sum of the squared error between the diagonals of the computed and the measured influence matrix. The error terms are appropriately normalized before summation and off-diagonal components are not considered in the optimization. For the genetic algorithm, the population size is 20,

the elitism count is 2, reproduction is via a two-point crossover function with a 0.8 crossover fraction, and a uniform mutation function is used with a 0.01 mutation rate. Convergence is adequately achieved after 30 iterations, with each function evaluation call requiring a single finite element analysis.

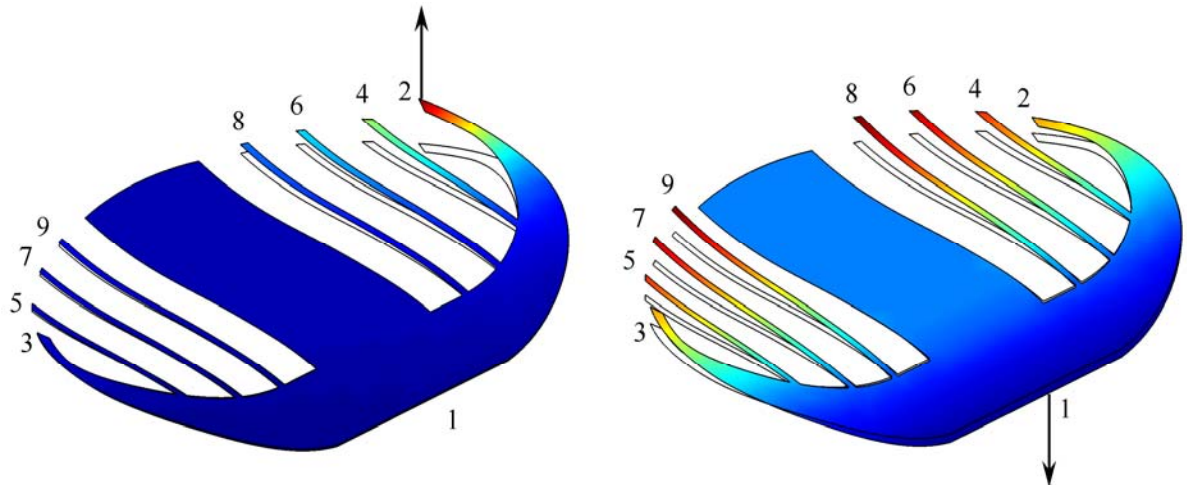

Figure 7. Computed deformations of a BR wing skeleton due to a point load at the wing tip (left) and the leading edge (right).

Table 2. Experimental influence matrix (mm/N) at points labeled in Figure 7.

	1	2	3	4	5	6	7	8	9
1	1.58	-2.90	-2.97	-3.00	-3.07	-3.47	-3.54	-3.05	-3.03
2	-2.93	104.65	3.94	50.85	5.88	36.47	7.65	26.06	9.99
3	-3.07	3.67	118.46	8.18	52.24	9.39	38.29	13.33	29.22
4	-3.68	49.05	5.69	329.11	8.71	44.14	10.51	33.05	13.23
5	-3.78	5.68	50.15	9.17	366.92	11.89	45.19	14.98	33.68
6	-4.33	36.41	7.92	44.63	10.68	547.50	13.41	38.46	15.23
7	-4.37	7.77	36.74	11.46	44.35	13.28	513.83	17.40	38.19
8	-4.75	24.30	9.02	30.15	11.24	34.68	12.63	757.00	15.81
9	-4.76	9.22	25.09	12.34	30.30	14.32	35.51	17.65	742.25

The resulting numerical influence matrix is given in Table 3. This matrix is symmetric, whereas the experimental matrix is slightly un-symmetric, probably due to manufacturing errors. For the plain weave, E_1 = 34.8 GPa, ν_{12} = 0.41, and G_{12} = 2.34 GPa. For the uni-directional battens, E_1 = 317.2 GPa, ν_{12} = 0.31, and G_{12} = 1.05 GPa. The model correctly predicts the very stiff leading edge (point 1), and the negative influence it has on the remainder of the wing (as shown on the right of Figure 7). The rest of the points along the wing positively influence one another. Errors between the two matrices are typically on the order of ± 5-10%; the numerical wing is generally stiffer than the actual wing. As expected, the weakest battens are the longest, found towards the root (points 8 and 9). The wingtips (points 2 and 3) generally have the greatest indirect influence on the rest of the wing (as shown on the left of Figure 7). Force-displacement trends at the nine locations along the wing, due to loads at those points (the diagonal terms in the matrices) are given in Figure 8, showing a suitable match between model and experiment. With the exception of the leading edge, two data points are given for each load level, corresponding to the data from the left and right sides of the wing. Higher fidelity methods for system identification of a carbon fiber MAV skeleton are given by Reaves et al. [106], who utilize model update techniques with uncertainty quantification methods. This is largely done due to the uncertainty in the laminate lay-up, predominately in ply overlapping regions within the skeleton, which is not an issue for the current work.

Table 3. Numerical influence matrix (mm/N) at points labeled in Figure 7.

	1	2	3	4	5	6	7	8	9
1	1.49	-2.92	-2.92	-3.61	-3.61	-4.24	-4.24	-4.60	-4.60
2	-2.92	107.96	3.36	54.49	5.05	33.10	6.80	20.84	8.13
3	-2.92	3.36	107.96	5.05	54.49	6.80	33.10	8.13	20.84
4	-3.61	54.49	5.05	312.00	6.78	39.30	8.51	25.09	9.73
5	-3.61	5.05	54.49	6.78	312.00	8.51	39.30	9.73	25.09
6	-4.24	33.10	6.80	39.30	8.51	584.26	10.14	28.81	11.18
7	-4.24	6.80	33.10	8.51	39.30	10.14	584.26	11.18	28.81
8	-4.60	20.84	8.13	25.09	9.73	28.81	11.18	776.48	11.95
9	-4.60	8.13	20.84	9.73	25.09	11.18	28.81	11.95	776.48

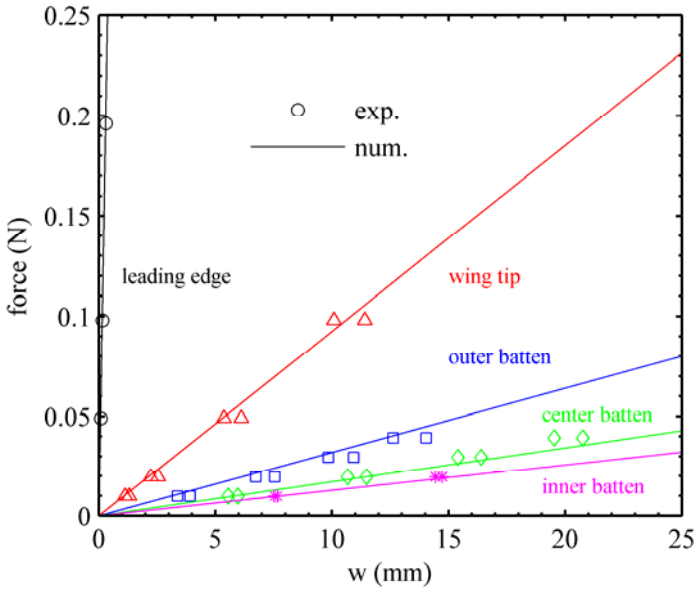

Figure 8. Compliance at various locations along the wing, due to a point load at those locations.

3.1.2. Membrane Modeling

In the modeling of thin, elastic membranes (with no resistance to a bending couple), four basic options are available. If there exists a significant pre-strain field throughout the sheet, linear modeling is possible by assuming inextensibility: the pre-strain overwhelms the strains that develop as a result external loading. As these strains grow in magnitude (or if the membrane is originally slack) a nonlinear model must be used, as the membrane's resistance depends upon the loading (geometric nonlinearity). However, a linear constituitive relationship is still typically valid up to a point, after which the membrane becomes hyperelastic (material nonlinearity), and the stress-strain relationship changes with increasing load. Finally, in the event of excessive compressive stresses or shear, one or more of the principle stresses may become zero, at which point a wrinkling module must be included in the structural model.

3.1.2.1. Linear Modeling

Geometric stress stiffening provides a relationship between in-plane forces and transverse deflection [105], and is indicative of a structure's reluctance to change its state of stress. For an initially flat membrane with a transverse pressure, the constitutive equation is:

$$N_x \cdot w_{,xx} + 2 \cdot N_{xy} \cdot w_{,xy} + N_y \cdot w_{,yy} + p = 0 \tag{4}$$

where w is the out-of-plane displacement (as above), N_x, N_{xy}, and N_y are the in-plane pre-stress resultants, and p is the applied pressure field. For an isotropic stress field with no shear, this equation reduces to the well known Poisson's equation [107]. This model assumes that the displacement along the membrane is purely out-of-plane; thus the membrane is inextensible in response to a pressure field (although extensibility is needed to apply the initial pre-stress field). The resulting finite element model is fairly inexpensive, as each node has only one degree of freedom, and standard direct linear solvers can be used. This model is thought to be accurate for small pressures, small displacements, and large pre-stresses. Though it is not expected that the MAV wing displacements will be particularly large (typically less than 10% of the root chord), it is expected that a slack membrane skin may provide significant aerodynamic advantages. As the solution to Eq. (4) becomes unbounded as the pre-stress approaches zero, higher fidelity models will be pursued for the current work. MAV simulations with linear membrane models can be found in the work of Stanford and Ifju [27] and Sugimoto [44], as noted in the second column of Table 1.

3.1.2.2. Nonlinear Modeling

The nonlinear membrane modeling discussed in this section will incorporate geometric nonlinearities, but Hooke's law is assumed to still be valid. For the inflation of a circular membrane, Pujara and Lardner [43] show that linear and hyperelastic constituitive relationships provide the same numerical solutions up to deformations on the order of 30% of the radius, a figure well above the deflections expected on a membrane wing. Geometric nonlinearity implies that the deformation is large enough to warrant finite strains, and that the direction of the non-conservative pressure loads significantly changes with deformation. Eq. (4) is still valid, only now the stress resultants depend upon the state of pre-stress, as well as in-plane stretching, which in turn depends on the out-of-plane displacement. Furthermore, the rotation of the membrane is no longer well-approximated by the derivative of w, rendering the equilibrium equation nonlinear. Three displacement degrees of freedom are required per node (u, v, w), rather than the single w used above. Finite element implementation of such a model is described by Taylor et al. [108] and Pauletti et al. [109].

The strain pseudo-vector within each element is given as:

$$\boldsymbol{\varepsilon} = \boldsymbol{\varepsilon}_o + \boldsymbol{\varepsilon}_L = \mathbf{B}_o \cdot \mathbf{X}_e + \mathbf{B}_L \cdot \mathbf{X}_e \tag{5}$$

where $\boldsymbol{\varepsilon}_o$ and $\boldsymbol{\varepsilon}_L$ represent the division of the linear (infinitesimal) and nonlinear contributions to the Green-Lagrange strain, $\mathbf{X}_e$ is a vector of the degrees of freedom in the elements (three displacements at the three nodes), and $\mathbf{B}_o$ and $\mathbf{B}_L$ are the appropriate strain-displacement matrices (the latter of which depends upon the nodal displacements) [100]. The pre-stress (if any) can be included into the model in one of two methods. First, they can be simply added to the stresses computed my multiplying the strain vector of Eq. (5) through the constituitive matrix. This may cause problems if the imposed pre-stress distribution does not exactly satisfy equilibrium conditions, or if there is excessive curvature in the membrane skin: the membrane will deform, even in the absence of an external force.

A second option is to use the pre-stresses in a finite element implementation of Eq. (4), then add the resulting stiffness matrix and force vectors to the nonlinear terms. For a flat membrane with uniform pre-stress, the two methods are identical. The internal force in each element $\mathbf{P}_e$ can be computed from the principle of virtual work:

$$\mathbf{P}_e = \mathbf{T} \cdot \int_{V_o} \left[\mathbf{B}_o + \partial\left(\mathbf{B}_L \cdot \mathbf{X}_e\right)/\partial \mathbf{X}_e \right]^T \cdot \mathbf{A}_m \cdot \boldsymbol{\varepsilon} \cdot dV + \mathbf{T} \cdot \mathbf{K}_w \cdot \mathbf{X}_e \tag{6}$$

where $\mathbf{A}_m$ is the linear constitutive elastic matrix of the membrane, $\mathbf{A}_m \cdot \boldsymbol{\varepsilon}$ is the stress pseudo-vector within each element, and $\mathbf{K}_w$ is the stiffness matrix representation of Eq. (4), containing only terms related to the out-of-plane displacement w. The tangential stiffness matrix $\mathbf{K}_e$ is then given as the sum of the geometric $\mathbf{K}_\sigma$, constituitive $\mathbf{K}_c$, external $\mathbf{K}_{ext}$ and pre-stress stiffness matrix $\mathbf{K}_w$:

$$\mathbf{K}_\sigma = \mathbf{T} \cdot \int_{V_o} \mathbf{G}^T \cdot \mathbf{M} \cdot \mathbf{G} \cdot dV \cdot \mathbf{T}^T \tag{7}$$

$$\mathbf{K}_c = \mathbf{T} \cdot \int_{V_o} \left[\mathbf{B}_o + \partial\left(\mathbf{B}_L \cdot \mathbf{X}_e\right)/\partial \mathbf{X}_e \right]^T \cdot \mathbf{A}_m \cdot \left[\mathbf{B}_o + \partial\left(\mathbf{B}_L \cdot \mathbf{X}_e\right)/\partial \mathbf{X}_e \right] \cdot dV \cdot \mathbf{T}^T \tag{8}$$

$$\mathbf{K}_{ext} = -\partial \mathbf{F}_e / \partial \mathbf{X}_e \tag{9}$$

where **G** is a matrix linking the nodal degrees of freedom to a displacement gradient vector [110], **M** is a stress matrix whose elements can be found in [105], and $\mathbf{F}_e$ is the external force vector. Computation of the skew-symmetric external stiffness matrix is given in [109]. $\mathbf{F}_e$ must be written in the unknown deformed configuration:

$$\mathbf{F}_e = \mathbf{T} \cdot (p \cdot A/3) \cdot \left[\mathbf{I} \quad \mathbf{I} \quad \mathbf{I}\right]^T \cdot \mathbf{n} \tag{10}$$

where A is the deformed area of the triangle, p is the uniform pressure over the element, **I** is the identity matrix, and **n** is the unit normal vector to the deformed triangular finite element. The resulting non-linear set of equations is solved with Newton's recurrence formula [109].

The above method essentially separates the linear and nonlinear stiffness contributions. If the pre-stress in the membrane is very large, $\mathbf{K}_w$ will overwhelm its nonlinear counterparts, and membrane response will be essentially linear for small pressures and displacements. Continued inflation will transition from linear to nonlinear response [111]. In the event of a slack membrane, the membrane's initial response to a pressure will have an infinite slope until strains develop and provide stiffness. Numerous membrane wing models use some variant of the geometrically nonlinear model described above: Stanford et al. [63], Ormiston [33], Smith and Shyy [93], Jackson and Christie [88], and Levin and Shyy [94], and Gordnier [95], as noted in the third column of Table 1.

3.1.2.3. Higher Fidelity Structural Modeling

Latex rubber is technically a hyperelastic incompressible material with a nonlinear stress-strain curve. A linear approximation of this curve for small strains allows for the linear-elastic formulation given above. For higher deformations, the material nonlinearity must be considered. Most hyperelastic models use a phenomenological approach, wherein the strain energy is written as a general polynomial of the invariants of the deformation tensor. The multiplying constants and exponential powers are curve fit parameters. Though many such models exist, the Mooney-Rivlin model [112] is the most popular, due to relative ease of use (only two terms are included in the strain energy) and good accuracy up to 150% strain. Finite element implementation of such a model is discussed by Oden and Sato [113] and Wu et al. [110]. Use of hyperelastic models for membrane wing simulations can be found in the work of Schoop et al. [90], Lian et al. [30], and Persson et al. [29], as noted in the fourth column of Table 1. It is thought that the geometrically nonlinear model will give identical results to a hyperelastic model, for the range of deformation expected on a membrane MAV wing [43], and is not used for the current work.

Wrinkling may also be a concern: this is a rippling in the membrane skin due to a compressive stress or excessive shearing [45]. While, as will be discussed below, a wrinkling module could be an insightful addition, the computational cost is prohibitive and is not used here. Aeroelastic modeling with wrinkling as pertaining to membrane wings is given in the work of Smith and Shyy [89] and Heppel [45].

3.1.2.4. Inflatable Diaphragm Validation

In order to validate the above membrane models, the material properties of the latex are first identified with a uni-axial tension test. The test specimen has a width of 20 mm, a length of 120 mm, and a thickness of 0.12 mm. The latex rubber sheets are formed in a rolling process, implying an orthotropy, though specimens cut from different orientations yield very similar results. VIC is used to monitor both the extensional and the Poisson strains: data is sampled at 50 pixel locations within the membrane strip, and then averaged. The resulting data can be seen in Figure 9, and is used to identity the linear elastic modulus and the Poisson's ratio. A linear fit through the stress-strain curve results in a modulus of 2 MPa; the nonlinear stress-softening behavior for higher strains is the hallmark of hyperelasticity [114]. The Poisson's ratio for small strains is 0.5, a result of the material's incompressibility.

Using these material parameters to construct the constitutive matrix $\mathbf{A}_m$, the finite element model can be appropriately validated with the Hencky-Campbell test [110]: a flat circular membrane (with or without pre-tension), clamped along its boundary, and subjected to a uniform pressure. A 57.15 mm radius is chosen in order to emulate the length scale of a micro air vehicle. Although the problem is axisymmetric, a full circular mesh is used for numerical computations. Experimentally, VIC is used to monitor the shape of the membrane, while a Heise pressure transducer measures the pressure within a chamber, to the top of which the membrane sheet is fixed. Results are given in Figure 10, in terms of the displacement of the membrane center (normalized by the radius) versus pressure. Numerical data is computed with the geometrically nonlinear model, without hyperelasticity.

Two cases are considered: a slack membrane, and a taut membrane. As expected, the response of the slack membrane to an applied pressure is at first unbounded, but becomes finite with the advent of the extensional strains. The correlation between model and experiment is adequate up to w/R = 0.22 (slightly lower than the value given by Pujara and Lardner [43]), and the model begins to under-predict the inflated shape. Hyperelastic effects appear after

this point: Hooke's law over-predicts the stress for a given strain level (Figure 9), and thus the membrane's resistance to a transverse pressure. For the case with membrane pre-tension, VIC is used to measure the pre-strain in the membrane skin (applied radially [115]), the average of which is then used for finite element computations. The mean pre-strain is 0.044, with a coefficient of variation of 3.1%. Both model and experiment indicate that the membrane deformation is linear up to w/R = 0.15. The response then becomes nonlinear, due to the advent of finite strains, but also because a relevant portion of the uniform non-conservative pressure is now directly radially, rather than vertically. Model and experiment now diverge at w/R = 0.3: the addition of a pre-tension field essentially increases the range of validity of the membrane model detailed in Section 3.1.2.2.

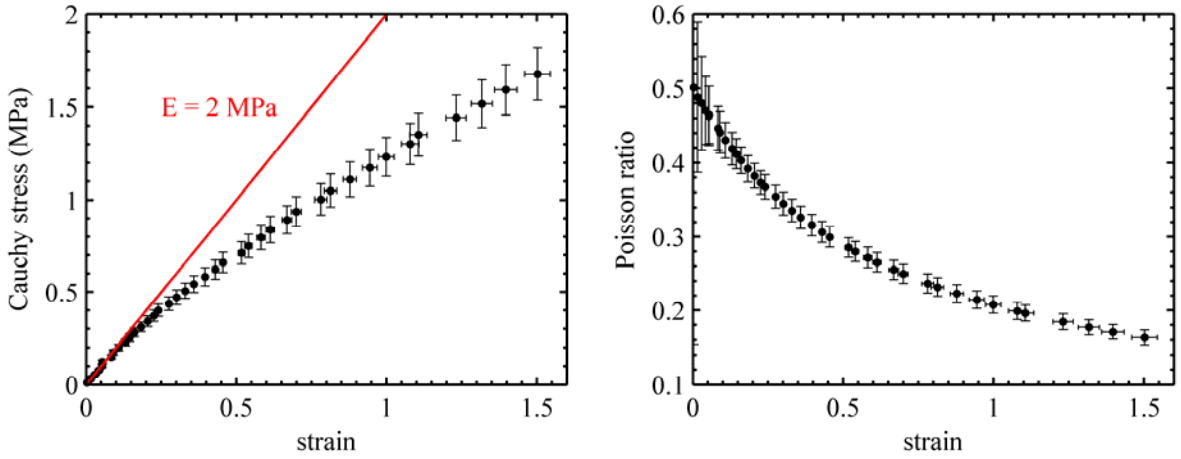

Figure 9. Uni-axial stretch test of a latex rubber membrane.

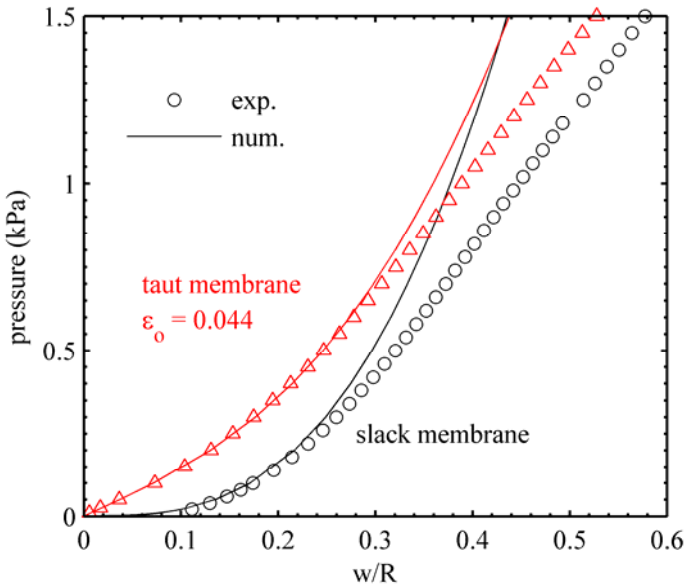

Figure 10. Circular membrane response to a uniform pressure.

3.1.3. Skin Pre-Tension Considerations

A state of uniform membrane pre-tension, though numerically convenient [33], [44], [27], is essentially impossible to actually fabricate on a MAV wing. One reason is that the latex sheets used on the MAVs in this work are not much wider than the wingspan, subjecting the state of pre-stress to end-effects. This may perhaps be remedied with larger sheets and a biaxial tension machine, which hardly seems worth the effort for MAV construction. Another problem is the fact that the wing is not a flat surface. Even if a state of uniform pre-tension were attainable, it cannot be transferred to the wing without significant field distortions, particularly due to the

camber in the leading edge. A typical pre-strain field is given in Figure 11, as measured by the VIC system off of a BR wing in the chordwise direction. The contour on the left is the pre-strain field after the spray adhesive has dried, but before the latex surrounding the wing has been de-pinned from the stretching frame (as discussed in section 2.5). The contour on the right of Figure 11 is the pre-strain after the excess latex has been trimmed away.

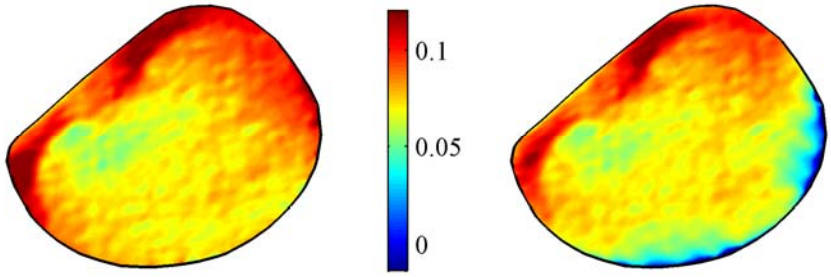

Figure 11. Measured chordwise pre-strains in a BR wing before the tension is released from the latex (left), and after (right).

The pre-strains measured from the carbon fiber areas of the wing (leading edge, root, battens) are meaningless, as the shell mechanics largely govern the response in these areas. The large extensional strains (~12%) at the leading edge are indicative of the fact that the wing skeleton is flattened against the membrane until the spray glue dries. At this point, the wing is allowed to re-camber, causing the latex adhered to its top surface to stretch. The anisotropic nature of the pre-tension field is very evident, with strains ranging from between 5% to 8% on the left semi-wing (in the membrane portion) and slightly higher on the right. Furthermore, when the surrounding latex is de-pinned from its frame the membrane at the trailing edge contracts, leaving an area of almost no tension (right side of Figure 11). This is a result of the BR wing's free trailing edge, and would not be a problem with a PR wing.

One numerical solution to such a problem is to interpolate the data of Figure 11 onto the finite element grid, and compute the pre-stress within each element, as discussed by Stanford et al. [63]. This method, though accurate, would require an experimental VIC analysis in conjunction with every numerical analysis; not a cost-effective method for thorough exploration of the design space. Eq. (4) however, is a natural smoothing operator [107]; simply averaging the pre-strains for the computations, though crude, can in some cases be relatively accurate. The match between measured and predicted membrane deformation for the taut case in Figure 10 is very good, despite the fact that the numerical pre-strains were presumed uniform. The error resulting from a uniform pre-stress assumption can be estimated with the following method. The pre-strain distribution throughout a flat circular membrane is considered a normally-distributed random variable: each finite element has a different pre-strain. The linear membrane model of Eq. (4) is then used to compute the displacement at the center of the membrane due to a hydrostatic pressure. The same membrane is then given a constant pre-strain distribution (the average value of the randomly-distributed pre-strain), and the central deflection is recomputed for comparison purposes. Monte Carlo simulations are then used to estimate the average error at the membrane center, for a given coefficient of variation of the membrane pre-strain.

The results of the Monte Carlo simulation are given in Figure 12. Each data point is the percentage error between the central displacement computed with a non-homogenous random pre-strain, and that with a constant pre-strain. Each error percentage is the average of 500 finite element simulations. The radius of the circle is 57.15 mm, the thickness is 0.12 mm, the elastic modulus is 2 MPa, the Poisson's ratio is 0.5, and the hydrostatic pressure is fixed at 200 Pa. The mean pre-strain is 0.05, and the standard deviation is decided by the COV of each data point's abscissa. Nonlinear membrane modeling is not used. The smoothing nature of the Laplacian operator in Eq. (4) is very evident: even in the presence of 30% spatial pre-strain variability, the error in assuming a constant pre-strain is still less than 5%. On one hand, the error in Figure 12 is probably under-predicted, as strain cannot truly be a spatially-random variable: on a local scale measured strain may seem random, but on a global scale it must satisfy the compatibility equations [114]. Both of these scale-trends are evident in Figure 11. On the other hand, Figure 12 represents the worst case scenario, as nonlinear membrane effects will dilute the importance of the pre-tension [111], whatever it's distribution throughout the membrane skin.

Though the above results indicate the appropriateness of using a constant membrane pre-stress for MAV wing computations (despite an inability to reproduce this in the laboratory), the tension relaxation at the free trailing edge of the BR wing (seen in Figure 11) should be corrected for. Regardless of the amount of pre-tension placed in a

batten-reinforced membrane, the pre-stress traction normal to the free trailing edge will always be zero, producing a stress gradient. This can be accounted for in the following manner:

1. Specify the pre-stress field within the membrane skin (uniform or otherwise).
2. Compute the traction due to this pre-stress along the outward normal, at each edge in a membrane finite element that coincides with a free surface.
3. Apply a transverse pressure along each edge, equal and opposite to the computed traction.
4. Compute the resulting stress field (while holding the carbon fiber regions of the wing rigid), add this field to the prescribed stress in step 1, and use the result as the new pre-stress resultant field for aeroelastic computations.

The resulting pre-stress field will be very small along the free edge, and approach the original specified value deeper into the wing towards the leading edge, as can be seen in Figure 13. For this example, about a fourth of the membrane area is affected by the free edge, while the remainder retains a pre-stress close to the prescribed value (a result validated by Figure 11). As mentioned above, this pre-stress correction only needs to be applied for simulations of a batten-reinforced wing.

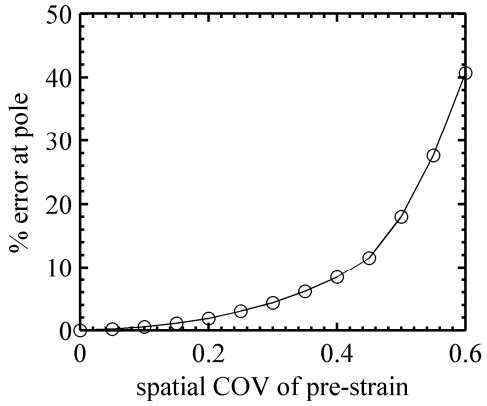

Figure 12. Monte Carlo simulations: error in the computed membrane deflection due to a spatially-constant pre-strain distribution assumption.

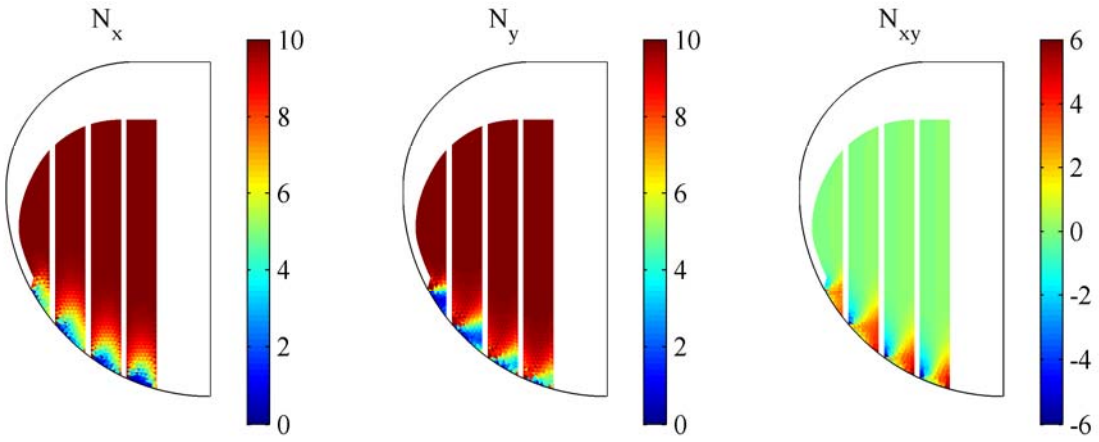

Figure 13. Computed pre-stress resultants (N/m) in the chordwise (left), spanwise (center), and shear (right) in a BR wing, corrected at the trailing edge for a uniform pre-stress resultant of 10 N/m.

3.2. Fluid Solver

The three-dimensional incompressible Navier-Stokes equations, written in curvilinear coordinates, are solved for the steady, laminar flow over a MAV wing. As before, the fuselage, stabilizers, and propeller are not taken into account. The computational domain can be seen in Figure 14, with the MAV wing enclosed within. Inlet and outlet boundaries are marked by the flow vectors; velocity is specified at the inlet, and a zero-pressure boundary condition is enforced at the outlet. The configuration shown in Figure 14 is for simulations at a model inclination of

0° angle of attack. For non-zero angles, the lower and upper surfaces will also see a mass flux, rather than re-meshing the wing itself. The sidewalls are modeled as slip walls, and thus no boundary layer forms. The MAV wing itself is modeled as a no-slip surface.

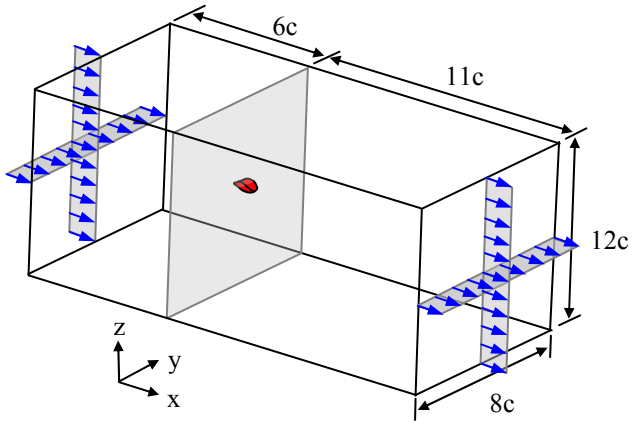

Figure 14. CFD computational domain.

Because no flow is expected to cross the root-chord of the wing (unsteady effects that may lead to bilateral asymmetry [19] are not included; nor is propeller slipstream [116]), symmetry is exploited by modeling only half of the computational domain (the plane of symmetry is also modeled as a slip wall). A schematic view of the resulting structured mesh (the nodes that lie on the plane of symmetry and the MAV wing) [63] is given in Figure 15. The wing itself has no thickness. Though the unstructured mesh of Figure 15 is adequate for the wing-only computations presented here, simulations of an entire vehicle will significantly increase the geometrical complexity, and unstructured grids may then be favorable [116].

Such a flow model is expected to adequately predict the strong tip vortex swirling system (and the accompanying nonlinear lift and moment curves: the swirling leaves low-pressure cells at the wing tip, which grow as a function of angle of attack [16]), as well as the flow separation against an adverse pressure gradient [117]. Similar laminar, steady flow computations for low Reynolds number flyers can be found in the work of Smith and Shyy [91], Viieru [118], and Stanford et al. [63].

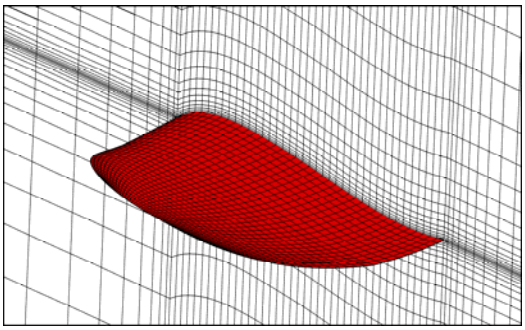

Figure 15. Detail of structured CFD mesh near the wing surface.

For the range of Reynolds numbers expected over a fixed-wing micro air vehicle (10^4 - 10^5), the flow may experience laminar-turbulent transition aft of the separation point. Current state-of-the-art flow modeling (discussed below) does not yet encompass computation of low Reynolds number three-dimensional transitional flow in an efficient manner, and so the modeler is frequently faced with the choice of purely laminar or turbulent modules. The use of both models for the computational domain of Figure 14 (with a K-ε model and a standard wall function for the turbulent case) is seen to result in very similar lift and drag computations at a Reynolds number of 70,000, with good agreement with experimental data [27]. The laminar computations are favored, as they are able to capture the large recirculation zones (verified experimentally by Sytsma [42]) over the wing, whereas the turbulent model cannot (velocity profile is assumed linear in the viscous sublayer). Kunz and Kroo [119] similarly advocate the use

of fully-laminar models over fully-turbulent, for the range of Reynolds numbers considered here.

The flow in the free-shear layer aft of the separation point is highly susceptible to transition however [117]. A fully laminar model is generally acceptable for low and moderate angles of attack, and lower Reynolds numbers [12]. Above $5 \cdot 10^4$, the turbulent entrainment of flow from the free-stream may cause the flow to reattach [50]. Referring to the comparison of experimental data and laminar computations over an Eppler 387 airfoil given by Lin and Pauley [28], the laminar CFD faithfully reproduces lift, drag, separation point, and bubble length for a range of Re and low-to-moderate angles of attack. At 7º and Re = 10^5 however, the bubble length (and thus drag) is over-predicted, presumably because flow transition prompts a quicker reattachment. Similar laminar CFD prediction limitations are given for three-dimensional flows by Stanford et al. [63], where drag is generally over-predicted for high angles of attack (though lift is accurate throughout, similar to that seen by Lin and Pauley [28]). This behavior can reach extremes for certain combinations of airfoil and Re, where a zig-zag pattern is found in the drag polar [12]. Increased turbulence at large incidence can lead to quick reattachment, and a sharp drop in drag. Fully laminar models are similarly unable to compute both lower and upper branches of a hysteresis loop [120].

3.2.1. Governing Equations

In order to handle the arbitrarily shaped geometries of a micro air vehicle wing with passive shape adaptation, the Navier-Stokes equations must be transformed into generalized curvilinear coordinates: $\xi(x,y,z)$, $\eta(x,y,z)$, $\zeta(x,y,z)$. This transformation is achieved by [119]:

$$\begin{bmatrix} \xi_x & \xi_y & \xi_z \\ \eta_x & \eta_y & \eta_z \\ \zeta_x & \zeta_y & \zeta_z \end{bmatrix} = \frac{1}{J} \cdot \begin{bmatrix} f_{11} & f_{12} & f_{13} \\ f_{21} & f_{22} & f_{23} \\ f_{31} & f_{32} & f_{33} \end{bmatrix} \tag{11}$$

where f_{ij} are metric terms, and J is the determinant of the transformation matrix:

$$J = \frac{\partial(x,y,z)}{\partial(\xi,\eta,\zeta)} \tag{12}$$

Using the above information, the steady Navier-Stokes equations can then be written in three-dimensional curvilinear coordinates [122]. The continuity equation and u-momentum equation are presented here in strong conservative form, with the implication that the v- and w-momentum equations can be derived in a similar manner.

$$U_\xi + V_\eta + W_\zeta = 0 \tag{13}$$

$$\begin{aligned} &\frac{\partial(\rho \cdot U \cdot u)}{\partial\xi} + \frac{\partial(\rho \cdot V \cdot u)}{\partial\eta} + \frac{\partial(\rho \cdot W \cdot u)}{\partial\zeta} = \frac{\partial}{\partial\xi}\left[\frac{\mu}{J} \cdot \left(q_{11} \cdot u_\xi + q_{12} \cdot u_\eta + q_{13} \cdot u_\zeta\right)\right] \\ &+ \frac{\partial}{\partial\eta}\left[\frac{\mu}{J} \cdot \left(q_{21} \cdot u_\xi + q_{22} \cdot u_\eta + q_{23} \cdot u_\zeta\right)\right] + \frac{\partial}{\partial\zeta}\left[\frac{\mu}{J} \cdot \left(q_{31} \cdot u_\xi + q_{32} \cdot u_\eta + q_{33} \cdot u_\zeta\right)\right] \\ &- \left[\frac{\partial(f_{11} \cdot p)}{\partial\xi} + \frac{\partial(f_{21} \cdot p)}{\partial\eta} + \frac{\partial(f_{31} \cdot p)}{\partial\zeta}\right] \end{aligned} \tag{14}$$

where ρ is the density, p is the pressure, μ is the viscosity, q_{ij} are parameters dictated by the transformation (expressions can be found in [122]), and U, V, and W are the contravariant velocities, given by the flux through a control surface normal to the corresponding curvilinear directions:

$$\begin{aligned} U &= f_{11} \cdot u + f_{12} \cdot v + f_{13} \cdot w \\ V &= f_{21} \cdot u + f_{22} \cdot v + f_{23} \cdot w \\ W &= f_{31} \cdot u + f_{32} \cdot v + f_{33} \cdot w \end{aligned} \tag{15}$$

In order to numerically solve the above equations, a finite volume formulation is employed, using both

Cartesian and contravariant velocity components [119]. The latter can evaluate the flux at the cell faces of the structured grid and enforce the conservation of mass. A second order central difference operator is used for computations involving pressure/diffusive terms; a second order upwind scheme handles all convective terms [123].

3.2.2. Higher Fidelity Fluids Modeling

A challenging and important aspect of fluid modeling is to accommodate unsteady laminar-turbulent transitional flows. As discussed above, the fully-laminar assumption can over-predict bubble lengths and drag, though lift is generally accurate [28]. A large amount of numerical work is available concerning two-dimensional transitional flows, as reviewed by Lian and Shyy [20]: available techniques include fixing the separation point from experimental observations and empirical methods based on local Reynolds number, shape factor, or turbulence levels. Lian and Shyy couple an incompressible RANS solver to the e^N method. The latter technique solves the Orr-Sommerfeld equation to monitor unstable growth rate of Tollmien-Schlichting waves; transition occurs when the least stable amplitude crosses a certain threshold [20].

Krumbein [124] utilizes a similar method for three-dimensional flows. He identities the e^N method as current state-of-the-art for transition prediction in many industrial applications due to a practical computational cost, though a number of fundamental aspects of the process are not included. A higher level of fidelity can be obtained with LES simulations, as discussed by Roberts and Yaras [125] for transitional separated flows. State-of-the-art without computational cost considerations involves DNS simulations, which can be found in the work of Shan et al. [126], for the three-dimensional flow over a NACA0012 wing at 6º angle of attack, for a Reynolds number of 10^5. The laminar shear layer first separates in a two-dimensional manner, followed by slight distortions in the spanwise vorticity. This leads to fully three-dimensional fluctuations, vortex shedding, and transition, followed by reattachment.

3.3. Aeroelastic Coupling

Transfer of data between the structured CFD mesh of Figure 15 and the unstructured FEA mesh of Figure 6 is done with simple polynomial interpolation. If information from grid A is to be interpolated to grid B, the element from grid A (triangular for the FEA mesh, quadrilateral for the CFD mesh) is found which is closest to each node from grid B. Except for nodes that lie on the wing border, these elements will enclose their corresponding nodes. Polynomial shape functions for the desired variable are formulated to describe its distribution within the element, and then the value at the node is solved for. Such a method is found to adequately preserve the integrated forces and the strain energies from one mesh to another, and is fairly inexpensive. A review of aeroelastic interfacing techniques is given by Guruswamy [127].

The un-deformed (due to aerodynamic loads) wing shape technically depends upon the membrane pre-tension. This shape could be found with Eq. (4), setting the pressure source terms to zero, and letting the wing shape at nodes upon the carbon fiber-latex boundary be prescribed displacement boundary conditions. Such a scheme should result in slight concavities along the membrane surface [128]. This effect is considered small, however, and is ignored for the current work. Viscous shear stress over the wing is also not included in the aeroelastic coupling. Though shear has been surmised to be an important factor in the stability of flags in flow [77], it is expected to be a secondary effect here.

3.3.1. Moving Grid Technique

In order to re-mesh the multi-block structured CFD grid for aeroelastic computations, a moving grid routine based upon the master-slave concept is used to maintain a point-matched grid block interface, preserve grid quality, and prevent grid cross-over [30]. Master nodes are defined as grid points that lie on the moving surface (the wing surface of the micro air vehicle, in this case), while the slave nodes constitute the remaining grid points. A slave node's nearest surface point is defined as its master node, and its movement is given by:

$$\tilde{x}_s = x_s + \omega \cdot \left(\tilde{x}_m - x_m \right) \tag{16}$$

where x_s is the location of the slave node, x_m is the location of its master node, the tilde indicates a new position, and ω is a Gaussian distribution decay function:

$$\omega = \exp\left[-\beta \cdot \min\left\{ 500, \frac{\left(x_s - x_m\right)^2 + \left(y_s - y_m\right)^2 + \left(z_s - z_m\right)^2}{\left(\tilde{x}_m - x_m\right)^2 + \left(\tilde{y}_m - y_m\right)^2 + \left(\tilde{z}_m - z_m\right)^2 + \eta} \right\} \right] \tag{17}$$

where η is small number to avoid division by zero, and β is a stiffness coefficient; larger values of β promote a more rigid-body movement. Further information concerning this technique is given by Kamakoti et al. [129].

3.3.2. Numerical Procedure

The steady fluid structure interaction of a flexible MAV wing computed by Stanford et al. [63] is summarized in the following:

1. If computations involve a batten-reinforced wing, correct for the membrane pre-tensions at the free trailing edge.
2. Solve the 3-D, incompressible Navier-Stokes equations for the steady laminar flow field.
3. Interpolate the computed wing pressures from the CFD grid (Figure 15) to the FEA grid (Figure 6).
4. Solve for the resulting wing displacement using the structural membrane/carbon fiber model.
5. Interpolate the displacement onto the MAV wing of the CFD grid.
6. Re-mesh the CFD grid using the master/slave moving grid scheme.
7. Repeat steps 2-6 until suitable convergence is achieved: less than 0.1% change in maximum displacement.

Less than ten iterations are usually adequate at modest angles of attack ($3^\circ<\alpha<18^\circ$). Typical results are given in Figure 16 for the lift and efficiency of both a BR and a PR wing. The lift of the PR wing monotonically converges (lift increases camber, which further increases lift), while the history of a BR wing is staggered (lift decreases wing twist, decreasing lift). Step 2 requires between 150 and 250 sub-iterations, while step 4 can typically converge within 20 sub-iterations.

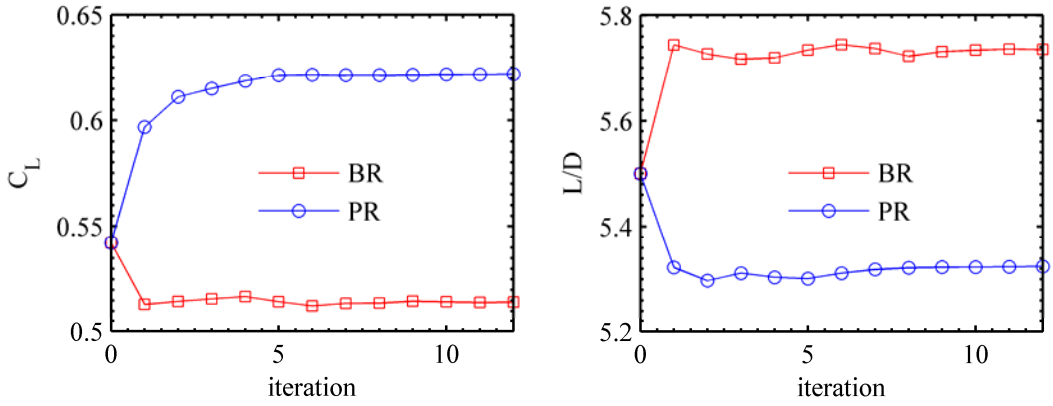

Figure 16. Iterative aeroelastic convergence of membrane wings at $\alpha = 9^\circ$.

4. Baseline Design Performance

Three "baseline" micro air vehicle wing designs are considered in this section: first, a completely rigid wing. Secondly, a batten-reinforced wing with no pre-tension in the membrane skin, two layers of bi-directional carbon fiber at ply angles of 45º to the chord line (at the root and leading edge), and one layer of uni-directional carbon fiber (fibers aligned in the chordwise direction) for the battens. Third, a perimeter-reinforced wing with no pre-tension in the membrane skin and two layers of bi-directional carbon fiber at ply angles of 45º to the chord line (at the root, leading edge, and perimeter). All results, unless indicated otherwise, are found at $U_\infty = 15$ m/s, a value towards the upper range of MAV flight (equating to a Reynolds number of $1.1 \cdot 10^5$). A higher velocity is chosen to emphasize aeroelastic deformations. Computational results are gathered with the aforementioned steady laminar Navier-Stokes solver coupled to the geometrically nonlinear membrane solver and the linear orthotropic plate solver. Experimentally, 10 VIC images are taken of the deformed wing (at 1 Hz) and averaged together for a given flight condition. Sting balance results are sampled at 1000 Hz for 2 seconds, and then averaged.

4.1. Wing Deformation

Numerical and experimental out-of-plane displacements, normalized by the root chord, are given in Figure 17 for a BR wing, along with a section of the data at x/c = 0.5, at 15º angle of attack. As expected, the primary mode of wing deformation is a positive deflection of the trailing edge, resulting in a nose-down twist of each flexible wing section. Deformations are relatively small (~5%, or 6.2 mm), though still have a significant effect upon the aerodynamics. The membrane inflates from between the battens (clearly seen in the section plot) towards the leading edge, but at the trailing edge the wing shape is more homogenous and smooth, and no distinction between batten and membrane can be made. This is presumably due to the pressure gradient, with very high forces at the

leading edge which dissipates down the wing. The carbon fiber wing tips, though several orders of magnitude stiffer than the membrane, shows appreciable twisting, indicative of the large suction forces from the tip vortex. Correlation between model and experiment is acceptable, with the model slightly under-predicting the adaptive washout, and over-predicting the local membrane inflation between the battens. Wing shapes and magnitudes match well with time-averaged results reported by Lian et al. [30].

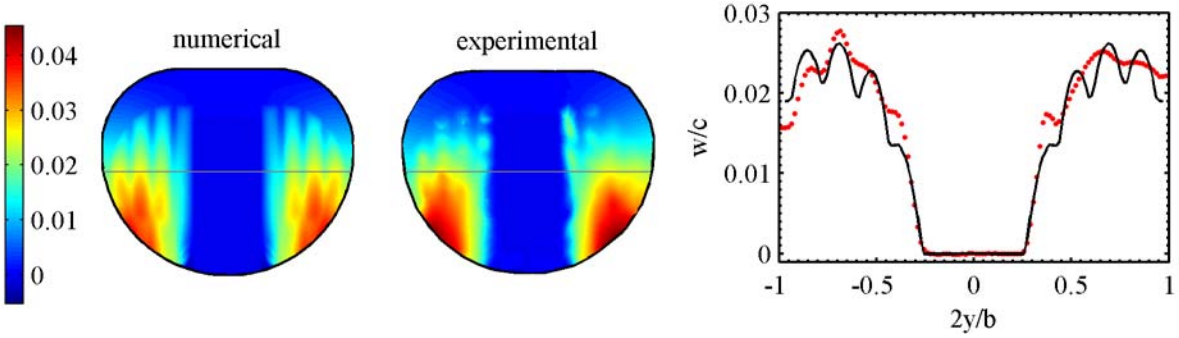

Figure 17. Baseline BR normalized out-of-plane displacement (w/c), α = 15º.

Chordwise strains for the same case as above can be seen in Figure 18. The directional stiffness of the battens generally prevents significant stretching in the chordwise direction. The model predicts appreciable strain (1.4%) at the carbon fiber/membrane interface towards the leading edge (due to inflation), almost no strain near the mid-chord region, and negative Poisson strains at the trailing edge. Strains in the carbon fiber regions, while computed, are much smaller than the membrane strains, and cannot be discerned in Figure 18. The measured chordwise strain is very small and noisy, with no evident differences between the carbon fiber and membrane regions. Much of the measured field lies below the system's strain resolution (~1000 με). Several noise spikes are also evident in this strain field, while the displacement field in Figure 17 has none; the strain differentiation procedure is more sensitive to experimental noise than the displacement temporal matching.

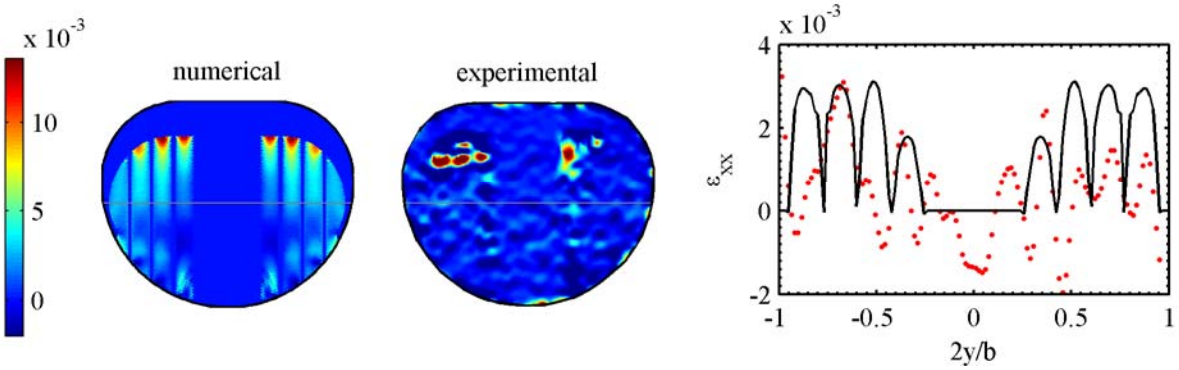

Figure 18. Baseline BR chordwise strain (ε_{xx}), α = 15º.

A better comparison between model and experiment is given in Figure 19, with the spanwise strains. These extensions are essentially a product of the change in distance between the battens as they deform. Both model and experiment indicate a peak in ε_{yy} between the inner batten and the carbon fiber root, though the model indicates this maximum towards the leading edge (~1.2%), while the measurement places it farther aft. Strain concentrations at the trailing edge are visible in both fields. Though still noisy, the VIC system's spanwise strain can differentiate between battens and membrane. Suitable model validation is also seen in shear (Figure 20). Both peaks and distributions of the anti-symmetric shear are well predicted. The tips of the battens at the trailing edge cause a shear concentration, typically of opposite sign to the strain in the rest of the membrane segments between each batten.

Normalized out-of-plane displacements for the perimeter-reinforced wing are given in Figure 21. Deformations are slightly larger than with the BR wing (6%), and are dominated by the membrane inflation between the carbon fiber leading and trailing edges. The membrane apex occurs approximately in the middle of the membrane skin, despite the pressure gradient over the wing. This location is a function of angle of attack, as the peak will move

slightly forward with increased incidence [97], [63]. The carbon fiber wing tip twists less than previously, thought to be a result of the fact that the wingtip is not free in a PR configuration, but attached to the trailing edge by the laminate perimeter. Some bending of the leading edge at the root can also be seen, but not in the BR wing (Figure 17). Correspondence between model and experiment is suitable, with the model again under-predicting wing deformation, but accurately locating the apex. Slight asymmetries in the measured wing profile (also evident in the BR wing) are probably a result of manufacturing errors (particularly in the application of the membrane skin tension), and not due to flow problems in the wind tunnel.

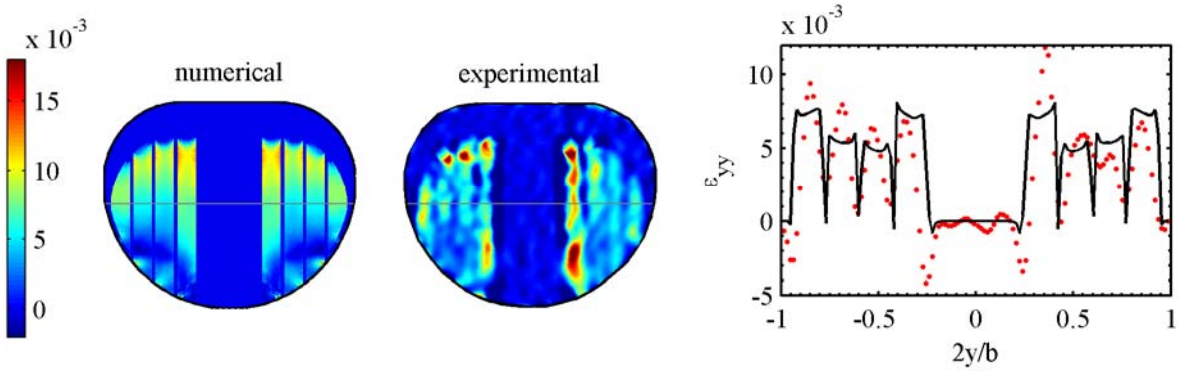

Figure 19. Baseline BR spanwise strain (ε_{yy}), $\alpha = 15^o$.

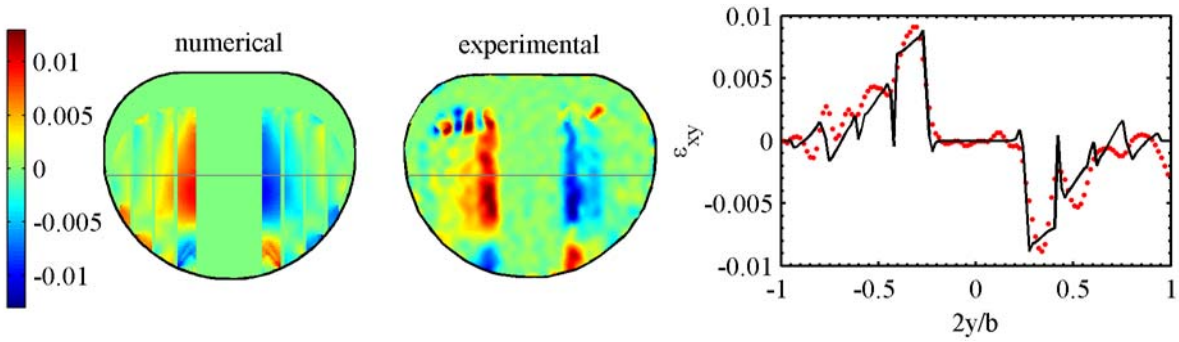

Figure 20. Baseline BR shear strain (ε_{xy}), $\alpha = 15^o$.

As the amount of unconstrained membrane is greater in a PR wing than in a BR wing, chordwise strains (Figure 22) are much larger as well: peak stretching (3%) is located at the membrane/carbon fiber boundary towards the leading edge, as before. The magnitude and size of this high-extension lobe is over-predicted by the model. Both model and experiment show a region of compressive strain aft of this lobe, towards the trailing edge. This is a Possion strain (and thus not a compressive stress), but the stress in this region does become slightly negative for higher angles of attack. Erroneous computation of compressive membrane stresses indicates the need for a wrinkling module. Though wrinkles in the membrane skin are not visible in the VIC measurements (possibly an unsteady process averaged out), wrinkling towards the onset of stall is a well-known membrane wing phenomena [130]. As before, no appreciable strain is measured or computed in the carbon fiber areas of the wing.

Peak spanwise stretching (Figure 23) occurs at the membrane carbon fiber interface towards the center of the wing root, and is well predicted by the model. The computed strain field erroneously shows a patch of negative Poisson strain towards the leading edge, due to the high chordwise strains in this area. One troubling aspect of the measured spanwise strains is the areas of negative strains along the perimeter of the membrane skin: namely on the sidewalls towards the root and the wingtip. Such strains have been measured in previous studies [21], but their presence is peculiar. Basic membrane inflation mechanics indicates large extension at the boundaries rather than compression [111] (as is computed by the model). The compression may be membrane wrinkling (which, again, is not evident from Figure 21), or may be an error in the VIC strain computations, potentially caused by the large displacement gradients in this area of the wing. A third possibility is that the VIC is measuring a bending strain at this point, where the radius of curvature is zero. The latex skin, though modeled as a membrane, does have some

(albeit very small) bending resistance due to its finite thickness. The anti-symmetric shear strain field (Figure 24) shows good correspondence between model and experiment, with accurate computations in-board, but slight under-predictions of the high shear closer to the wingtip.

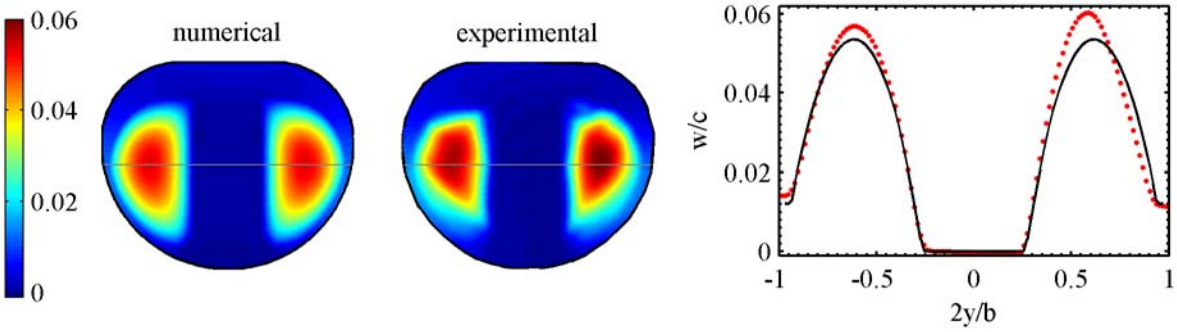

Figure 21. Baseline PR normalized out-of-plane displacement (w/c), α = 15º.

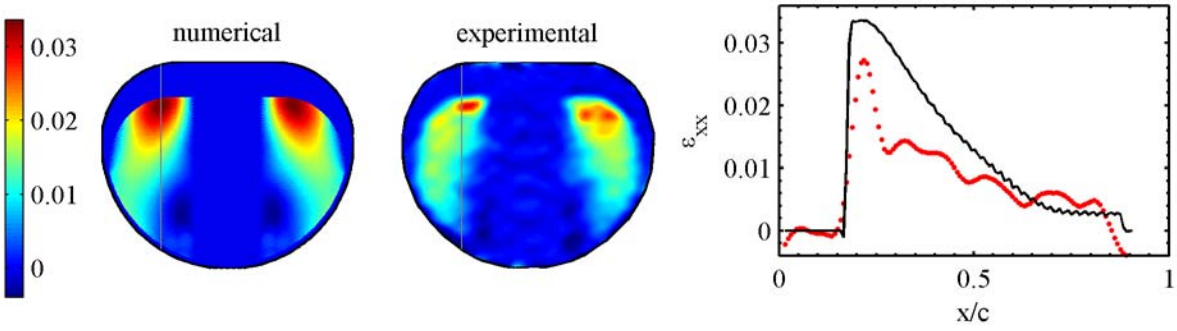

Figure 22. Baseline PR chordwise strain (ε_{xx}), α = 15º.

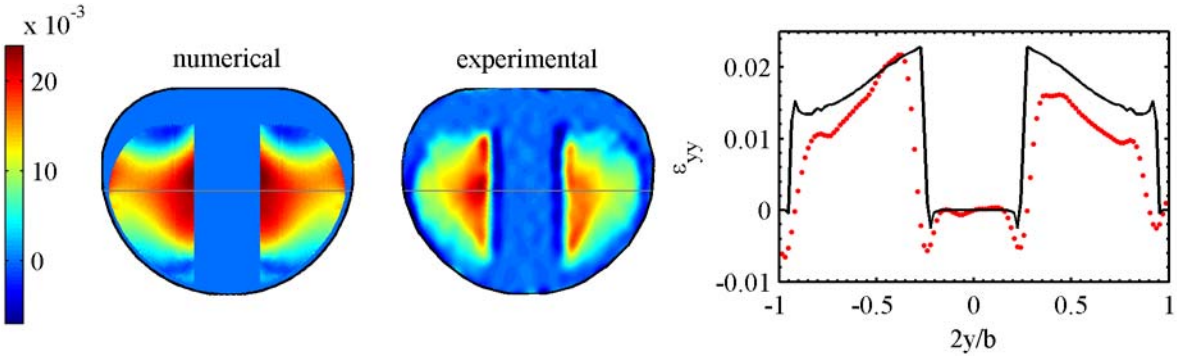

Figure 23. Baseline PR spanwise strain (ε_{yy}), α = 15º.

The aerodynamic twist (maximum camber and camber location) and geometric twist angle distributions for the baseline BR and rigid wings are given in Figure 25. The rigid wing is characterized by positive (nose-up) twist and a progressive de-cambering toward the wingtip. The carbon fiber inboard portion of the BR wing exhibits very similar wing twist to the rigid wing. Past 2y/b = 0.3 however, both model and experiment show that the membrane wing has a near-constant decrease in twist of 2-3º: adaptive washout. Though this geometric twist dominates the behavior of the BR wing, the membrane also exhibits some aerodynamic twist. This occurs predominately in the latex between the battens, about 1% of the chord in magnitude. The location of this peak camber has large variations: some portions of the wing are pushed back from 25% (rigid) to 75% (membrane), as shown by both model and experiment. Shifting the maximum camber aft-ward on low Reynolds number wings is one method to hinder separation through control of the pressure gradient [131], and may play a role in the BR wing's delayed stall.

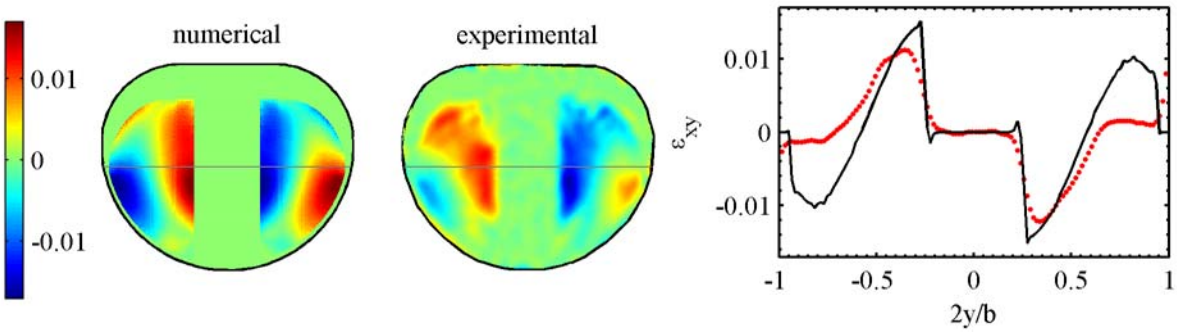

Figure 24. Baseline PR shear strain (ε_{xy}), α = 15º.

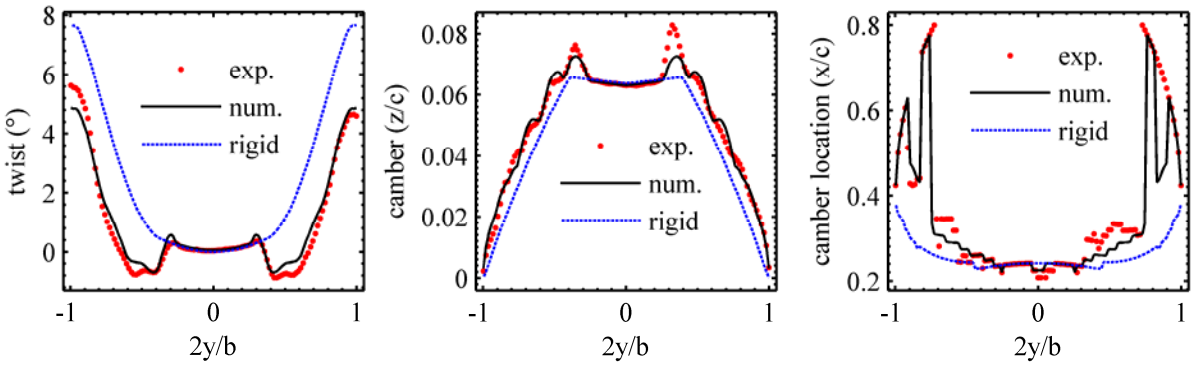

Figure 25. Baseline BR aerodynamic and geometric twist distribution, α = 15º.

The aerodynamic and geometric twist distributions for the baseline PR and rigid wings are given in Figure 26. Membrane inflation adaptively increases the maximum camber by as much as 4%, though this figure is slightly under-predicted by the model. The location of this camber is shifted aft-ward, though not as much as with the BR wing. The flexible laminate used for the wing skeleton pushes the location of the maximum root camber slightly forward. Like the BR wing deformation, shape changes over the PR wing are a mixture of both aerodynamic and geometric twist (though the former dominates). The laminated perimeter deflects upward farther than the leading edge, resulting in a nose down twist. This is as much as 2º at the wingtips, slightly under-predicted by the model.

Wing twist and maximum camber throughout the entire α-sweep are given in Figure 27, at a flexible wing section at 2y/b = 0.65. The master slave moving grid algorithm [129] fails with BR wings at angles of attack higher than 20º: the steep displacement gradients between the carbon fiber root and the membrane skin leads to excessive shearing within the CFD mesh surrounding the wing. The nose-down twist of both the BR and the PR wing increase monotonically with angle of attack, thought the former is obviously much larger. Experimentally measured BR wing twist has a linear trend (up to stall at about 22º) with α, while the numerical curve is more nonlinear, and under-predicts twist at moderate angles. Both model and experiment demonstrate a moderate increase in maximum camber of the BR wing, with a largely linear trend in α up to stall. After stall, the maximum camber of the BR wing increases substantially, from 5% to 8%.

The maximum camber of the PR wing is much larger than the rigid wing, even at low and negative angles of attack. This is due to the lack of pre-tension: even a moderate amount of force will cause substantial deformations [115]. Both measurements and simulations of the PR wing are difficult at lower angles than shown in Figure 27: the membrane is equally apt to lie on either side of the chordline [79], and steady-state solutions don't exist. PR wing camber variations with angle of attack are nonlinear (the development of finite strains cause a 1/3 power law response to the applied load [91]), and are slightly under-predicted by the model. The location of this maximum camber in a PR wing moves somewhat forward for modest angles, while the BR wing sees a significant aft-ward shift at the onset of stall. Both of these camber location trends are well-predicted by the model. Experimental error bars for camber, though not shown here, are on the order of 10% at low angles, less than 2% at moderate angles, and upwards of 20% in the stalled region [63]. This stems not from uncertainty but from unsteady membrane vibration, due to vortex shedding as discussed by Lian and Shyy [20] and Gordnier [95].

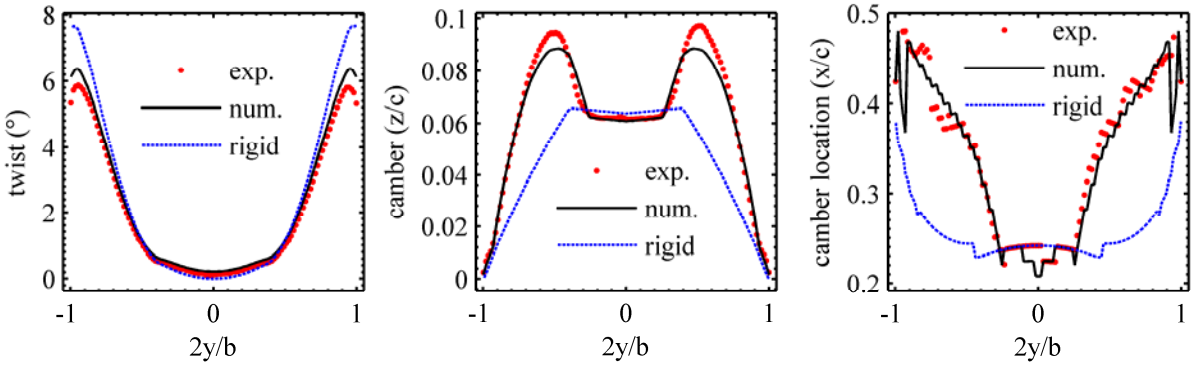

Figure 26. Baseline PR aerodynamic and geometric twist distribution, α = 15º.

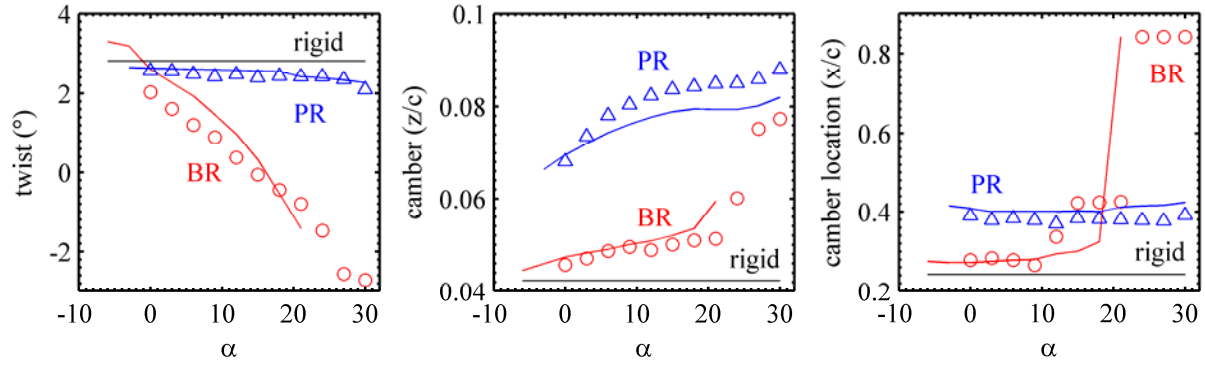

Figure 27. Aerodynamic and geometric twist at 2y/b = 0.65.

4.2. Aerodynamic Loads

Lift coefficients (both measured and predicted) throughout the α-sweep, with no model yaw, are given in Figure 28, for the three baseline wing designs discussed above. For all six data sets, lift slopes are very low (~0.05/º, about half of the value for two-dimensional airfoils [131]) as expected from low aspect ratio wings. The downward momentum from the tip vortices helps mitigate the flow separation, delaying stall to relatively high angles (18º-22º). Focusing first on the rigid wing, mild nonlinearities can be seen in the lift curve. Both model and experiment indicate an increase in the slope by 25% between 0º and 15º angle of attack. This is presumably due to a growth in the low pressure cells at the wing tips of the low aspect ratio wing [16]. Such nonlinearities should become more prevalent for lower aspect ratios than considered here (1.25). Model and experiment show good agreement for the lift over the rigid wing prior to stall. At stall (where the static model's predictive capability is questionable due to unsteady flow separation [28] and tip vortices [19]) the model slightly under-predicts the stalling angle and $C_{L,max}$; the loss of lift is more severe in the experimental data.

The adaptive inflation/cambering of the PR wing substantially increases the lift and the lift slope as compared to the rigid wing. The lift curve of the PR wing is less nonlinear than the rigid wing. This may be due to the nonlinear cambering seen in Figure 27, which is known to decrease the lift slope [33] and can offset the growth of the tip vortices. Drastic changes in the lift characteristics at low angles due to hysteresis effects [79], and a gradual onset of stall [60] are not evident in either the numerical or the experimental data, perhaps because a relevant portion of the wing is not composed of the flexible membrane. The model significantly under-predicts $C_{L,max}$ of the PR wing, and erroneously computes that the wing stalls before the rigid wing. This may be simply due to the fact that the inflated wing shape is generally under-predicted (Figure 27), or a higher-ordered coupling between the membrane vibration and vortex shedding, whose high-α lift-enhancing capabilities are seen in the work of Persson et al. [29] and Gordnier [95].

At angles of attack below 10º, the BR wing has very similar lift characteristics to the rigid wing, a fact also noted in the work of Lian et al. [30]. This is thought to be due to two offsetting characteristics of a wing with both aerodynamic and geometric twist [81]: the inflation in between each batten increases the lift, while the adaptive washout at the trailing edge decreases the lift. Both of these deformations can be seen in Figure 17. At higher

angles of attack, the load alleviation from the washout dominates the deformation, and decreases both the lift and the lift slope, as indicated by both model and experiment.

The experimental data of Figure 28 does not show the BR wing with a delayed stall over the rigid wing (and the numerical modeling cannot be taken past 20º due to aforementioned problems with the moving boundary), though it has been reported in past work [21], [26]. The stalling angle of a BR wing is a complicated function of the wing structure and Reynolds number. For low Reynolds numbers (60,000), Albertani [58] measures the stalling angles of various wings structures. Wings with very thin battens stall 3º earlier than rigid wings, but delayed stall (by 4º) is seen with thicker battens. At higher Reynolds numbers (100,000), all three wings stall at the same angle, as indicated in Figure 28 as well. Conversely, BR wing structures with a very flexible leading edge can delay stall by 2º regardless of the tested Re [58]. Further experimental testing is clearly needed for a better understanding of this phenomenon. Tailoring of the MAV wing structure is discussed in some detail below, but stalling effects are not considered due to the questionable validity of the aeroelastic model in this region, as seen in Figure 27 and Figure 28.

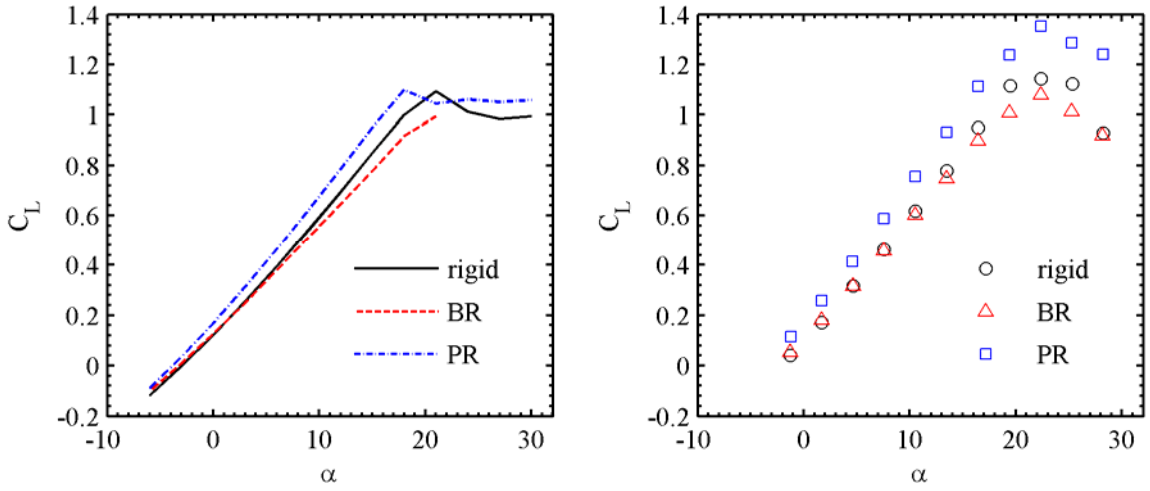

Figure 28. Baseline lift coefficients: numerical (left), and experimental (right).

Figure 29 shows drag coefficients through the α-sweep, with good experimental validation of the model. Drag is slightly over-predicted at higher angles of attack, presumably due to the fully-laminar CFD used in the study [28]. Transitioned flow can entrain high-momentum flow from the free layer and cause quicker reattachment for decreased drag [12]. As before, the drag of the rigid and the BR wings are very similar for modest angles of attack. Above 10º the load alleviation at the trailing edge decreases the drag (compared to the rigid case), a streamlining effect [101]. It should be noted however that for a given value of lift, the BR wing actually has slightly more drag than a rigid wing [21]. Regardless of whether the comparative basis is lift or angle of attack, the PR wing has a drag penalty over the rigid wing. This is in part due to the highly non-optimal airfoil shape of each membrane wing section: Figure 21 shows the tangent discontinuity of the wing shape at the membrane/carbon fiber interface towards the leading edge. Excessive inflation may also induce additional flow separation.

Longitudinal pitching moments (measured about the leading edge) are given as a function of lift for the three baseline designs in Figure 30. Of the three, the PR wing is not statically stable (based upon a negative $C_{m,AC}$), and the hinged trailing edge portion (seen in Figure 1 and Figure 2) must be used for trimmed flight. Prior to stall, both the aeroelastic model and the experiment indicate very similar behavior between the rigid and the BR wing, with mild nonlinearities in the moment curves. This is ostensibly due to tip vortex growth, as before [16]. The PR wing has a 15% lower pitching moment slope than the rigid wing. This is a result of the membrane inflation, which shifts the pressure recovery towards the trailing edge, adaptively increasing the strength of the nose-down (restoring) pitching moment with increases in lift and α. Steeper C_m slopes indicate larger static margins: stability concerns are a primary target of design improvement from one generation of micro air vehicles to the next. The static margin of a MAV is generally only a few millimeters long; properly fitting all the micro-components on board can be difficult. Furthermore, the PR wing displays a greater range of linear Cm behavior, possibly due to the fact that the adaptive membrane inflation quells the strength of the low pressure cells [26].

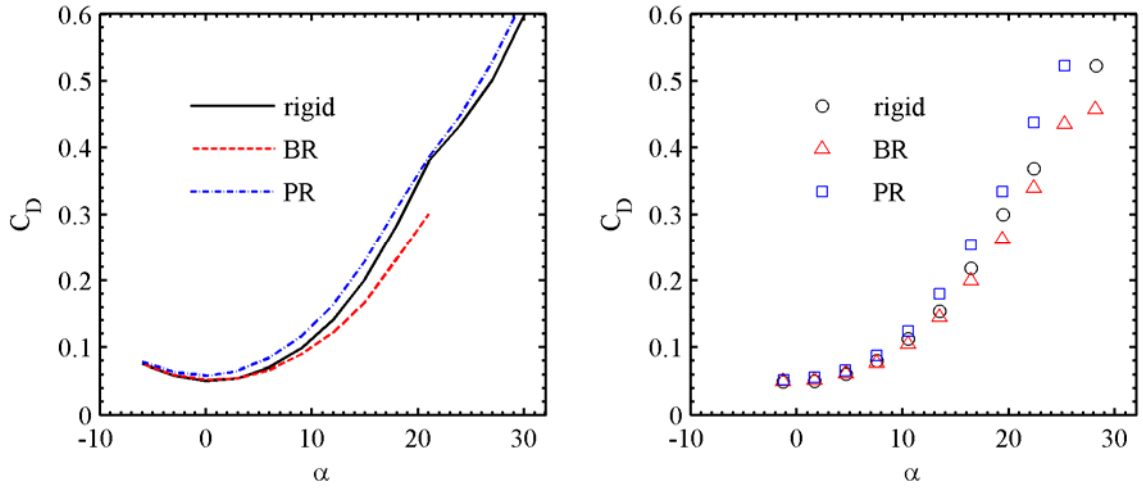

Figure 29. Baseline drag coefficients: numerical (left), and experimental (right).

Finally, L/D characteristics are given in Figure 31, as a function of lift. For low angles of attack (and lift), the three wings perform similarly. At higher angles of attack (prior to stall), the PR wing has the highest efficiency. The model incorrectly computes the BR wing to have the best L/D for a small range of modest lift values. Correlation between model and experiment is generally acceptable for the rigid and BR wings, though the L/D of the PR wing is significantly under-predicted by the model, owing mostly to poor lift prediction at these angles (Figure 28). At no point does either model or experiment indicate that the rigid wing has the best efficiency; perhaps surprising, given the fact that neither wing deforms into a particularly optimal airfoil shape.

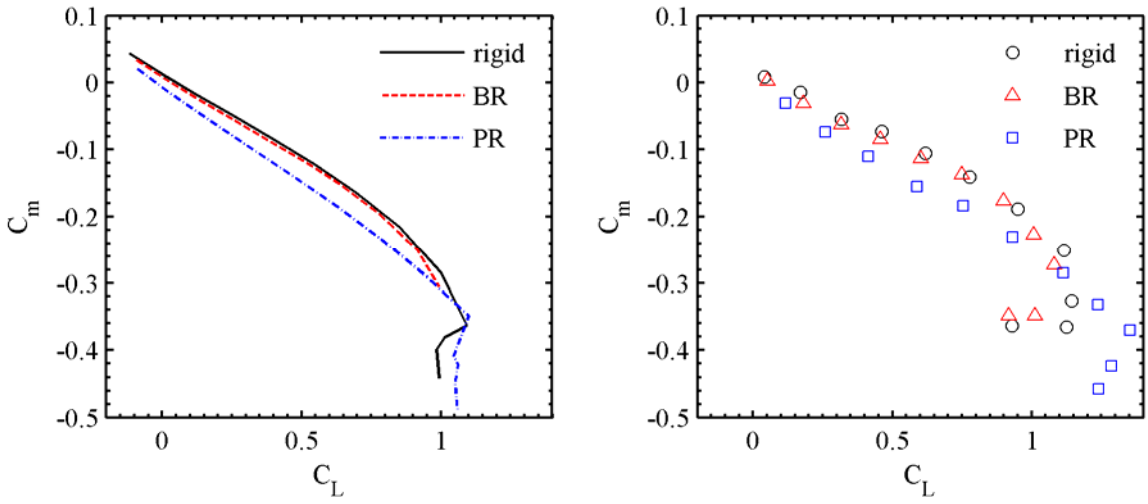

Figure 30. Baseline pitching moment coefficients: numerical (left), and experimental (right).

A quantitative summary of the last four figures is given in Table 4, for all three baseline wings at 6º angle of attack. Experimental error bounds are computed as described in section 2.2.1. Aerodynamic sensitivities (as well as the pitching moment about the aerodynamic center) are found with a linear fit through the pre-stall angles of attack. Error bounds in these slopes are computed with Monte Carlo simulations. Computed lift, drag, and pitching moments consistently fall within the measured error bars (the latter of which are exceptionally large), though pitching moments are significantly under-predicted (10-30%). Sensitivities are also under-predicted, though still fall within the large error bars associated with pitching moment slopes. With the exception of L/D of a PR wing, trends between different wing structures are well-predicted by the aeroelastic model.

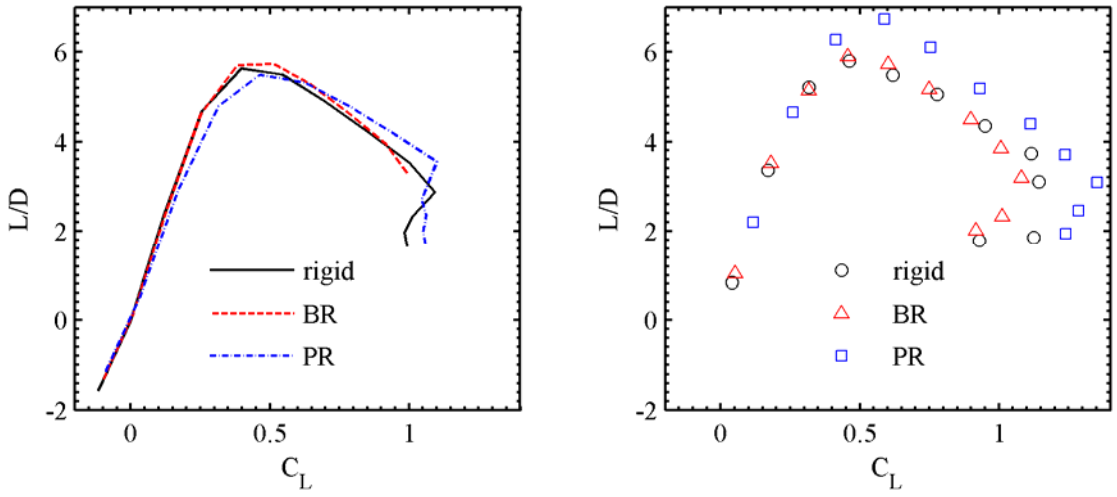

Figure 31. Baseline wing efficiency: numerical (left), and experimental (right).

Table 4. Measured and computed aerodynamic characteristics, α = 6°.

	C_L			C_D		
	num.	exp.	error (%)	num.	exp.	error (%)
rigid	0.396	0.384 ± 0.024	3.10	0.070	0.069 ± 0.007	1.15
BR	0.381	0.382 ± 0.024	-0.16	0.067	0.069 ± 0.007	-3.04
PR	0.465	0.495 ± 0.031	-5.98	0.085	0.076 ± 0.009	11.61
	C_m			L/D		
	num.	exp.	error (%)	num.	exp.	error (%)
rigid	-0.084	-0.063 ± 0.033	-32.81	5.64	5.49 ± 0.69	2.72
BR	-0.087	-0.073 ± 0.034	-19.39	5.70	5.49 ± 0.68	3.77
PR	-0.138	-0.131 ± 0.042	-5.64	5.49	6.49 ± 0.87	-15.36
	$C_{L\alpha}$			$C_{m,AC}$		
	num.	exp.	error (%)	num.	exp.	error (%)
rigid	0.049	0.051 ± 0.003	-5.26	0.013	0.016 ± 0.018	-
BR	0.044	0.048 ± 0.004	-9.35	0.006	-0.001 ± 0.020	-
PR	0.052	0.057 ± 0.004	-9.21	-0.008	-0.015 ± 0.026	-
	$C_{m\alpha}$			dC_m/dC_L		
	num.	exp.	error (%)	num.	exp.	error (%)
rigid	-0.012	-0.010 ± 0.004	-11.65	-0.246	-0.199 ± 0.086	-23.07
BR	-0.011	-0.009 ± 0.004	-17.97	-0.244	-0.185 ± 0.098	-31.88
PR	-0.014	-0.013 ± 0.006	6.01	-0.280	-0.229 ± 0.105	-22.17

4.3. Flow Structures

Having established sufficient confidence in the static aeroelastic membrane wing model, attention is now turned to the computed flow structures. No experimental validation is available for this work, though whenever possible the results will be correlated to flow visualization work reviewed in section 2.4.

The pressure distributions and flow structures are given in Figure 32 at 0° angle of attack for the upper/suction wing surface of all three baseline wing designs. The plotted streamlines reside close to the surface, typically within the boundary layer. For the rigid wing, a high pressure region is located close to the leading edge, corresponding to flow stagnation. This is followed by pressure recovery (minimum pressure), located approximately at the maximum camber of each rigid wing section. Pressure recovery is followed by a mild adverse pressure gradient, which is not strong enough to cause the flow to separate. A further decrease in Reynolds number has been shown to cause mild

flow separation over the top surface for 0° however [27], [42]. A small locus of downward forces are present over the negatively-cambered region (reflex) of the airfoil, helping to offset the nose-down pitching moment of the remainder of the rigid MAV wing. The reflex can also help improve the wing efficiency, compared to positively-cambered wings. There is positive lift of this wing at 0° (Figure 28), resulting in a mild tip vortex swirling system. The low pressure cells at the wing tip are not yet evident.

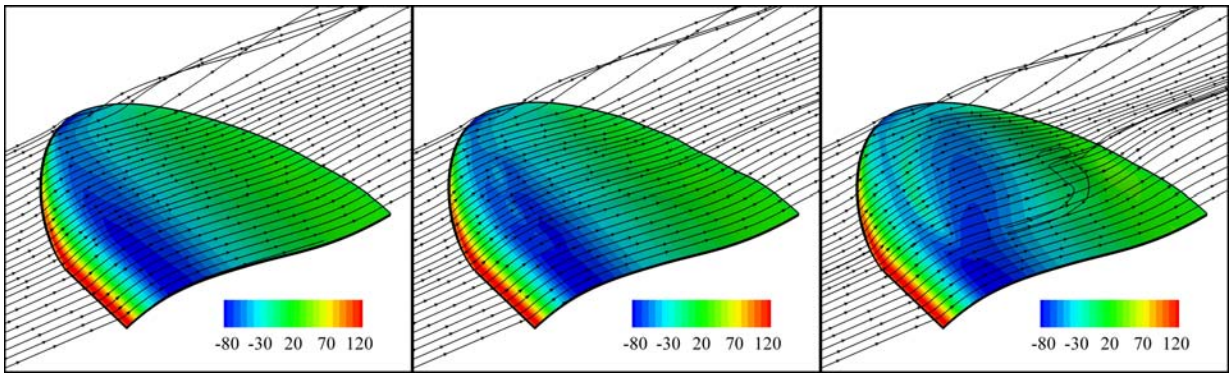

Figure 32. Pressure distributions (Pa) and streamlines on the upper surface of a rigid (left), BR (center), and PR wing (right), α = 0º.

Aeroelastic pressure redistributions of the upper surface of the BR wing are seen in the form of three high-pressure lobes at the carbon fiber/membrane boundary interface towards the leading edge. The membrane inflation in between each batten (Figure 17) results in a slight tangent discontinuity in the wing surface. This forces the flow to slow down and redirect itself over the inflated shape: such a deceleration results in a pressure spike. Aft of these spikes, the pressure is slightly lower in the membrane skin than over each batten (due to the adaptive camber), driving the flow into the membrane patches. This is a very small effect (mildly visible in the streamlines) for the current case, but can be expected to play a large role with potential flow separation, where the chordwise velocities are very small [132].

For the PR wing (Figure 32), the pressure spike is stronger, and exists continuously along the membrane interface. A significant percentage of this spike is directed axially, increasing the drag (as seen in Figure 29). The adaptive inflation causes an aft-ward shift in the pressure recovery location of each flexible wing section. The longer moment arm increases the nose-down pitching moment about the leading edge (Figure 30), which is the working mechanism behind the benevolent longitudinal static stability properties of the PR wing. Furthermore, the aerodynamic twist increases the adverse pressure gradient over the membrane portion of the wing: some flow now separates as it travels down the inflated shape, further increasing the drag (as compared to the rigid wing).

Similar results are given for the lower/pressure side of the three wings at 0º angle of attack in Figure 33. The flow beneath the rigid wing is dominated by an adverse pressure gradient towards the leading edge, causing a large separation bubble underneath the wing camber. This separated flow is largely confined to the in-board portions of the wing. Flow reattaches slightly aft of the quarter-chord, after which the pressure gradient is favorable. The flow accelerates beneath the negatively-cambered portion of the rigid wing: this decreases the local pressures, further offsetting the nose-down pitching moment. The pressure distribution on the lower surface is not greatly affected by the tip vortices, previously noted by Lian et al. [30]. For the BR wing, slight undulations in the pressure distribution are indicative of the membrane inflation in between the battens. This causes the opposite of what is seen on the upper wing: flow is slightly packed towards the battens [132], though the effect is minor, as before. The adaptive aerodynamic twist of the PR membrane wing pushes the bulk of the separated flow at the leading edge towards the root, and induces further separation beneath the inflated membrane shape, as the air flows into the cavity against an adverse pressure gradient. The location of maximum pressure is increased and pushed aft-ward to coincide with the apex of the inflated membrane, increasing both the lift and the stability.

Flow structures over the upper surface at 15º angle of attack are given in Figure 34. At this higher incidence, the adverse pressure gradient is too strong for the low Reynolds number flow to overcome, and a large separation bubble is present at the three-quarter chord mark of the rigid wing. Despite the nose-up geometric twist built into the wing (7º at the tip, Figure 25), flow separates at the root first, and is largely confined (at this angle) to the in-board portion of the wing. The reattached flow aft of the bubble (and the resulting pressure distribution) must be viewed with a certain amount of suspicion. Such a reattachment is known to be turbulent process [117], and no such

module is included in the CFD. The reflex airfoil will create a favorable pressure gradient towards the trailing edge however, which may induce the attachment: similar behavior is seen experimentally by Tamai et al. [41]. Unsteady vortex shedding will accompany the bubble as well, though numerical time-averaging of vortex shedding is known to compare well with steady experimental measurements of a single stationary bubble [28]. The augmented incidence has considerably increased the strength of the wing-tip vortex swirling system over the rigid wing. The size of the vortex core is larger, and the low pressure cells at the wing tip are very evident [16].

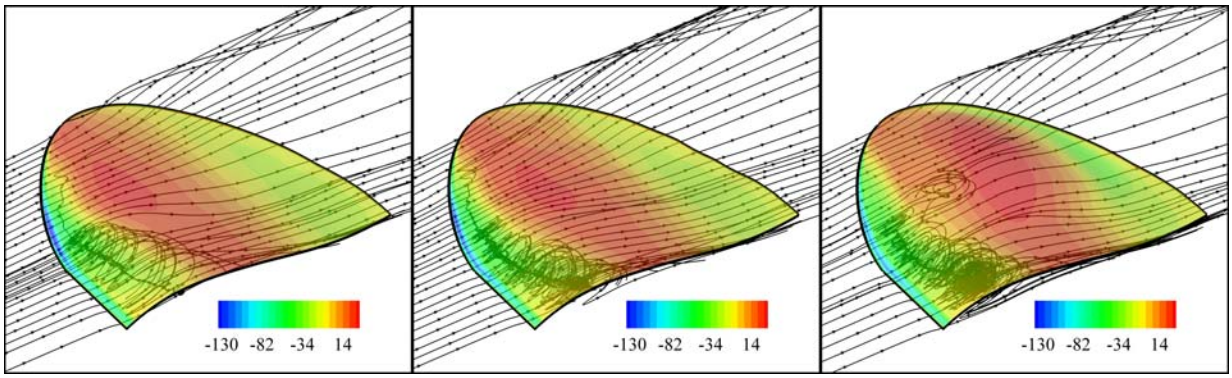

Figure 33. Pressure distributions (Pa) and streamlines on the lower surface of a rigid (left), BR (center), and PR wing (right), α = 0º.

As expected, the aeroelastic effects of the BR and PR wings are more predominate at 15º in Figure 34. For the BR wing, the three high-pressure lobes over the membrane/carbon fiber interface are larger. Significant pressure-redistribution over the membrane stretched between the outer batten and the wing tip can be seen as well. Adaptive washout slightly decreases the intensity of the separation bubble, but has no noticeable effect on the pressure distribution at the trailing edge of the upper BR wing surface. At 15º, the aerodynamic twist of the PR wing is considerably larger than before, as is the resulting pressure spike at the membrane-carbon fiber interface. Despite the large adverse pressure gradient in this region, flow does not separate. The inflated membrane shape of the PR wing pushes the bulk of the flow separation closer to the wing root. Some of this separated flow reattaches to the wing and travels into the wake, while the rest travels spanwise. This flow is attracted either by the low pressures associated with the adaptive cambering, or by the low pressures at the core of the tip vortex. Some of these separated streamlines are entrained into the swirling system, an interaction that has been shown to cause potential bilateral instabilities for high angles of attack [19].

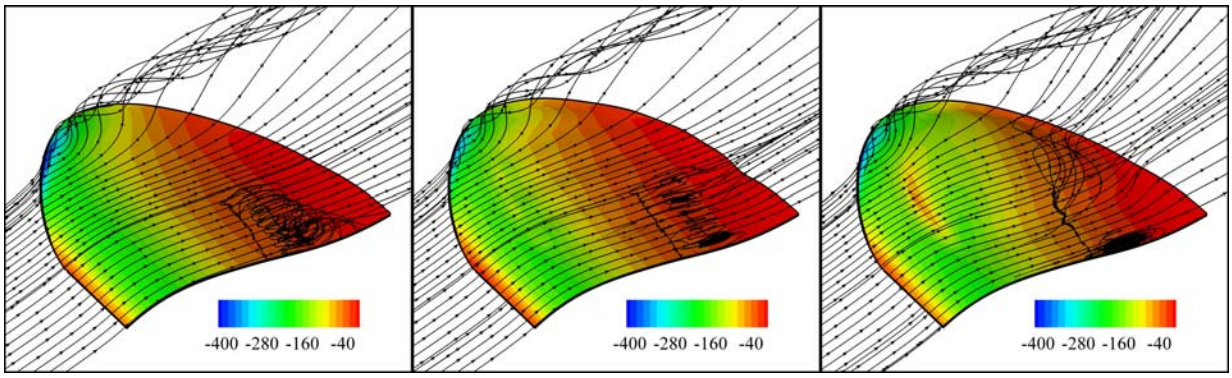

Figure 34. Pressure distributions (Pa) and streamlines on the upper surface of a rigid (left), BR (center), and PR wing (right), α = 15º.

It can also be seen that the passive shape adaptation decreases the magnitude of the low pressure cells at the wing-tip, by 9% for the BR wing and 13% for the PR wing, compared to the rigid case. The inflated membrane shape may act as a barrier to the tip vortex formation, preventing the full swirling development at the wing-tip. A similar effect is demonstrated in the work of Viieru et al. [118] through the use of endplates installed on the wingtips

of a rigid micro air vehicle wing. Whereas the endplates are able to decrease induced drag only at moderate angles (afterwards the tip vortices increase in strength to overwhelm the geometrical presence of the endplates), the phenomena demonstrated in Figure 34 is effective at all angles: both the size of the membrane barrier and the strength of the vortex swirling grow in conjunction with one another as the angle of attack increases. This decrease in tip vortex strength is also evidenced in Figure 30: the nonlinear aerodynamics (due to the low pressure cells at the tip) is evident in the pitching moments of the rigid and BR wings, while the PR curve is very linear.

On the underside of the rigid wing at 15º angle of attack (Figure 35), the increased incidence provides for completely attached flow behavior. The pressure gradient is largely favorable, smoothly accelerating the flow from leading to trailing edge. From the previous four figures it can be seen that separated flow over the bottom surface gradually attaches for increasing angles of attack, while attached flow over the upper surface gradually separates (eventually leading to wing stall). As time-averaged flow separation is likely to be unsteady vortex shedding [28]: this explains the aforementioned membrane vibration amplitudes that decrease to a quasi-static behavior, then increase through the α-sweep [71].

Load alleviation on the lower surface of the BR wing is evidenced by a decrease in the high-pressure regions associated with camber, and a growth of the suction region at the trailing edge (the latter presumably due to a decrease in the local incidence). The adaptive inflation of the PR wing causes a significant redirection of the flow vectors beneath the wing, but does not induce flow separation. Two sharp pressure drops are seen beneath the wing: one as the flow accelerates into the inflated membrane shape, and the second as the flow accelerates out of from the membrane and underneath the re-curved area of the wing. The tangent discontinuities are seen as geometry cusps beneath the wing, and the flow must travel very quickly over the small radius of curvature.

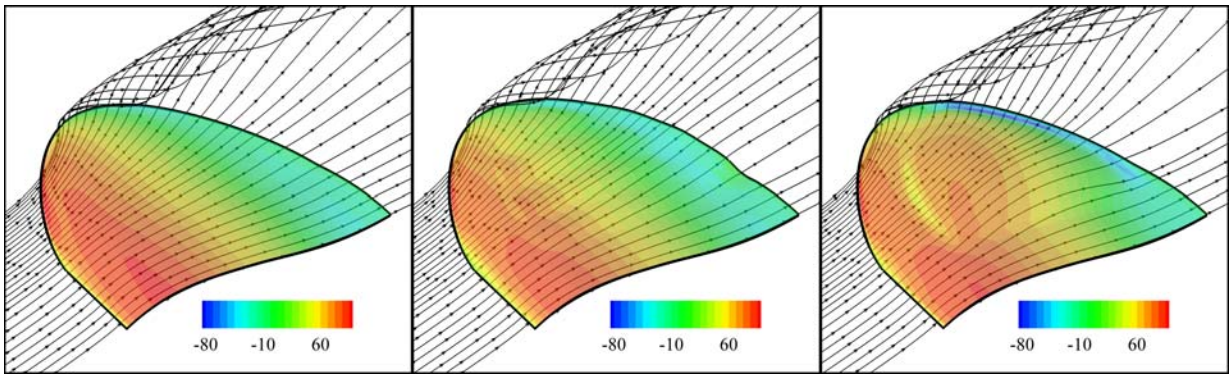

Figure 35. Pressure distributions (Pa) and streamlines on the lower surface of a rigid (left), BR (center), and PR wing (right), α = 15º.

5. Tailoring Studies

Although aeroelastic tailoring is generally defined as the addition of directional stiffness into a wing structure so as to beneficially affect performance [22], this has traditionally meant the use of unbalanced composite plates/shells. Despite the use of such laminated materials on many MAV wing frames [133], there does not appear to be any tailoring studies on fixed micro air vehicle wings. Conventional tailoring studies can be found applied to a larger class of unmanned aerial vehicles [134], [135]. The latter study by Weisshaar et al. uses laminate tailoring to improve the lateral control of a vehicle with an aspect ratio of 3. With ailerons, a wing tailored with adaptive wash-in is shown to improve roll performance and roll-reversal speed, though wash-out is preferred for a leading-edge slat [135]. Generalized tailoring studies have been used to design flapping ornithopter wings [136], [137] as well, though specific laminate-based design has not.

In addition to conventional laminate-based tailoring, drastic changes in the performance of a membrane wing are attainable by altering the pre-tension distribution within the extensible membrane. Holla et al. [86], Fink [130], Smith and Shyy [91], Murai and Maruyama [87], Ormiston [33], and Gordnier [95] all note the enormous impact that membrane pre-tension has on aerodynamics: for the two-dimensional case, higher pre-tension generally pushes flexible wing performance to that of a rigid wing. For a three-dimensional wing, the response can be considerably more complex, depending on the nature of the membrane reinforcement. Well-reported effects of increasing the membrane pre-tension include: decrease in drag [60], decrease in $C_{L\alpha}$ [33], linearized lift behavior [91], increase in the zero-lift angle of attack [87], and more abrupt stalling patterns [60]. Gordnier notes that increasing pre-tension

decreases the time-averaged lift, alters the membrane dynamics from a third mode standing wave to a second mode, and drops the St from 1.43 to 1.13 [95].

Application of pre-tension is also a well known method used to prevent numerous undesirable aeroelastic behaviors of a membrane wing. The lift slope of excessively flexible membrane wings may approach infinity, leading to obvious flight stability and control issues. Ormiston details this stability boundary as a function of the ratio of spanwise to chordwise pre-tension, as well as the tension in a trailing edge cable [33]. The free trailing edge of membrane wing (such as the BR wing) may be prone to large-amplitude flapping vibrations, which can degrade the lift, drag, and efficiency [35]. Tension is an obvious remedy to this issue [36]; it is hypothesized that tension induced into the membrane skin from skin friction can substantially over-predict this stability boundary computed with inviscid methods [77]. Topological reinforcement through batten structures is another solution to this problem.

Adequate control of membrane tension has long been known as a crucial concern to sailors in order to efficiently exploit wind power [138]. Tension-control is similarly important to the performance and agility of fighter kites: a wrinkled membrane surface can send the kite into an unstable spin. When pointed in the desired direction, pulling the control line tenses and deforms the kite, which thus attains forward velocity [139]. Biological inspiration for aerodynamic tailoring of membrane tension can be seen in the wing structures of pterosaurs and bats. In addition to significant membrane anisotropy (pterosaur wings have internal fibrous reinforcement to limit chordwise stretching [140], while bat wings skins are measured to be 100 times stiffer in the chordwise direction than the spanwise [141]), the tension can be controlled through a single digit (pterosaurs) [36], or varied throughout the wing via multiple digits (bats) [142].

Work formally implementing membrane tension as a variable for optimizing aerodynamic performance is very rare. Levin and Shyy [94] study a modified Clark-Y airfoil with a flexible membrane upper surface, subjected to a varying freestream velocity. Response surface techniques are used to maximize the power index averaged over a sinusoidal gust cycle, with membrane thickness variation, elastic modulus, and pre-stress used as variables. The maximum power index is found to coincide with the lower bound placed upon pre-stress, though lift and efficiency are also seen to be superior to a rigid wing.

It should also be noted that aeroelastic tailoring of the structure is one of many methods that must be taken into consideration for the design of an efficient, agile, and stable membrane micro air vehicle wing through a wide range of mission requirements. Torres [16], for example, minimizes a weighted combination of payload, endurance, and agility metrics, with various discrete (wing and tail planform) and continuous (aspect ratio, propeller location, angle of attack, etc) variables. Aerodynamic analysis is provided by a combination of experimental data, analytical methods, and interpolation techniques. Stanford et al. [143] optimize the actuator distribution throughout a membrane wing, where un-symmetric wing twist is used for lateral agility. The laminate reinforcement of a membrane MAV wing is well-suited for aeroelastic topology optimization studies as well, an idea pioneered in the work of Maute et al. [144], and used explicitly for MAVs by Stanford [145] with a two-material formulation (latex membrane or carbon fiber laminate) on the wetted surface.

Results presented here are concerned with the effect of structural sizing/strength variables within the aeroelastic system. Wing shape, angle of attack, and free-stream velocities are fixed, and wing topologies are restricted to the BR, PR, and rigid. Results from the previous section show that the membrane skin's inflation/stretching dominates the aeroelastic behavior, indicating the importance of the pre-tension in the membrane skin. Pre-stress resultants in the spanwise and chordwise directions are both considered as variables. With the exception of the free trailing edge correction of the BR wings detailed above, the pre-tension is constant throughout the wing. The laminate orientation and number of plies used to construct the plain weave carbon fiber areas of the wing can be varied as well. Finally, the number of layers in each batten of the BR wing can be altered, though the orientation will be fixed so that the fibers run parallel to the chord line. The static aeroelastic modeling algorithm detailed above can elucidate accurate quantitative dependencies of a variety of parameters (C_L, C_D, C_m, L/D, $C_{L\alpha}$, $C_{m\alpha}$, mass) upon these parameters.

The sizing/strength parameters listed above leads to an optimization framework with 9 variables, if the number of layers in each of the three battens is permitted to differ, and the wing type (BR, PR, rigid) is considered a variable as well. For this work, one-factor-at-a-time (OFAT) numerical tests are run to establish the effect of various structural parameters upon the relevant aerodynamics. The three baseline wing designs used above will represent the nominal wing designs (2 layers of plain weave at 45º, one layer battens, slack membrane). Having identified the structural variables that display the greatest sensitivity within the system, a full-factorial designed experiment [146] will be run on a reduced set of variables. This data set can then be used to identify the optimal wing type and structural composition for a given objective function. Designs that strike a compromise between two objective functions are considered as well. The work concludes with experimental wind tunnel validation of the performance of selected optimal designs.

5.1. OFAT Simulations

The schedule of OFAT simulations is as follows: a 6-level full factorial design is conducted for the chordwise and spanwise pre-stress resultants, 6 simulations for the orientation of a single laminate of plain-weave, a 6-level full factorial design for the orientations of a two-layer laminate plain weave, and a 3-level full factorial design for the number of layers used in the three battens. Pre-stress is bounded by 0 N/m (slack membrane) and 25 N/m (values larger than this may subject the wing skeleton to axial buckling). The latter value corresponds to roughly 10% pre-strain. Plies of plain weave carbon fiber are limited to two layers, while battens are limited to three.

5.1.1. Membrane Pre-Tension

Computed aerodynamic derivatives ($C_{L\alpha}$ and $C_{m\alpha}$) and efficiency (L/D) are given as a function of the pre-stress resultants in the chordwise (N_x) and spanwise (N_y) directions for a BR wing in Figure 36. The corresponding normalized wing displacement is given in Figure 37 for a subset of the data matrix. All results are computed at 12º angle of attack, aerodynamic derivatives are computed with a finite difference between 11º and 12º. In a global sense, increasing the pre-tension in the BR wing increases $C_{L\alpha}$, decreases $C_{m\alpha}$, and decreases L/D. The increased membrane stiffness prevents effective adaptive washout (and the concomitant load alleviation), and the wing performance tends towards that of a rigid wing. At 12º for a rigid wing, $C_{L\alpha}$ = 0.0507, $C_{m\alpha}$ = -.0143, and L/D = 4.908. Overall sensitivity of the aerodynamics to the membrane pre-tension can be large for the derivatives (up to 20%), though less so for the wing efficiency (less than 5%, presumably due to the conflictive nature of the ratio).

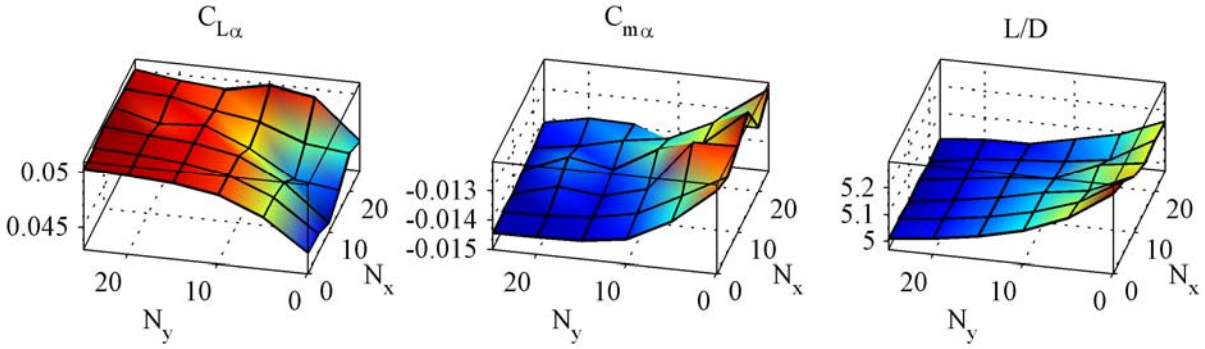

Figure 36. Computed tailoring of pre-stress resultants (N/m) in a BR wing, α = 12º: color contour represents z-axis values.

The BR wing is very sensitive to the pre-stress in the spanwise direction, but less so to stiffness in the chordwise direction. This is evinced in Figure 37: the slack membrane wing has a trailing edge deflection of 2.5% of the root chord. Maximizing the spanwise pre-tension (but leaving the other direction slack) drops this value to 1%, while the opposite scenario drops the value to only 1.9%. This is due to the directional stiffness of the battens (which depend on compliance normal to their axis for movement), but also the free trailing edge stress correction detailed above. Despite the global trend towards a rigid wing with increased pre-tension, the changes are not monotonic. A wing design with a minimum lift slope (for gust rejection, improved stall performance, etc.) is found, not with a completely slack wing, but a wing with a mild amount of stiffness (10 N/m) in the chord direction, and none in the span direction. Such a tactic removes the aforementioned conflicting sources of aeroelastic lift in a BR wing. The pre-stress correction eliminates most of the stiffness at the trailing edge (allowing for adaptive washout and load alleviation), but retains the chordwise stiffness towards the leading edge, as seen in Figure 13. The membrane inflation in this area is thus decreased, along with the corresponding increase in lift due to camber.

Maximizing $C_{L\alpha}$ (for efficient pull-up maneuvers, for example), is found by maximizing N_y and setting N_x to zero; this eliminates the adaptive washout, but retains the inflation towards the leading edge. Conversely, maximizing $C_{L\alpha}$ with a constraint on the acceptable L/D might be obtained by maximizing N_x and setting N_y to zero. Peak efficiency is found with a slack membrane: this corresponds to minimum drag, which is not shown. It should be mentioned however, that if a design goal is to maximize the lift slope (or minimize the pitching moment slope for stability), a BR wing is most likely a poor choice.

Opposite trends are found for the PR wing (Figure 38 and Figure 39): increasing the pre-tension decreases $C_{L\alpha}$, increases $C_{m\alpha}$, and increases L/D. Similar to before, added wing stiffness decreases the adaptive inflation of the wing skin, and results tend towards that of a rigid wing. Without the directional influence of the battens and the

trailing edge stress correction needed for the BR wing, the PR wing surfaces in Figure 38 are very smooth, and converge monotonically for high pre-stress.

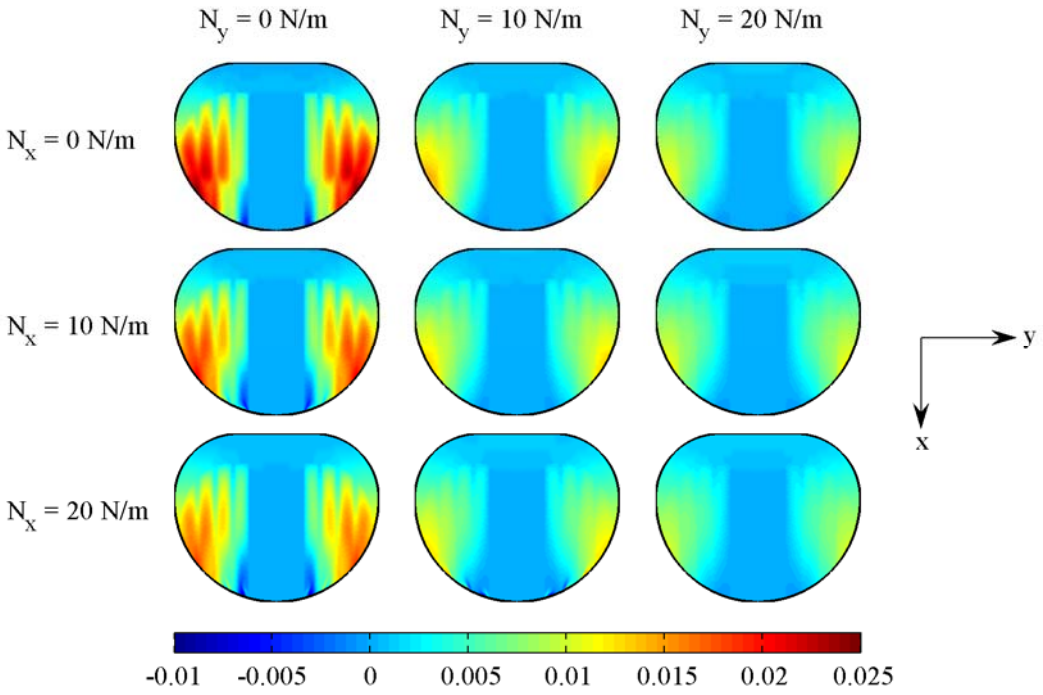

Figure 37. Computed BR wing deformation (w/c) with various pre-tensions, α = 12º.

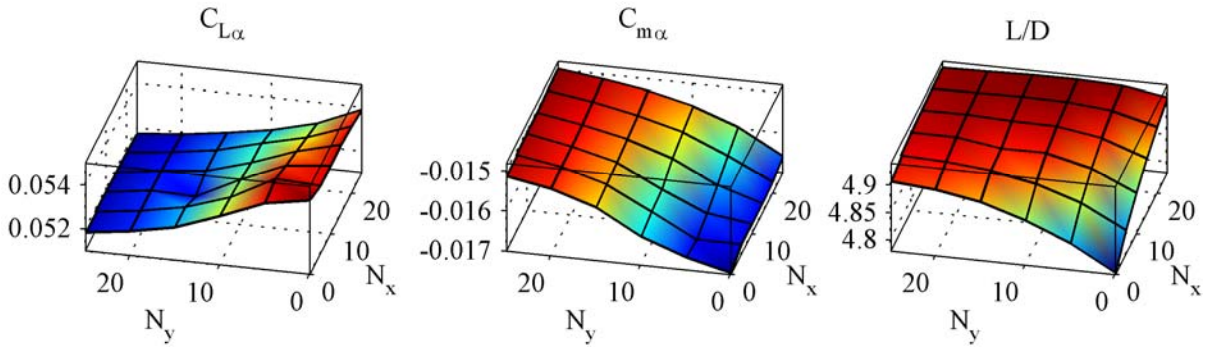

Figure 38. Computed tailoring of pre-stress resultants (N/m) in a PR wing, α = 12º: color contour represents z-axis values.

As before, the PR wing is more sensitive to pre-tension in the spanwise direction than the chordwise direction. The slack membrane wing inflates to 5% of the chord: maximizing tension in the chord direction (with none in the span direction) drops this value to 3%, though the opposite case drops the value to 1.5%. This is probably due to the fact that the chord of the membrane skin is about twice as long as it's span. The sensitivity of a pressurized rectangular membrane to a directional pre-stress is inversely-proportional to its length in the same direction, as indicated by solutions to Eq. (4). Though the L/D of the PR wing is equally affected by pre-stresses in both directions, the two aerodynamic derivatives in Figure 38 have a significantly muted response to N_x. Such a result has noteworthy ramifications upon a multi-objective optimization scenario. The longitudinal static stability is optimal for a slack membrane wing, but the wing efficiency at this data point is poor. Maximizing N_x and setting N_y to zero greatly improves the lift-to-drag ratio (only 0.2% less than the true optimum found on this surface), with a negligible loss in static stability.

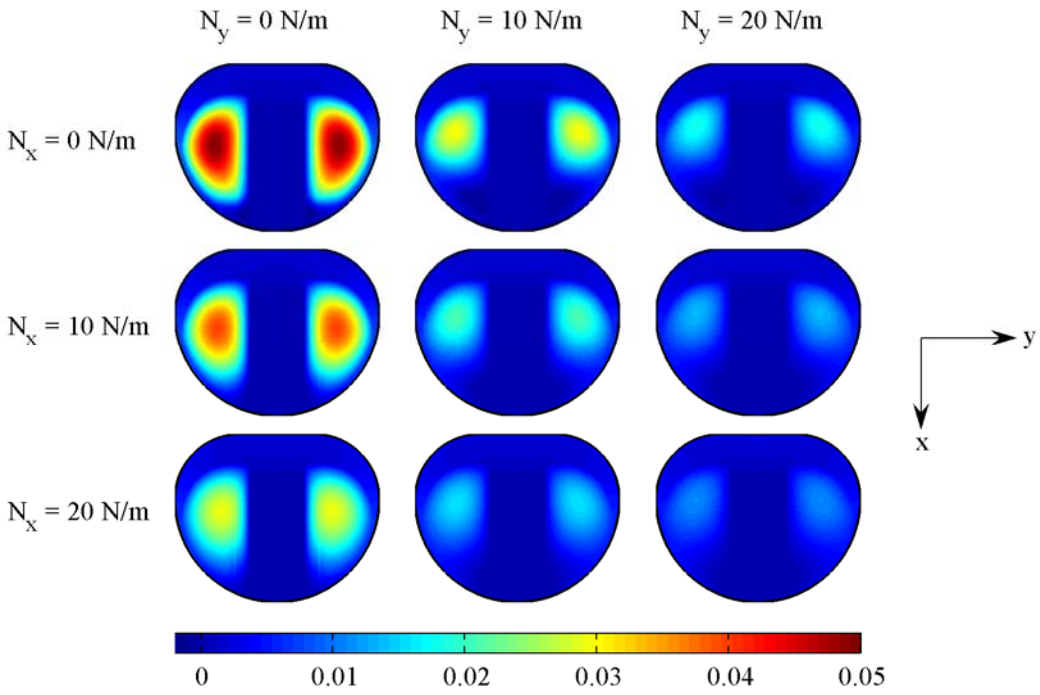

Figure 39. Computed PR wing deformation (w/c) with various pre-tensions, α = 12º.

5.1.2. Single Ply Laminates

The same aerodynamic metrics are given in Figure 40 as a function of the ply angle (with respect to the chord line) for a set of wings with a single layer of bi-directional carbon fiber at the wing root, leading edge, and perimeter (for the PR wing only). The membrane wing is slack. Due to the plain weave nature of the laminate, all trends are periodic every 90º. Only fiber orientations of 0º, 45º, and 90º automatically satisfy the balance constraint [147]. For the PR wing, changing the fiber angle has a minor effect on the aeroelastic response, and optima are mostly located at either 45º (where spanwise bending is largest) or 90º (where it is smallest). This indicates that the PR wing, whose planform is dominated by membrane skin, can only take advantage of different laminates inasmuch as the spanwise bending can increase or decrease the aerodynamic membrane twist/cambering.

On the other hand, the BR wing relies mostly upon geometric twist (Figure 27), which can be provided from unbalanced laminates via bend-twist coupling; the concept behind traditional aeroelastic tailoring [22]. Of the 7 data points shown in Figure 40, orientations less than 45° cause the wing to wash-in, while angles greater than 45° cause washout, the latter of which minimizes $C_{L\alpha}$ of a BR wing, as expected. Using laminate wash-in to counter the load alleviation of the membrane washout (at 15°) optimizes the wing efficiency. Aerodynamic sensitivity of the BR wing to laminate orientation is also larger than that seen in the PR wing because the carbon fiber skeleton is less constrained. The wing tip of the BR wing (where the forces can be large, due to the tip vortices seen in Figure 34) is not connected to the trailing edge via a perimeter strip.

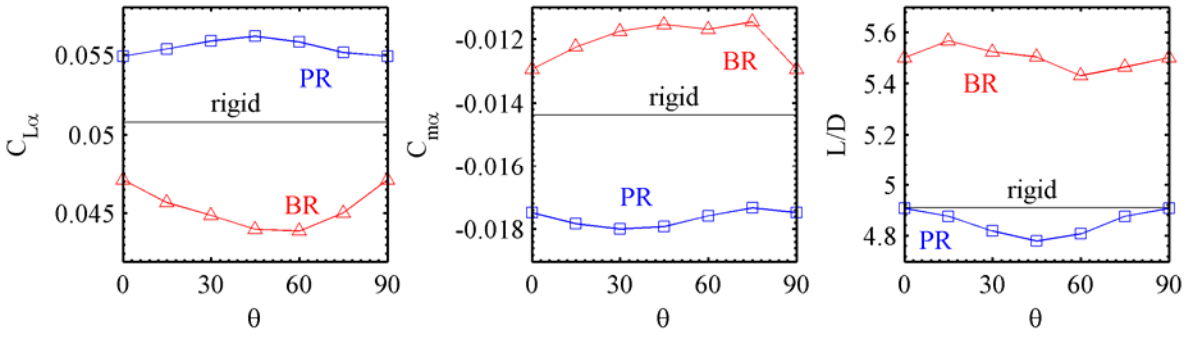

Figure 40. Computed tailoring of laminate orientation for single ply bi-directional carbon fiber, α = 12º.

5.1.3. Double Ply Laminates

Computed aerodynamic derivatives ($C_{L\alpha}$ and $C_{m\alpha}$) and efficiency (L/D) are given as a function of the ply orientations (θ_1 and θ_2) of the two layers of bi-directional plain weave in a BR wing (Figure 41) and a PR wing (Figure 42) at 12° angle of attack. As before, the membrane skin is slack. Aeroelastic trends are expected to repeat every 90°, and will be symmetric about the line $\theta_1 = \theta_2$. This latter point is only true because bending-extension coupling in non-symmetric laminates is ignored, though the effect of its inclusion would be very small as the wing is subjected mostly to normal pressure forces. For the BR wing, efficiency is maximized and the lift slope is minimized when the fibers make 45° angles with the chord and span directions. Static stability is improved when fibers align with the chord. The response surface of the two stability derivatives are very noisy, suggesting possible finite differencing errors, and all three surfaces in Figure 41 show little variation (only $C_{m\alpha}$ of the BR wing can be varied by more than 5%). Unlike any of the tailoring studies discussed above, the PR wing shows the same overall trends and optima as the BR wing. The surfaces for the PR wing are much smoother but have less overall variation.

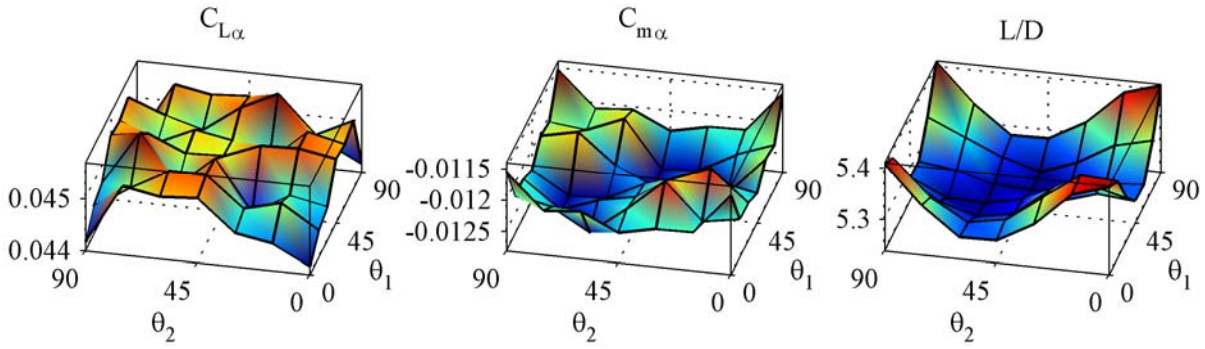

Figure 41. Computed tailoring of laminate orientations for two plies of bi-directional carbon fiber in a BR wing, α = 12°: color contour represents z-axis values.

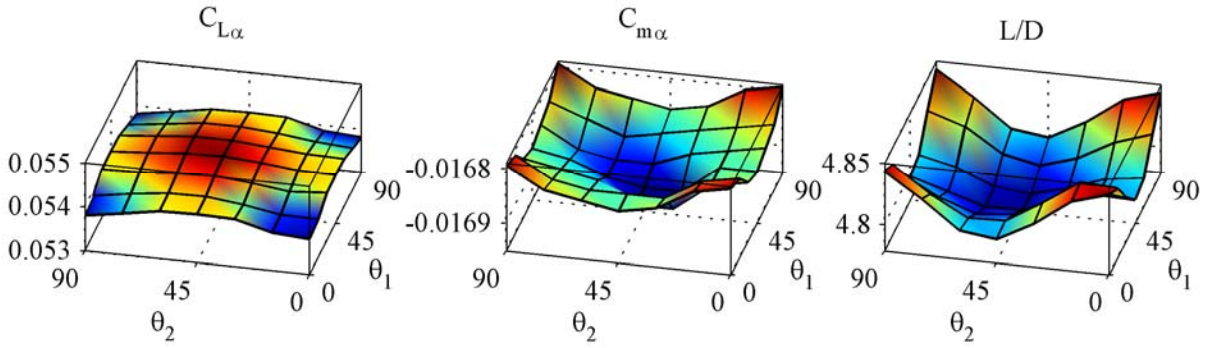

Figure 42. Computed tailoring of laminate orientations for two plies of bi-directional carbon fiber in a PR wing, α = 12°: color contour represents z-axis values.

Of the sampled laminate designs, $[15°]_2$ and $[75°]_2$ will exhibit the greatest bend-twist coupling, yet neither are utilized by the membrane wings. This fact, along with the similarity between the PR and the BR surfaces, suggest that the orientation of a plain weave laminate with two layers is too stiff to have much impact on the aerodynamics, which is dominated by membrane inflation/stretching. The use of bi-directional plain weave is not the most effective means of introducing bend-twist coupling in a laminate. The fact that the two fiber directions within the weave are perpendicular automatically satisfies the balance constraint at angles such as 45°. This would not be the case if plies of uni-directional carbon fiber are utilized, but this is prohibitive in MAV fabrication for the following reason. Curved, unbalanced, potentially non-symmetric thin uni-directional laminates can experience severe thermal warpage when removed from the tooling board, retaining little of the intended shape.

5.1.4. Batten Construction

Computed lift slope and efficiency of a BR wing at 12° angle of attack is given in Figure 43 as a function of the

number of layers in each batten. The thickness of each batten can be varied independently, though the number of layers is limited to three, resulting in 27 possible designs. As before, the membrane skin is slack, and a two-layer plain weave at 45º makes up the remainder of the wing. As expected, the wing with three one-layer battens has the most adaptive washout, which provides the shallowest lift slope, but also the best lift-to-drag ratio. Additional plies, regardless of which batten they are added to, monotonically decreases the efficiency. The same technique can be used to increase $C_{L\alpha}$, except for combinations of stiff battens towards the wing root and a thin outer batten at the wing tip (331 and 332, for example, where the battens are numbered from inner to outer and the integers indicate the number of layers), which causes the slope to decrease from these peaks. Overall changes in the aerodynamics due to batten tailoring are relatively small however, with 5% possible variability in $C_{L\alpha}$ and 1.5% in L/D. Though not shown, the static stability of the BR wing can be varied by 10% with batten tailoring.

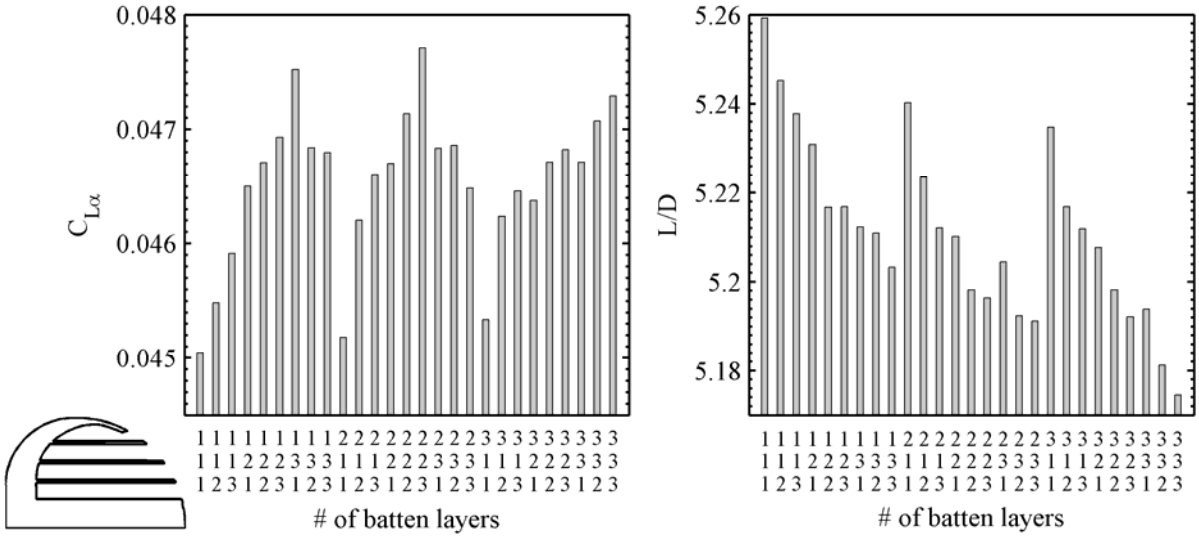

Figure 43. Computed tailoring of batten construction in a BR wing, $\alpha = 12^{\circ}$.

5.2. Full Factorial Designed Experiment

Of the structural sizing/strength parameters discussed above, spanwise membrane pre-tension, chordwise pre-tension, the number of layers of bi-directional plain weave carbon fiber, and the wing type (BR, PR, rigid) are considered in a designed experiment. As stated above, the aeroelasticity of the MAV wing is dominated by the membrane inflation, and the laminate stacking is a secondary effect (though $C_{m\alpha}$ of a BR wing is moderately sensitive to fiber orientation and batten thickness). The number of layers of plain weave carbon fiber, though not explicitly discussed above, is included due to interesting discrepancies between laminate tailoring with one layer (Figure 40) and tailoring with two layers (Figure 41and Figure 42). For this study, the number of layers in each batten is fixed at one, and all plain weaves are oriented at 45º to the chordline.

A three-level, three-variable full factorial designed experiment is implemented for each membrane wing. Only 1, 2, or 3 layers of carbon fiber are permitted, while pre-tension resultant (chordwise or spanwise) is restricted to 0, 10 or 20 N/m. More than 3 layers is excessively stiff and heavy; 1 layer may not be able to withstand flight loads or survive a crash. The upper cap on pre-tension is, as discussed above, meant to prevent batten buckling. Each full factorial design array requires 27 simulations for each membrane wing, a number which must be doubled to obtain finite difference approximations of the lift and moment derivatives in angle of attack. Including the two data points needed for the rigid wing, 110 computationally expensive simulations are required. While a full factorial matrix is not the most economical choice for a designed experiment (a central-composite design is an adequate fraction of the full factorial, for example [146]), the uniform sampling will provide the best insight into the membrane tailoring.

This data is compiled in Figure 44, which plots the performance in terms of the lift slope and pitching moment slope as a function of L/D. As seen many times in the above plots, the various objective functions conflict: tailoring a wing structure for longitudinal static stability may induce a severe drag penalty, for example. No wing design exists (typically) that will optimize all of the relevant performance metrics, and compromise designs must be considered. The set of compromise solutions fall on the design space's Pareto optimal front. A Pareto optimal solution is non-dominated: no solution exists within the data set that out performs the Pareto optimal solution in all

of the performance metrics.

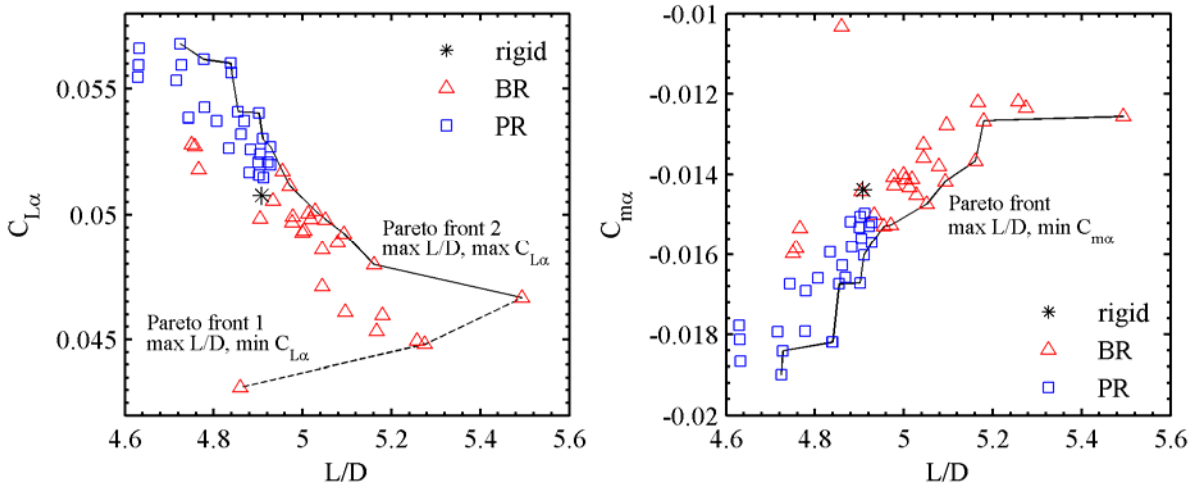

Figure 44. Computed design performance and Pareto optimality, α = 12º.

Three Pareto fronts are given in Figure 44. The first details the tradeoff between maximizing L/D while minimizing $C_{L\alpha}$. The second gives the tradeoff between maximizing L/D while maximizing $C_{L\alpha}$, and the final front is a tradeoff between maximizing L/D while minimizing $C_{m\alpha}$. It may be beneficial for a MAV wing to have a very steep lift slope (for efficient pull-up maneuvers, for example) or very shallow (for gust rejection), so both are included. All three of these objective functions could be used to compute a common Pareto front, but visualization of the resulting hypersurface would be difficult. Furthermore, maximizing $C_{L\alpha}$ and minimizing $C_{m\alpha}$ evolve from similar mechanisms, and seldom conflict.

The overlap between BR wings and PR wings in Figure 44 is minimal, with the latter design typically having higher efficiency and shallow lift and moment slopes. The rigid wing lies close to the interface between the two membrane wing types, but is not Pareto optimal. The basic performance tradeoffs are readily visible: peak L/D is 5.49 (a single-layer BR wing with a slack membrane), a design whose lift slope is 8% higher than the minimum possible lift slope, 18% lower than the maximum possible lift slope, and whose pitching moment slope is 34% higher than the minimum possible moment slope. Most of the dominated solutions do not lie far from the Pareto front, indicative of the fact that all of the objective functions are obtained by integrating the pressure and shear distributions over the wing. Substantial variations in the CFD state variables can be obtained on a local level through the use of wing flexibility (Figure 34, for example), but integration averages out these deviations.

Having successfully implemented the designed experiment, the typical next step is to fit the data with a response surface, a technique used by Sloan et al. [148] and Levin and Shyy [94] for MAV work. Having verified the validity of the surrogate, it can then be used as a relatively inexpensive objective function for optimization. Such a method is not used here for several reasons. First, half of the design variables (wing type and laminate thickness) are discrete, which as discussed by Torres [16], can cause convergence problems in conventional optimization algorithms. Second, nonlinear curve fitting is likely required (membrane wing performance asymptotically approaches that of a rigid wing for increased pre-tension), and the moderate number of data points (only 9 for each wing type and laminate thickness) won't provide enough information for an adequate fit. Finally, such a method may result in an optimal pre-stress resultant of 5.23 N/m, for example. As discussed above, the actual application of pre-tension to a membrane MAV wing is an inexact science, and such resolution could never be produced in the laboratory (or more importantly, the field) with any measure of repeatability or accuracy.

A more practical approach is to simply treat the pre-tension as a discrete variable: taut (~20 N/m), moderate (~10 N/m), and slack (0 N/m). Figure 44 now represent an enumeration-type optimization, wherein every possible design is tested. Optimal wing designs in terms of 7 objective functions (maximum L/D, minimum mass, maximum lift, minimum drag, minimum pitching moment slope, maximum lift slope and minimum lift slope) are located among the 55 available data points, and given along the diagonal of the design array in Table 5. Results from the OFAT tests in Section 5.1 are not included.

Satisfactory compromise designs are found by first normalizing design performance between 0 and 1, and then locating a utopia point. This utopia point is a (typically) fictional design point which would simultaneously

optimize both objective functions. In the design trade-of between L/D and $C_{m\alpha}$ in Figure 44, the utopia point is (5.49, -0.0189). An adequate compromise is the Pareto optimal design which lies closest to the utopia point; these are listed in the off-diagonal cells in Table 5. Only compromises between 2 objective functions are considered in this work. The corresponding performance of each design is given in Table 6. The value in each cell is predicated upon the label at the top of each column; the performance of the second objective function (row-labeled) can be found in the cell appropriately located across the diagonal.

Table 5. Optimal MAV design array with compromise designs on the off-diagonal, α = 12º: design description is (wing type, N_x, N_y, number of plain weave layers).

	max L/D	min mass	max C_L	min C_D	min $C_{m\alpha}$	max $C_{L\alpha}$	min $C_{L\alpha}$
max L/D	**BR,0,0,1L**	BR,0,0,1L	PR,10,0,1L	BR,0,0,1L	BR,20,0,3L	PR,20,0,2L	BR,0,0,1L
min mass	BR,0,0,1L	**PR,20,20,1L**	PR,0,0,1L	BR,0,0,1L	PR,0,10,1L	PR,0,10,1L	BR,20,10,1L
max C_L	PR,10,0,1L	PR,0,0,1L	**PR,0,0,1L**	BR,0,10,1L	PR,0,0,1L	PR,0,0,1L	BR,20,10,1L
min C_D	BR,0,0,1L	BR,0,0,1L	BR,0,10,1L	**BR,0,0,1L**	BR,20,0,3L	BR,10,20,3L	BR,10,0,1L
min $C_{m\alpha}$	BR,20,0,3L	PR,0,10,1L	PR,0,0,1L	BR,20,0,3L	**PR,0,10,1L**	PR,0,10,1L	BR,20,0,3L
max $C_{L\alpha}$	PR,20,0,2L	PR,0,10,1L	PR,0,0,1L	BR,10,20,3L	PR,0,10,1L	**PR,0,10,1L**	BR,0,20,3L
min $C_{L\alpha}$	BR,0,0,1L	BR,20,10,1L	BR,20,10,1L	BR,10,0,1L	BR,20,0,3L	BR,0,20,3L	**BR, 20,10,1L**

Table 6. Optimal MAV design performance array, α = 12º: off-diagonal compromise design performance is predicated by column metrics, not rows.

	max L/D	min mass (g)	max C_L	min C_D	min $C_{m\alpha}$	max $C_{L\alpha}$	min $C_{L\alpha}$
max L/D	**5.49**	4.36	0.780	0.112	-0.015	0.054	0.047
min mass	5.49	**4.10**	0.817	0.112	-0.019	0.057	0.043
max C_L	4.84	4.18	**0.817**	0.145	-0.018	0.056	0.043
min C_D	5.49	4.36	0.716	**0.112**	-0.014	0.052	0.045
min $C_{m\alpha}$	5.05	4.16	0.817	0.134	**-0.019**	0.057	0.049
max $C_{L\alpha}$	4.90	4.16	0.817	0.141	-0.019	**0.057**	0.050
min $C_{L\alpha}$	5.49	4.31	0.673	0.119	-0.015	0.049	**0.043**

At no point does the rigid wing represent an optimum design (compromise or otherwise). The compromise between minimizing the lift slope, and maximizing the lift slope is identified by located the design closest to the normalized $C_{L\alpha}$ of 0.5. This is found by a BR wing design with peak pre-tension normal to the battens to limit adaptive washout, but no pre-tension in the chordwise direction to allow for camber and lift via inflation. Both BR and PR wings are equally-represented throughout the design array, with the exception of designs requiring load alleviation: all compromises involving drag or lift slope minimization utilize a BR wing. The majority of the optimal designs use a single layer of plain weave carbon fiber to take the most advantage of wing flexibility. A single layer slack BR wing can minimize drag through streamlining [101], for example, as a significant portion of the wing is deformed. A few designs use 3 layers; only one design uses 2 layers.

A few compromise wing designs coincide with the utopia point: a one-layer BR wing with a slack membrane maximizes L/D and minimizes the drag. A one-layer PR wing with no pre-tension in the chordwise direction and 10 N/m in the spanwise direction provides the steepest lift slope and pitching moment slope. Most compromise designs improve both objective functions, compared to the rigid wing, but the system particularly struggles to maximize both L/D and lift (above results indicate that efficiency improvements are driven by drag reduction), and to maximize lift and minimize the lift slope. The conflictive nature of the objective functions means that looking at designs that strike a reasonable compromise between three or more aerodynamic metrics is of minor usefulness. It should be noted however, that the design that lies closest to the utopia point of all 7 objectives shown in Table 5 is a 2-layer BR wing with a slack membrane in the chordwise direction, and 10 N/m of pre-tension spanwise, similar to the design that lies closest to the normalized $C_{L\alpha}$ of 0.5, as discussed above. Finally, mass minimization is obviously afforded with a single layer of plain weave carbon fiber: membrane pre-tension then provides moderate and insignificant deviations from this value, by changing the amount of latex used over the MAV wing.

5.3. Experimental Validation of Optimal Design Performance

The design results from the single-objective optimization studies (the diagonal of Table 5, with the exception of the minimum mass design) are fabricated and tested in the wind tunnel. Only loads are measured through the α-sweep, for comparison with the experimental data from the three baseline wings designs discussed in Section 4. As discussed above, each of these wing designs utilize a single layer of plain weave carbon fiber. Two layers are typically used for MAVs of this scale. Despite the extremely compliant nature of the wings (which is precisely why they were located as optimal), all designs are able to withstand flight loads in the wind tunnel without buckling. Whether they can withstand maneuver loads or strong gusts is still unknown however, as is their ability to endure a flight crash without breaking. Some wing designs display substantial leading edge vibration at very low and negative angles of attack (presumably due to the vortex shedding from the separation bubble seen in Figure 33), though deformation is observed to be quasi-static above 3º and prior to stall. The required pre-stress resultants are converted into pre-strains using Hooke's law, and applied to a square of latex rubber by uniformly stretching each side. VIC is used to confirm the pre-strain levels, with spatial coefficients of variation between 10 and 20%, similar to data given in Figure 11 and by Stanford et al. [63].

Results for lift-related optima are given in Figure 45. The design that maximizes C_L (PR,0,0,1L) produces more lift than the baseline PR wing up to 10º angle of attack, though within the error bars (not shown, but on the order of 5%). Above this angle the wing shows a premature stall: $C_{L,\,max}$ is much lower than measured from the baseline PR wing. The vibration and buffeting typically seen over MAV wings towards stall is obviously magnified for these compliant designs. Similar results are seen for the wing design that maximizes $C_{L\alpha}$ (PR,0,10,1L), though in this case the lift slope is nearly identical to that measured from the baseline PR wing up to 10º, after which premature stall occurs. This benign stall behavior is not necessarily detrimental, though unintended by the numerical model, caused by optimizing at a single angle of attack with a steady aeroelastic solver.

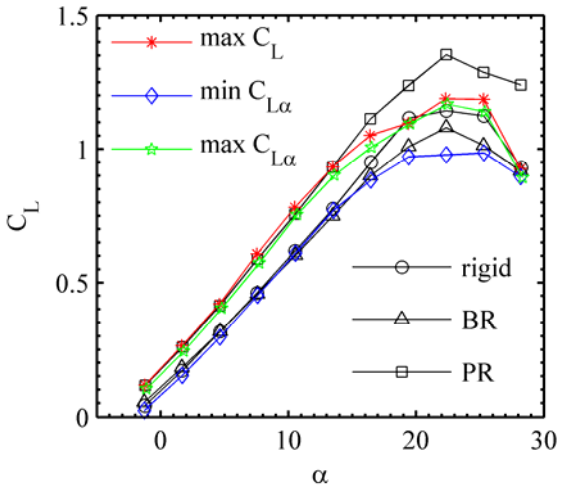

Figure 45. Experimentally measured design optimality over baseline lift.

The optimizer is considerably more successful when minimizing $C_{L\alpha}$ with design (BR,20,10,1L), as seen in Figure 45. At low angles of attack, the lift of the optimal design is smaller than both the baseline rigid and BR wings, though the lift slope is comparable. For moderate angles, no significant differences are evident. After 10º however, the optimal design shows a clear drop in lift slope, a very flat stalling region, and stalling angle delayed by 3º over the baseline designs. $C_{L,\,max}$ is measured to be 9% less than that measured for the baseline BR wing.

Experimental validation results for the wing design minimizing the pitching moment slope (PR,0,10,1L) is given in Figure 46. As before, performance of the baseline PR wing and the optimal design are comparable up to 13º. Above this angle, and through the stalling region, the optimal design has a steeper slope than the baseline PR wing. At these angles, the nose-down pitching moment is stronger than that seen in the baseline BR and rigid wings, but the slope is similar. This is largely due to the linear pitching moment behavior previously noted on the PR wings, possibly due to membrane inflation interference with the tip vortices [27]. Despite the measured improvements over the baseline PR wing, the data indicates that longitudinal control beyond stall (~ 28º) may not be possible [131]. Interestingly, the same wing design theoretically minimizes the moment slope and maximizes the lift slope, but only the former metric is considerably improved over the baseline.

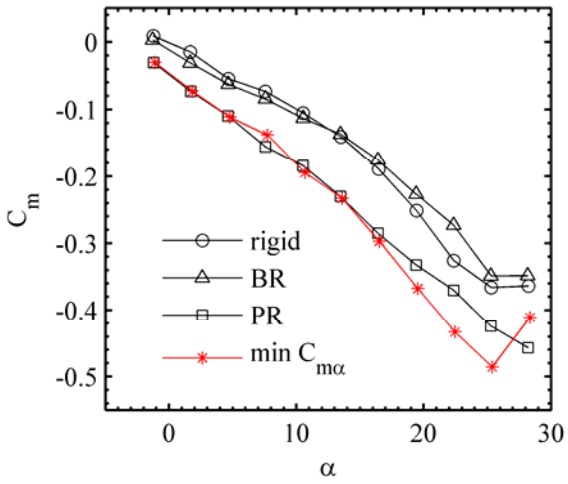

Figure 46. Experimentally measured design optimality over baseline pitching moments.

Similar validation results are given in Figure 47 and Figure 48, for the minimization of drag and maximization of L/D. Both metrics are optimized by wing design (BR,0,0,1L). The drag is consistently lower than the three baseline designs up to 20º. Accurate drag data for micro air vehicles at low speeds is very difficult to measure, largely due to resolution issues in the sting balance [38]. Questionable data typically manifests itself through atypically low drag. Regardless, the veracity of the data from the optimal wing in Figure 47 may be confirmed by the identical results at the bottom of the drag bucket with the rigid wing, where deformation is very small. The data also compares very well with computed results. Unlike the baseline BR wing, the optimal design has less drag at a given angle of attack and at a given value of lift (the latter of which is visible in the drag polar, which is not shown). Past 20º, the optimal design shows more of a drag penalty than the baseline BR wing, which may also be attributed to larger vibration amplitudes in the single-layer wing.

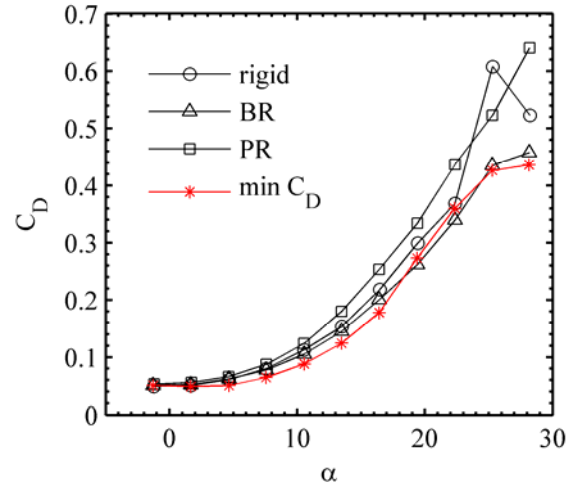

Figure 47. Experimentally measured design optimality over baseline drag.

The results for optimal efficiency (Figure 48) show substantial improvements over the three baseline designs for a range of moderate angles: 8º - 18º. The optimization is only conducted at 12º angle of attack; whereas the previously considered optimal designs can be reasonably considered ideal throughout most of the α-sweep (up to stall), the conflictive nature of the lift-to-drag ratio is more complex. This can be seen in the numerical data of Figure 31, where the baseline BR, PR, and rigid wings all have the highest L/D for different lift values. It is expected that optimizing at different angles of attack will produce radically different optimal L/D designs, but similar results may be retained for the remaining objectives.

Of the six aerodynamic objectives considered in this section, wind tunnel testing indicates that two are unmistakably superior to the baselines over a large range of angles of attack (minimum drag and maximum efficiency), and two have similar responses to one or more of the baseline designs for small and moderate angles but are clearly superior for higher angles of attack (minimum lift and pitching moment slopes). One objective (maximum lift) is slightly better at moderate angles (though not beyond the measured uncertainty), but decidedly inferior during stall, while another objective (maximum lift slope) is identical to the baseline for moderate angles, and again inferior during stall. With the exception of these latter two studies, this wind tunnel validation confirms the use of numerical aeroelastic tailoring for realizable improvements to actual MAV wings. This is not to indicate that the latter two studies have failed: the computed performance of the tailored wings is not always significantly better than the baseline, and may be blurred by experimental errors. The experimental data of these two designs is not significantly better than the baseline designs, but not measurably worse either (for moderate angles).

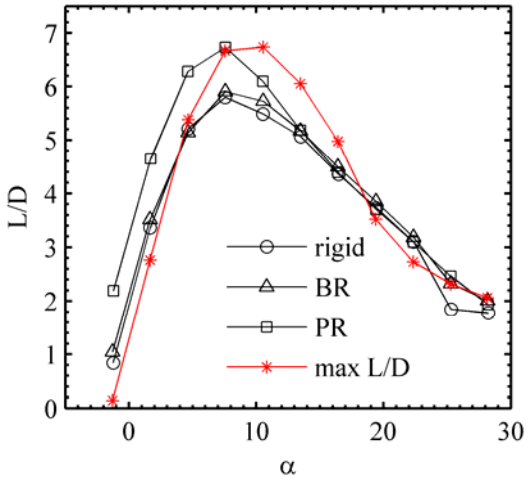

Figure 48. Experimentally measured design optimality over baseline efficiency.

6. Conclusions

The results given in this work detail a recent research effort aimed at understanding and exploiting the static aeroelasticity of membrane micro air vehicle wings, as well as a comprehensive review of the pertinent literature. The flow structures of such wings are exceedingly complex, characterized by low Reynolds numbers (flow separation, laminar-turbulent transition, reattachment, vortex shedding, vortex pairing), low aspect ratios (strong tip vortex swirling, low pressure wing tip cells), and unstable interactions between the two (vortex destabilization for bilateral asymmetry). The wing's structural mechanics are also difficult to predict: a topologically-complex orthotropic wing shell is covered with a thin extensible latex skin, a membrane with an inherently nonlinear response. Two wing topologies are utilized, representing the polar opposites of flexible wing structures: a batten-reinforced design for adaptive geometric twist, and a perimeter-reinforced design for adaptive aerodynamic twist.

No model currently exists that can accurately predict such aeroelasticity in a practical manner (the three-dimensional transition is the biggest numerical hurdle), and so the current work utilizes a steady laminar Navier-Stokes solver coupled to a nonlinear membrane finite element model. Due to the lower-fidelity nature of the model (despite which, the computational cost of this coupled aeroelastic simulation is very large), experimental model validation is required. Such characterization is conducted in a low speed closed loop wind tunnel. Aerodynamic forces and moments are measured using a strain gage sting balance with an estimated resolution of 0.01 N. Structural displacement and strain measurements are made with a visual image correlation system; a calibrated camera system is mounted over the test section.

At small angles of attack, the low Reynolds number flow beneath a MAV wing separates across the leading edge camber, the flow over the upper surface is largely attached, and the tip-vortex swirling system is weak. The opposite is true has the incidence is increased: the separation bubble on the upper surface grows, eventually leading to stall. The lift curves of the low aspect ratio wings are typically shallow, with a large stalling angle. Low pressure cells deposited on the upper surface of the wing tip by the vortex swirling grow with angle of attack, and lead to slight nonlinearities in the lift and pitching moment trends.

The structural deformation of a batten-reinforced wing has two main trends: the forces towards the leading edge

are very large, and induce membrane inflation in-between the battens. This increases the camber over the wing, and thus the lift. A second trend comes from the free trailing edge of the BR wing, which deflects upward for a nose-down twist, decreasing the wing lift. These two effects tend to offset for lower angles of attack, and the aerodynamics follow the rigid wing's very closely. At higher angles the adaptive washout dominates, decreasing the incidence of a wing section by as much as 5º and decreasing the slope of the wing's lift curve. Outside of the promise such a wing shows for gust rejection and benevolent stall, the data also indicates that the streamlining decreases drag. The strain field of the BR membrane wing is largely one-dimensional: the directional influence of the battens prevents appreciable chordwise stretching.

The deformation of a perimeter-reinforced wing is characterized by adaptive aerodynamic twist: the membrane skin inflates, constrained at the leading and trailing edges by the stiff carbon fiber perimeter. Lift, drag, and pitching moments are consistently stronger than measured from the rigid and BR wings, as a result of the cambering motion. The slope of the pitching moment curve is considerably steeper, providing much-needed longitudinal static stability to a wing with severe space and weight constraints. The large drag penalty of the wing is partly due to a pressure spike at the tangent discontinuity between the inflated membrane and the carbon fiber, and partly due to the greater amount of separated flow over the PR wing. Interactions between the separated longitudinal flow and the wing tip vortices are clearly visible in the PR wing, possibly indicating a greater propensity for rolling instabilities. The stretching of the membrane skin in the PR wing is more two-dimensional without the restrictive presence of battens.

It is shown, both numerically and experimentally, that unconventional aeroelastic tailoring can be used to improve MAV wing performance. The chordwise and spanwise membrane pre-tension, number of plain weave carbon fiber layers, laminate orientation, and batten thickness are all considered, with the first three variables identified as critical. Increasing stiffness is seen to tend aerodynamic behavior towards a rigid wing, thought many local optima exist and can be exploited. A comprehensive numerical review of the design space is provided with a full factorial designed experiment of the three aforementioned variables. This data is then used to optimize six aerodynamic variables, as well as compromises between each. The six designs resulting from the single-objective optimizations are built and tested in the wind tunnel: five show improvements over the baseline designs, one has a similar response.

While the current results (particularly the wind tunnel validation of the numerical aeroelastic tailoring) are encouraging, higher-fidelity models can provide greater insight towards effective tailoring. This is particularly obvious in Figure 45, where unsteady vortex shedding and wing vibration (not included in the model) eliminate the supposed optimality of the maximum lift slope wing design at higher angles. A formal search optimization considering all of the structural variables (rather than the abbreviated set used in the designed experiment) is also recommended, though the logistics are formidable: mixed variables, non-convex Pareto fronts, large computational cost, etc. Further numerical inclusions would be turbulence/transition modeling, prediction of wing fracture upon crash impact, and high-fidelity methods for computing pre-tension fields. As noted above, accurate implementation of wing skin pre-tension can be difficult in the laboratory or the field, though properly applied tension has well-demonstrated aerodynamic advantages. Anisotropic membrane skins (through imbedded fibers, for example) may be used to alleviate such problems.

Acknowledgements

This work was jointly supported by the Air Force Research Laboratory and the Air Force Office of Scientific Research under the MURI program F49620-03-1-0381. The authors would also like to acknowledge the contributions provided by Dr. Dragos Viieru at the University of Florida and Dr. Paul Hubner at the University of Alabama.

References

[1] Ailinger, K., "U.S. Navy Micro Air Vehicle Development," *International UAV Conference*, Bristol, UK, Apr. 12-14, 1999.

[2] Torres, G., Mueller, T., "Micro Aerial Vehicle Development: Design, Components, Fabrication, and Flight Testing," *AUVSI Unmanned Systems Symposium and Exhibition*, Orlando, FL, July 11-13, 2000.

[3] Grasmeyer, J., Keenon, M., Development of the Black Widow Micro Air Vehicle," *AIAA Aerospace Sciences Meeting and Exhibit*, Reno, NV, Jan. 8-11, 2001.

[4] Ifju, P., Jenkins, D., Ettinger, S., Lian, Y., Shyy, W., Waszak, M., "Flexible-Wing-Based Micro Air Vehicles," *Confederation of European Aerospace Societies Aerodynamics Conference*, London, UK, June 10-12, 2003.

[5] Shkarayev, S., Null, W., Wagner, M., "Development of Micro Air Vehicle Technology with In-Flight Adaptive-Wing Structure," *NASA Contractor Report*, CR-213271, 2004.

[6] Sun, D., Wu, H., Zhu, R., Hung, L., "Development of Micro Air Vehicle Based on Aerodynamic Modeling Analysis in Tunnel Tests," *IEEE International Conference on Robotics and Automation*, Barcelona, Spain, Apr. 18-22, 2005.
[7] Settles, G., "Fluid Mechanics and Homeland Security," *Annual Review of Fluid Mechanics*, Vol. 38, No. 1, pp. 87-110, 2006.
[8] Brewer, K., "High-Tech Micro Air Vehicle will Battle with Soldiers," United States Department of Defense Transformation, http://www.defenselink.mil/transformation/articles/2005-11/ta110105c.html, Nov. 2005.
[9] Air Force Scientific Advisory Board, *New World Vistas: Air and Space Power for the 21st Century, Summary Volume*, Washington, DC, 1995.
[10] Nair, M., "Conceptual Design, Engineering Modeling, and Experimental Validation of Air Sampling System for Chemical Sensor Insertion into the U.S. Army Research Laboratory's Silent Operating Aerial Reconnaissance Program," *ARL Technical Report*, TR 3105, 2004.
[11] Grady, M., "UAVs Tested as Fire Spotters," AVweb, http://www.avweb.com/avwebflash/briefs/188894-1.html, Jan. 2005.
[12] Shyy, W., Lian, Y., Tang, J., Viieru, D., Liu, H., *Aerodynamics of Low Reynolds Number Flyers*, Cambridge University Press, New York, NY, 2008.
[13] Jenkins, D., Ifju, P., Abdulrahim, M., Olipra, S., "Assessment of the Controllability of Micro Air Vehicles," *Bristol International RPV/UAV Conference*, Bristol, UK, Apr. 2-4, 2001.
[14] Abdulrahim, M., Garcia, H., Lind, R., "Flight Characteristics of Shaping the Membrane Wing of a Micro Air Vehicle," *Journal of Aircraft*, Vol. 42, No. 1, pp. 131-137, 2005.
[15] Young, A., Horton, H, "Some Results of Investigation of Separation Bubbles," *AGARD Conference Proceedings*, No. 4, pp. 779-811, 1966.
[16] Torres, G., "Aerodynamics of Low Aspect Ratio Wings at Low Reynolds Numbers with Applications to Micro Air Vehicle Design," Ph.D. Dissertation, Department of Aerospace and Mechanical Engineering, University of Notre Dame, South Bend, IN, 2002.
[17] Shyy, W., Ifju, P., Viieru, D., "Membrane Wing-Based Micro Air Vehicles," *Applied Mechanics Reviews*, Vol. 58, No. 4, pp. 283-301, 2005.
[18] Hoerner, S., Borst, H., *Fluid-Dynamic Lift*, Hoerner Fluid Dynamics, Brick Town, NJ, 1975.
[19] Tang, J., Zhu, K., "Numerical and Experimental Study of Flow Structure of Low-Aspect Ratio Wing," *Journal of Aircraft*, Vol. 41, No. 5, pp. 1196-1201, 2004.
[20] Lian, Y., Shyy, W., "Laminar-Turbulent Transition of a Low Reynolds Number Rigid or Flexible Airfoil," *AIAA Journal*, Vol. 45, No. 7, 2007.
[21] Albertani, R., Stanford, B., Hubner, J., Ifju, P., "Aerodynamic Coefficients and Deformation Measurements on Flexible Micro Air Vehicle Wings," *Experimental Mechanics*, Vol. 47, No. 5, pp. 625-635, 2007.
[22] Shirk, M., Hertz, T., Weisshaar, T., "Aeroelastic Tailoring-Theory, Practice and Promise," *Journal of Aircraft*, Vol. 23, No. 1, pp. 6-18, 1986.
[23] Griffin, C., "Pressure Deflection Behavior of Candidate Materials for a Morphing Wing," Masters Thesis, Department of Mechanical and Aerospace Engineering, West Virginia University, Morgantown, WV, 2007.
[24] Pawlowski, K., Belvin, H., Raney, D., Su, J., Harrison, J., Siochi, E., "Electrospinning of a Micro Air Vehicle Wing," *Polymer Communication*, Vol. 44, No. 4, pp. 1309-1314, 2003.
[25] Xu, Y., Jiang, F., Newbern, S., Huang, A., Ho, C., Tai, Y., "Flexible Shear-Stress Sensor Skin and its Application to Unmanned Aerial Vehicles," *Sensors and Actuators*, Vol. 105, No. 3, pp. 321-329, 2003.
[26] Waszak, M., Jenkins, L., Ifju, P., "Stability and Control Properties of an Aeroelastic Fixed Wing Micro Air Vehicle," *AIAA Atmospheric Flight Mechanics Conference and Exhibit*, Montreal, Canada, Aug. 6-9, 2001.
[27] Stanford, B., Ifju, P., "Membrane Micro Air Vehicles with Adaptive Aerodynamic Twist: Numerical Modeling," *AIAA Structures, Structural Dynamics, and Materials Conference*, Honolulu, HI, Apr. 23-26, 2007.
[28] Lin, J., Pauley, L., "Low-Reynolds-Number Separation on an Airfoil," *AIAA Journal*, Vol. 34, No. 8, pp. 1570-1577, 1996.
[29] Persson, P., Peraire, J., Bonet, J., "A High Order Discontinuous Galerkin Method for Fluid-Structure Interaction," *AIAA Computational Fluid Dynamics Conference*, Miami, FL, June 25-28, 2007.
[30] Lian, Y., Shyy, W., Viieru, D., Zhang, B., "Membrane Wing Mechanics for Micro Air Vehicles," *Progress in Aerospace Sciences*, Vol. 39, No. 6, pp 425-465, 2003.
[31] Bisplinghoff, R., Ashley, H., Halfman, R., *Aeroelasticity*, Dover, Mineola, NY, 1955.
[32] Ho, S., Nassef, H., Pornsinsirirak, N., Tai, Y., Ho, C., "Unsteady Aerodynamics and Flow Control for Flapping Wing Flyers," *Progress in Aerospace Sciences*, Vol. 39, No. 8, pp. 635-681, 2003.

[33] Ormiston, R., "Theoretical and Experimental Aerodynamics of the Sail Wing," *Journal of Aircraft*, Vol. 8, No. 2, pp. 77-84, 1971.
[34] Fitt, A., Pope, M., "The Unsteady Motion of Two-Dimensional Flags With Bending Stiffness," *Journal of Engineering Mechanics*, Vol. 40, No. 3, pp. 227-248, 2001.
[35] Alexander, D., Vogel, S., *Nature's Flyers: Birds, Insects, and the Biomechanics of Flight*, John Hopkins University Press, Baltimore, MD, 2002.
[36] Wilkinson, M, "Sailing the Skies: the Improbable Aeronautical Success of the Pterosaurs," *Journal of Experimental Biology*, Vol. 210, No. 10, pp. 1663-1671, 2007.
[37] Greenhalgh, S., Curtiss, H., Smith, B., "Aerodynamic Properties of a Two-Dimensional Inextensible Flexible Airfoil," *AIAA Journal*, Vol. 22, No. 7, pp. 865-870, 1984.
[38] Mueller, T., "Aerodynamic Measurements at Low Reynolds Numbers for Fixed Wing Micro-Air Vehicles," *RTO Special Course on the Development and Operation of UAVs for Military and Civil Applications*, Von Karman Institute, Belgium, Sep. 13-17, 1999.
[39] Burner, A., Fleming, G., Hoppe, J., "Comparison of Three Optical Methods for Measuring Model Deformation," *AIAA Aerospace Sciences Meeting and Exhibit*, Reno, NV, Jan. 10-13, 2000.
[40] Kaplan, S., Altman, A., Ol, M., "Wake Vorticity Measurements for Low Aspect Ratio Wings at Low Reynolds Numbers," *Journal of Aircraft*, Vol. 44, No. 1, pp. 241-251, 2007.
[41] Tamai, M., Murphy, J., Hu, H., "An Experimental Study of Flexible Membrane Airfoils at Low Reynolds Numbers," *AIAA Aerospace Sciences Meeting and Exhibit*, Jan. 7-10, Reno, NV, 2008.
[42] Sytsma, M., "Aerodynamic Flow Characterization of Micro Air Vehicles Utilizing Flow Visualization Methods," Masters Thesis, Department of Mechanical and Aerospace Engineering, University of Florida, Gainesville, FL, 2006.
[43] Pujara, P., Lardner, T., "Deformations of Elastic Membranes – Effect of Different Constituitive Relations," *Zeitschrift für Angewandte Mathematik und Physik*, Vol. 29, No. 2, pp. 315-327, 1978.
[44] Sugimoto, T., "Analysis of Circular Elastic Membrane Wings," *Transactions of the Japanese Society of Aerodynamics and Space Sciences*, Vol. 34, No. 105, pp. 154-166, 1991.
[45] Heppel, P., "Accuracy in Sail Simulation: Wrinkling and Growing Fast Sails," *High Performance Yacht Design Conference*, Auckland, New Zealand, Dec. 4-6, 2002.
[46] Pellettier, A., Mueller, T., "Low Reynolds Number Aerodynamics of Low Aspect Ratio Thin/Flat/Cambered-Plate Wings," *Journal of Aircraft*, Vol. 37, No. 5, pp. 825-832, 2000.
[47] Hunt, R., Hornby, G., Lohn, J., "Toward Evolved Flight," *Genetic and Evolutionary Computation Conference*, Washington, DC, June 25-29, 2005.
[48] Gili, P., Battipede, M., "Experimental Validation of the Wing Dihedral Effect Using Whirling Arm Equipment," *Journal of Aircraft*, Vol. 38, No. 6, pp. 1069-1075, 2001.
[49] Babinsky, H., Cattafesta, L., Abate, G., "Design Considerations for a Micro Aerial Vehicle Aerodynamic Characterization Facility at the University of Florida Research and Engineering Education Facility," *AIAA Aerodynamic Measurement Technology and Ground Testing Conference*, San Francisco, CA, June 5-8, 2006.
[50] Carmichael, B., "Low Reynolds Number Airfoil Survey," *NASA Contractor Report*, CR 165803, 1981.
[51] Mueller, T., "The Influence of Laminar Separation and Transition on Low Reynolds Number Airfoil Hysteresis," *Journal of Aircraft*, Vol. 22, No. 9, pp. 763-770, 1985.
[52] Marchman, J., "Aerodynamic Testing at Low Reynolds Numbers," *Journal of Aircraft*, Vol. 24, No. 2, pp. 107-114, 1987.
[53] Kochersberger, K., Abe, C., "A Novel, Low Reynolds Number Moment Balance Design for Micro Air Vehicle Research," *AIAA Fluid Dynamics Conference and Exhibit*, Toronto, Canada, June 6-9, 2005.
[54] Suhariyono, A., Kim, J., Goo, J., Park, N., Yoon, K., "Design of Precision Balance and Aerodynamic Characteristic Measurement System for Micro Air Vehicles," *Aerospace Science and Technology*, Vol. 10, No. 2, pp. 92-99, 2006.
[55] Ifju, P., Albertani, R., Stanford, B., Claxton, D., Sytsma, M., "Flexible-Wing Micro Air Vehicles," Chapter 5 in *Introduction to the Design of Fixed-Wing Micro Air Vehicles*, Mueller, T., Kellogg, J., Ifju, P., Shkarayev, S., (editors), AIAA, Reston, VA, 2007.
[56] Recommended Practice R-091-2003, "Calibration and Use of Internal Strain-Gage Balances with Application to Wind Tunnel Testing," AIAA, Reston, VA, 2003.
[57] Moschetta, J., Thipyopas, C., "Aerodynamic Performance of a Biplane Micro Air Vehicle," *Journal of Aircraft*, Vol. 44, No. 1, pp. 291-299, 2007.

[58] Albertani, R., "Experimental Aerodynamics and Elastic Deformation Characterization of Low Aspect Ratio Flexible Fixed Wings Applied to Micro Aerial Vehicles," Ph.D. Dissertation, Department of Mechanical and Aerospace Engineering, University of Florida, Gainesville, FL, 2005.
[59] Newman, B., Low H., "Two-Dimensional Impervious Sails: Experimental Results Compared with Theory," *Journal of Fluid Mechanics*, Vol. 144, pp. 445-462, 1984.
[60] Galvao, R., Israeli, E., Song, A., Tian, X., Bishop, K., Swartz, S., Breuer, K., "The Aerodynamics of Compliant Membrane Wings Modeled on Mammalian Flight Mechanics," *AIAA Fluid Dynamics Conference and Exhibit*, San Francisco, CA, June 5-8, 2006.
[61] Shyy, W., Jenkins, D., Smith, R., "Study of Adaptive Shape Airfoils at Low Reynolds Number in Oscillatory Flows," *AIAA Journal*, Vol. 35, No. 9, pp. 1545-1548, 1996.
[62] Kline, S., McClintock, F., "Describing Uncertainties in Single-Sample Experiments," *Mechanical Engineering*, Vol. 75, No. 1, pp. 3-8, 1953.
[63] Stanford, B., Sytsma, M., Albertani, R., Viieru, D., Shyy, W., Ifju, P., "Static Aeroelastic Model Validation of Membrane Micro Air Vehicle Wings," *AIAA Journal*, Vol. 45, No. 12, pp. 2828-2837, 2007.
[64] Pankhurst, R., Holder, D., *Wind Tunnel Technique*, Sir Isaac Pitman and Sons, London, UK, 1952.
[65] Barlow, J., Rae, W., Pope, A., *Low-Speed Wind Tunnel Testing*, Wiley, New York, NY, 1999.
[66] Fleming, G., Bartram, S., Waszak, M., Jenkins, L., "Projection Moiré Interferometry Measurements of Micro Air Vehicle Wings," SPIE Paper 4448-16.
[67] Sutton, M., Turner, J., Bruck, H., Chae, T., "Full Field Representation of the Discretely Sampled Surface Deformation for Displacement and Strain Analysis," *Experimental Mechanics*, Vol. 31, No. 2, pp. 168-177, 1991.
[68] Orteu, J., "3-D Computer Vision in Experimental Mechanics," *Optics and Lasers in Engineering*, DOI:10.1016./j.optlaseng.2007.11.009.
[69] Schreier, H., Braasch, J., Sutton, M., "Systematic Errors in Digital Image Correlation caused by Intensity Interpolation," *Optical Engineering*, Vol. 39, No. 11, pp. 2915-2921, 2000.
[70] Sutton, M., McFadden, C., "Development of a Methodology for Non-Contacting Strain Measurements in Fluid Environments Using Computer Vision," *Optics and Lasers in Engineering*, Vol. 32, No. 4, pp. 367-377, 2000.
[71] Albertani, R., Stanford, B., Sytsma, M., Ifju, P., "Unsteady Mechanical Aspects of Flexible Wings: an Experimental Investigation Applied to Biologically Inspired MAVs," *European Micro Air Vehicle Conference and Flight Competition*, Toulouse, France, Sep. 17-21, 2007.
[72] Rojratsirikul, P., Wang, Z., Gursul, I., "Unsteady Aerodynamics of Membrane Airfoils," *AIAA Aerospace Sciences Meeting and Exhibit*, Reno, NV, Jan. 7-10, 2008.
[73] Lorillu, O., Weber, R., Hureau, J., "Numerical and Experimental Analysis of Two-Dimensional Separated Flows over a Flexible Sail," *Journal of Fluid Mechanics*, Vol. 466, pp. 319-341, 2002.
[74] Parks, H., "Three-Component Velocity Measurements in the Tip Vortex of a Micro Air Vehicle," Masters Thesis, School of Engineering and Management, Air Force Institute of Technology, Wright Patterson Air Force Base, OH, 2006.
[75] Gamble, B., Reeder, M., "Experimental Analysis of Propeller Interactions with a Flexible Wing Micro Air Vehicle," *AIAA Fluid Dynamics Conference and Exhibit*, San Francisco, CA, June 5-8, 2006.
[76] Charvet, T., Hauville, F., Huberson, S., "Numerical Simulation of the Flow Over Sails in Real Sailing Conditions," *Journal of Wind Engineering and Industrial Aerodynamics*, Vol. 63, No. 1, pp. 111-129, 1996.
[77] Argentina, M., Mahadevan, L., "Fluid-Flow-Induced Flutter of a Flag," *Proceedings of the National Academy of Science: Applied Mathematics*, Vol. 102, No. 6, pp. 1829-1834, 2005.
[78] Voelz, K., "Profil und Auftrieb Eines Segels," *Zeitschrift f'ur Angewandte Mathematik und Mechanik*, Vol. 30, pp. 301-317, 1950.
[79] Thwaites, B., "The Aerodynamic Theory of Sails," *Proceedings of the Royal Society of London*, Vol. 261, No. 1306, pp. 402-422, 1961.
[80] Nielsen, J., "Theory of Flexible Aerodynamic Surfaces," *Journal of Applied Mechanics*, Vol. 30, No. 3, pp. 435-442, 1963.
[81] Haselgrove, M., Tuck, E., "Stability Properties of the Two-Dimensional Sail Model," *Society of Naval Architects and Marine Engineers New England Sailing Yacht Symposium*, New London, CN, Jan. 24, 1976.
[82] Jackson, P., "A Simple Model for Elastic Two-Dimensional Sails," *AIAA Journal*, Vol. 21, No. 1, pp.153-155, 1983.
[83] Sneyd, A., Bundock, M., Reid, D., "Possible Effects of Wing Flexibility on the Aerodynamics of Pteranodon," *The American Naturalist*, Vol. 120, No. 4, pp. 455-477, 1982.

[84] Greenhalgh, S., Curtiss, H., Smith, J., "Aerodynamic Properties of a Two-Dimensional Inextensible Flexible Airfoil," *AIAA Journal*, Vol. 22, No. 7, pp. 865-870, 1984.
[85] Boudreault, R., "3-D Program Predicting the Flexible Membrane Wings Aerodynamic Properties," *Journal of Wind Engineering and Industrial Aerodynamics*, Vol. 19, No. 1, pp. 277-283, 1985.
[86] Holla, V., Rao, K., Arokkiaswamy, A., Asthana, C., "Aerodynamic Characteristics of Pretensioned Elastic Membrane Rectangular Sailwings," *Computer Methods in Applied Mechanics and Engineering*, Vol. 44, No. 1, pp. 1-16, 1984.
[87] Murai, H., Murayama, S., "Theoretical Investigation of Sailwing Airfoils Taking Account of Elasticities," *Journal of Aircraft*, Vol. 19, No. 5, pp.385-389, 1982.
[88] Jackson, P., Christie, G., "Numerical Analysis of Three-Dimensional Elastic Membrane Wings," *AIAA Journal*, Vol. 25, No. 5, pp. 676-682, 1987.
[89] Smith, R., Shyy, W., "Incremental Potential Flow Based Membrane Wing Element," *AIAA Journal*, Vol. 35, No. 5, pp. 782-788, 1997.
[90] Schoop, H., Bessert, N., Taenzer, L., "On the Elastic Membrane in a Potential Flow," *International Journal for Numerical Methods in Engineering*, Vol. 41, No. 2, pp. 271-291, 1998.
[91] Smith, R., Shyy, W., "Computational Model of Flexible Membrane Wings in Steady Laminar Flow," *AIAA Journal*, Vol. 33, No. 10, pp. 1769-1777, 1995.
[92] Cyr, S., Newman, B., "Flow Past Two-Dimensional Membrane Aerofoils with Rear Separation," *Journal of Wind Engineering and Industrial Aerodynamics*, Vol. 63, No. 1, pp. 1-16, 1996.
[93] Smith, W., Shyy, W., "Coupled Computations of a Flexible Membrane Wing in Unsteady Viscous Flow," *AIAA Fluid Dynamics Conference*, San Diego, CA, June 19-22, 1995.
[94] Levin, O., Shyy, W., "Optimization of a Low Reynolds Number Airfoil with Flexible Membrane," *Computer Modeling in Engineering and Sciences*, Vol. 2, No. 4, pp. 523-536, 2001.
[95] Gordnier, R., "High Fidelity Computational Simulation of a Membrane Wing Airfoil," *AIAA Aerospace Sciences Meeting and Exhibit*, Reno, NV, Jan. 7-10, 2008.
[96] Viieru, D., "Flapping and Fixed Wing Aerodynamics of Low Reynolds Number Flight Vehicles," Ph.D. Dissertation, Department of Mechanical and Aerospace Engineering, University of Florida, Gainesville, FL, 2006.
[97] Smith, R., Shyy, W., "Computation of Aerodynamic Coefficients for a Flexible Membrane Airfoil in Turbulent Flow: A Comparison with Classical Theory," *Physics of Fluids*, Vol. 8, No. 12, pp. 3346-3353, 1996.
[98] Chakrabarti, S., Brebbia, C., "A Two-Dimensional Sail in Turbulent Flow," *Advances in Fluid Mechanics*, Vol. 30, No. 16, pp. 245-254, 2001.
[99] Scott, R., Bartels, R., Kandil, O., "An Aeroelastic Analysis of a Thin Flexible Membrane," *AIAA Structures, Structural Dynamics, and Materials Conference*, Honolulu, HI, Apr. 23-26, 2007.
[100] Lian, Y., Shyy, W., Ifju, P., Verron, E., "A Computational Model for Coupled Membrane-Fluid Dynamics," *AIAA Fluid Dynamics Conference and Exhibit*, St. Louis, MO, June 24-26, 2002.
[101] Alben, S., Shelley, M., Zhang, J., "How Flexibility Induces Streamlining in a Two-Dimensional Flow," *Physics of Fluids*, Vol. 16, No. 5, pp. 1694-1713, 2004.
[102] Stanford, B., Albertani, R., Ifju, P., "Static Finite Element Validation of a Flexible Micro Air Vehicle," *Experimental Mechanics*, Vol. 47, No. 2, pp. 283-294, 2007.
[103] Ferguson, L., Seshaiyer, P., Gordnier, R., Attar, P., "Computational Modeling of Coupled Membrane-Beam Flexible Wings for Micro Air Vehicles," *AIAA Structures, Structural Dynamics, and Materials Conference*, Honolulu, HI, Apr. 23-26, 2007.
[104] Batoz, J., Bathe, K., Ho, L., "A Study of Three-Node Triangular Plate Bending Elements," *International Journal for Numerical Methods in Engineering*, Vol. 15, No. 12, pp. 1771-1812, 1980.
[105] Cook, R., Malkus, D., Plesha, M., Witt, R., *Concepts and Applications of Finite Element Analysis*, Wiley, New York, NY, 2002.
[106] Reaves, M., Horta, L., Waszak, M., Morgan, B., "Model Update of a Micro Air Vehicle (MAV) Flexible Wing Frame with Uncertainty Quantification," *NASA Technical Memorandum*, TM 213232, 2004.
[107] Isenberg, C., *The Science of Soap Films and Soap Bubbles*, Dover, New York, NY, 1992.
[108] Taylor, R., Onate, E., Ubach, P., "Finite Element Analysis of Membrane Structures," in *Textile Composites and Inflatable Structures*, Onate, E., Kröplin, B (editors), Springer, Dordrecht, The Netherlands, 2005.
[109] Pauletti, R., Guirardi, D., Deifeld, T., "Argyris' Natural Finite Element Revisited," *International Conference on Textile Composites and Inflatable Structures*, Stuttgart, Germany, Oct. 2-5, 2005.
[110] Wu, B., Du, X., Tan, H., "A Three-Dimensional FE Nonlinear Analysis of Membranes," *Computers and Structures*, Vol. 59, No. 4, pp. 601-605, 1996.

[111] Campbell, J., "On the Theory of Initially Tensioned Circular Membranes Subjected to Uniform Pressure," *Quarterly Journal of Mechanics and Applied Mathematics*, Vol. 9, No. 1, pp. 84-93, 1956.
[112] Mooney, M., "A Theory of Large Elastic Deformation," *Journal of Applied Physics*, Vol. 11, pp. 582-592, 1940.
[113] Oden, J., Sato, T., "Finite Strains and Displacements of Elastic Membranes by the Finite Element Method," *International Journal of Solids and Structures*, Vol. 3, pp. 471-488, 1967.
[114] Mase, G., Mase, G., *Continuum Mechanics for Engineers*, CRC Press, Boca Raton, FL, 1999.
[115] Stanford, B., Boria, F., Ifju, P., "The Validity Range of Pressurized Membrane Models with Varying Fidelity," *Society for Experimental Mechanics*, Springfield, MA, June 4-6, 2007.
[116] Ramamurti, R., Sandberg, W., Löhner, R., "Simulation of the Dynamics of Micro Air Vehicles," *AIAA Aerospace Sciences Meeting and Exhibit*, Reno, NV, Jan. 10-13, 2000.
[117] Gad-el-Hak, M., "Micro-Air-Vehicles: Can They be Controlled Better?" *Journal of Aircraft*, Vol. 38, No. 3, pp. 419-429, 2001.
[118] Viieru, D., Albertani, R., Shyy, W., Ifju, P., "Effect of Tip Vortex on Wing Aerodynamics of Micro Air Vehicles," *Journal of Aircraft*, Vol. 42, No. 6, pp. 1530-1536, 2005.
[119] Kunz, P., Kroo, I., "Analysis and Design of Airfoils for Use at Ultra-Low Reynolds Numbers," Chapter 3 in *Fixed and Flapping Wing Aerodynamics for Micro Air Vehicle Applications*, Mueller, T (editor), AIAA, Reston, VA, 2002.
[120] Baragona, M., Bijl, H., Van Tooren, M., "Bubble Bursting and Laminar Separation Unsteadiness on a Multi-Element High Lift Configuration," *Flow, Turbulence and Combustion*, Vol. 71, No. 2, pp. 279-296, 2003.
[121] Tannehill, J., Anderson, D., Pletcher, R., *Computational Fluid Mechanics and Heat Transfer*, Taylor and Francis, Philadelphia, PA, 1997.
[122] Shyy, W., *Computational Modeling for Fluid Flow and Interfacial Transport*, Elsevier, Amsterdam, The Netherlands, 1994.
[123] Thakur, S., Wright, J., Shyy, W., "STREAM: A Computational Fluid Dynamics and Heat Transfer Navier-Stokes Solver: Theory and Applications," Streamline Numerics, Inc., Gainesville, FL, 2002.
[124] Krumbein, A., "Automatic Transition Prediction and Application to Three-Dimensional High-Lift Configurations," *Journal of Aircraft*, Vol. 44, No. 3, pp. 918-926, 2007.
[125] Roberts, S., Yaras, M., "Large-Eddy Simulation of Transition in a Separation Bubble," *Journal of Fluids Engineering*, Vol. 128, No. 2, pp. 232-238, 2006.
[126] Shan, H., Jiang, L., Liu, C., Love, M., Maines, B., "Numerical Study of Passive and Active Flow Separation Control over a NACA0012 Airfoil," *Computers and Fluids*, DOI:10.1016/j.compfluid.2007.10.010.
[127] Guruswamy, G., "A Review of Numerical Fluids/Structures Interface Methods for Computations Using High-Fidelity Equations," *Computers and Structures*, Vol. 80, No. 1, pp. 31-41, 2002.
[128] Lewis, W., *Tension Structures: Form and Behavior*, Thomas Telford Ltd, London, UK, 2003.
[129] Kamakoti, R., Lian, Y., Regisford, S., Kurdila, A., Shyy, W., "Computational Aeroelasticity Using a Pressure-Based Solver," *Computer Methods in Engineering and Sciences*, Vol. 3, No. 6, pp. 773-790, 2002.
[130] Fink, M., "Full-Scale Investigation of the Aerodynamic Characteristics of a Model Employing a Sailwing Concept," *NASA Technical Report*, TR 4062, 1967.
[131] Katz, J., Plotkin, A., *Low-Speed Aerodynamics*, Cambridge University Press, Cambridge, UK, 2001.
[132] Hepperle, M., "Aerodynamics of Spar and Rib Structures," *MH AeroTools Online Database*, http://www.mh-aerotools.de/airfoils/ribs.htm, Mar. 2007.
[133] Ifju, P., Ettinger, S., Jenkins, D., Martinez, L., "Composite Materials for Micro Air Vehicles," *Society for the Advancement of Material and Process Engineering Annual Conference*, Long Beach, CA, May 6-10, 2001.
[134] Allen, M., Maute, K., "Probabilistic Structural Design of UAVs under Aeroelastic Loading," *AIAA "Unmanned Unlimited" Conference*, San Diego, Sep. 15-18, 2003.
[135] Weisshaar, T., Nam, C., Batista-Rodriguez, A., "Aeroelastic Tailoring for Improved UAV Performance," *AIAA Structures, Structural Dynamics, and Materials Conference*, Long Beach, CA, Apr. 20-23, 1998.
[136] Frampton, K., Goldfarb, M., Monopoly, D., Cveticanin, D., "Passive Aeroelastic Tailoring for Optimal Flapping Wings," *Proceedings of Conference on Fixed, Flapping, and Rotary Wing Vehicles at Very Low Reynolds Numbers*, South Bend, IN, June 5-7, 2000.
[137] Snyder, R., Beran, P., Parker, G., Blair, M., "A Design Optimization Strategy for Micro Air Vehicles," *AIAA Structures, Structural Dynamics, and Materials Conference*, Honolulu, HI, Apr. 23-26, 2007.
[138] Garrett, R., *The Symmetry of Sailing: The Physics of Sailing for Yachtsmen*, Adlard Coles, Dobbs Ferry, NY, 1996.
[139] Eden, M., *The Magnificent Book of Kites: Explorations in Design, Construction, Enjoyment, and Flight*, Sterling Publishing, New York, NY, 2002.

[140] Templin, R., Chatterjee, S., "Posture, Locomotion, and Paleoecology of Pterosaurs," Geological Society of America Special Paper 376, 2004.
[141] Swartz, S., Groves, M., Kim, H., Walsh, W., "Mechanical Properties of Bat Wing Membrane Skin," *Journal of Zoology*, Vol. 239, pp. 357-378, 1996.
[142] Norberg, U., "Bat Wing Structures Important for Aerodynamics and Rigidity," *Zoomorphology*, Vol. 73, No. 1, pp. 45-61, 1972.
[143] Stanford, B., Abdulrahim, M., Lind, R., Ifju, P., "Investigation of Membrane Actuation for Roll Control of a Micro Air Vehicles," *Journal of Aircraft*, Vol. 44, No. 3, pp. 741-749, 2007.
[144] Maute, K., Allen, M., "Conceptual Design of Aeroelastic Structures by Topology Optimization," *Structural and Multidisciplinary Optimization*, Vol. 27, No. 1, pp. 27-42, 2004.
[145] Stanford, B., "Aeroelastic Analysis and Optimization of Membrane Micro Air Vehicle Wings," Ph.D. Dissertation, Department of Mechanical and Aerospace Engineering, University of Florida, Gainesville, FL, 2008.
[146] Antony, J., *Design of Experiments for Engineers and Scientists*, Butterworth-Heinemann, Boston, MA, 2003.
[147] Gürdal, Z., Haftka, R., Hajela, P., *Design and Optimization of Laminated Composites Materials*, Wiley, New York, NY, 1999.
[148] Sloan, J., Shyy, W., Haftka, R., "Airfoil and Wing Planform Optimization for Micro Air Vehicles," *Symposium of RTO Applied Vehicle Technology Panel*, Ottawa, Canada, Oct. 19-21, 1999.